A Multiwavelength Study of Radio Halos and Relics in Clusters of Galaxies

by

Ruta Kale

A thesis submitted to the

Jawaharlal Nehru University

for the degree of

Doctor of Philosophy

April 2011

Raman Research Institute

Bangalore 560 080

INDIA

Certificate

This is to certify that the thesis entitled 'Multiwavelength Studies of Radio Halos and Relics in Clusters of Galaxies' submitted by Ruta Kale for the award of the degree of Doctor of Philosophy of Jawaharlal Nehru University is her original work. This has not been published or submitted to any other University for any other Degree or Diploma.

Prof. Ravi Subrahmanyan
Director

Prof. K. S. Dwarakanath
Thesis Supervisor

Astronomy and Astrophysics Group,
Raman Research Institute,
Bangalore 560 080
INDIA

Declaration of Authorship

I, RUTA KALE, declare that the work reported in this thesis is entirely original. This thesis is composed independently by me at the Raman Research Institute under the supervision of Prof. K. S. Dwarakanath. I further declare that the subject matter presented in this thesis has not previously formed the basis for the award of any degree, diploma, membership, associateship, fellowship or any other similar title of any university or institution.

Prof. K. S. Dwarakanath **Ruta Kale**

Astronomy and Astrophysics Group,
Raman Research Institute,
Bangalore 560 080
INDIA

Acknowledgements

I take this opportunity to thank all those who have helped me directly or indirectly in the completion of this thesis.

I thank Prof. Dwarakanath for being my thesis advisor and giving me timely suggestions and support. The discussions I had with him were encouraging and inspiring. I am grateful to Prof. Biman Nath, Prof. Dipankar Bhattacharya and Prof. Ravi Subrahmanyan for their interest in my work. I have also benefited from the discussions I had with all the members of Astronomy and Astrophysics Group and many thanks to all of them.

This work would not have been possible without the support I received at NCRA and GMRT. I am grateful to Prof. Ishwara Chandra for giving lessons in data analysis. I thank Prof. Rajaram Nityananda and Prof. Yashwant Gupta for the support I received from them during my visits. I also thank all my friends at NCRA, GMRT and IUCAA who have helped me and provided encouragement from time to time.

The support provided by the administration, the computer section, the library and the canteen at RRI has been excellent and I am thankful to them.

All my friends at RRI have helped me whenever I was in need and made my stay enjoyable. Thank you all !

I thank my family for their encouragement and support throughout the course of this thesis.

We thank the staff of the GMRT that made these observations possible. GMRT is run by the National Centre for Radio Astrophysics of the Tata Institute of Fundamental Research.

The National Radio Astronomy Observatory is a facility of the National Science Foundation operated under cooperative agreement by Associated Universities, Inc.

The Westerbork Synthesis Radio Telescope is operated by the ASTRON (Netherlands Institute for Radio Astronomy) with support from the Netherlands Foundation for Scientific Research (NWO).

This research has made use of the NASA/IPAC Extragalactic Database (NED) which is operated by the Jet Propulsion Laboratory, California Institute of Technology, under contract with the National Aeronautics and Space Administration.

This research has made use of data obtained from the High Energy Astrophysics Science Archive Research Center (HEASARC), provided by NASA's Goddard Space Flight Center.

This thesis makes use of data products from the Two Micron All Sky Survey, which is a joint project of the University of Massachusetts and the Infrared Processing and Analysis Center/California Institute of Technology, funded by the National Aeronautics and Space Administration and the National Science Foundation.

Synopsis

This thesis is about radio halos and relics that represent the non-thermal components (relativistic particles and magnetic fields) of the intra-cluster medium (ICM). We have addressed issues about the origins of these sources through low frequency imaging, spectral index mapping and modelling of radio spectra.

The diffuse cluster-wide (linear extents ∼Mpc) radio sources with no obvious associations with AGNs are evidence for the presence of magnetic fields ($\sim 0.01-1\mu$G) and relativistic electrons in the ICM (eg. Ferrari et al 2008). Such sources when centrally located in clusters following roughly the morphologies of the thermal gas seen in X-rays are called *radio halos* and when are elongated or arclike and at cluster peripheries are termed as *radio relics*. These sources have been detected in ~ 50 clusters so far and are known to occur in $\sim 5\%$ of all clusters and $\sim 30\%-35\%$ of clusters which are brighter than $\sim 5 \times 10^{44}$ erg s^{-1} in X-rays (eg. Ferrari et al 2008). It has been noticed that all the clusters that host radio halos or relics show signatures of undergoing cluster mergers (eg. Feretti 2006). However the exact role of mergers is not clear since many clusters which are merging do not possess radio halos or relics.

The fundamental problems in understanding radio halos and relics are the origins of relativistic electrons and magnetic fields on cluster-wide scales. The radiative lifetime of relativistic electrons being short ($\sim 10^7 - 10^8$ yr) as compared to the time required for them to diffuse to Mpc scale distances ($\sim$ a few Gyr), requires an in-situ mechanism of generating relativistic electrons to form a cluster-wide ($\sim$ Mpc scale) synchrotron source. Shocks and turbulence in clusters are proposed to reaccelerate the electrons in the thermal gas or mildly relativistic electrons ejected by galaxies (eg. Brunetti et al 2003). Reacceleration by turbulence injected in to the ICM during cluster mergers is the most favoured mechanism to explain the radio halos (eg. Brunetti et al 2009). Radio relics have been proposed to be remnants of radio galaxies or revived remnants of radio galaxies by adiabatic compression in shocks or reaccelerated electrons at shock fronts (Slee et al 2001; Ensslin &

Gopal-Krishna 2001; Ensslin et al 1998). These mechanisms have signatures in morphologies and integrated spectra of radio halos and relics. The spectral index distributions over the radio halos and relics have clues about their origin. For example, a flat spectrum edge and steepening away from it indicates acceleration at a shock front, whereas a patchy distribution of spectral index indicates the possible role of turbulence in reacceleration. However due to the difficulties involved in imaging extended, low surface brightness radio halos and relics (angular extents of a few to 10s of arcminutes and surface brightnesses ~ 1 mJy arcmin^{-2} at 1.4 GHz) over a wide range of frequencies, such studies were mainly at 1.4 GHz in the recent past. With the advent of the Giant Metre-wave Radio Telescope (GMRT), opportunities to obtain images at frequencies < 1.4 GHz with resolutions and sensitivities comparable to those at 1.4 GHz have become available. The low frequency capabilities of the GMRT along with those of the WSRT and the VLA are extensively used to uncover properties of radio halos and relics in this thesis.

Low frequencies have the advantage of large primary beams which can image large areas around cluster centres. This is particularly important to detect relics which are far from cluster centres. The steep spectra $\alpha < -1$ ($S \propto \nu^{\alpha}$) of radio halos and relics are of advantage for imaging at low frequencies. A low frequency study of 5 clusters of galaxies that host radio halos and relics and of a sample of ultra-steep spectrum sources was undertaken as a part of this thesis. This thesis demonstrates the successful use of the 150 MHz band of the GMRT for studies of radio halos and relics. Observations at multiple frequencies were used to find spectral signatures of the various acceleration mechanisms. Such studies have been attempted in only a few cases so far (Feretti et al 2004; Pizzo et al 2008).

Role of cluster mergers in the generation of cluster-wide diffuse radio emission is studied in this thesis using two well known clusters of galaxies - A2256 and A754. The cluster A2256 is a rich cluster of galaxies that hosts a radio relic and a radio halo and is suspected to have undergone a major (mass ratio 1 : 2) and a minor (mass ratio 1 : 10) merger in the past Gyr (eg. Clarke & Ensslin 2006; Sun et al 2002; Berrington et al 2002). Using a combination of telescopes such as the GMRT at 150 MHz, the WSRT at 350 MHz and the VLA at 1369 MHz,

spectral index maps of the radio halo and the relic with resolutions $\sim 1'$(FWHM) were constructed. This study reveals that turbulent reacceleration may be the mechanism that generated the radio halo and the relic. The properties of the radio relic are consistent with a shock possibly due to a recent minor merger. The diffuse radio emission in A2256 shows an intriguing property of steepening at lower frequencies. We interpret this as a result of two epochs of reacceleration which are consistent with the two mergers. The case of A2256 is also used to show the futility in correlating average spectral indices and average temperatures in respective clusters.

The cluster A754, also rich and merging, is a host to diffuse radio emission, but has no well defined radio halo. At 150 MHz, using the GMRT, we discovered a new steep spectrum ($\alpha < -1.5$) feature in A754. Another diffuse radio blob located along the proposed axis of merger but ~ 0.7 Mpc from the cluster centre is likely to be a radio relic in A754. We test the possibility of this radio relic being a shock compressed cocoon of a radio galaxy. For this purpose a code for the theoretical framework of Ensslin and Gopal-Krishna (2001) was developed and applied. It turns out that the relic in A754 is consistent with an ageing cocoon of radio galaxy; no shock compression is required. This relic and the other blobs of the diffuse radio emission in A754 are lurking cocoons of radio galaxies or results of turbulent reacceleration.

Radio relics are a class of diffuse radio sources which show a wide variety in their morphologies, spectra and environments. A multi-frequency analysis of three radio relics with modelling of their radio spectra using the adiabatic compression model is presented in this thesis. The radio relics in the clusters A4038, A1664 and A786 were selected for such an analysis. The locations of the relics in A4038, A1664 and A786 are at the cluster centre, at the cluster periphery and at the cluster outskirts, respectively. The low frequency (150, 235 and 606 MHz) images of the relic in A4038 reveal a whole new story. A new steep spectrum component that forms an extention of the earlier known relic is discovered. Also a plume having low surface brightness and steep spectrum is suspected toward the northwest of the main source. These discoveries have revealed more than twice the extent of

the radio relic that was known from earlier studies at 1.4 GHz. Considering that the size of the relic is an important input to make estimates of its magnetic field, it is crucial to make sensitive multifrequency images to map its entire extent. The model fit to the integrated spectrum of the relic in A4038 is consistent with an adiabatically compressed cocoon. The projected location of the relic is nearly at the cluster centre and close to the cD galaxy. Such diffuse steep spectrum plasma in cluster can also be the non-thermal bubbles created by radio galaxies. Cavities in the X-ray images are expected in that case. However no cavities have been reported in the cluster A4038 so far. We emphasize the effects of projection which may be important in such cases. The relics in A1664 and A786 represent relics in extremely low density environments. We suggest that possibly due to low external pressure the sizes of these relics are larger than that of the A4038 relic. The spectra of these relics are consistent with those of lurking fossil radio galaxies. The relic near A786 may be a relic at the large scale structure formation shock as suggested by Ensslin et al (1998).

Steep spectra ($\alpha < -1$) are characteristic of radio halos and relics. Samples of sources identified from surveys using the criteria of steep spectra and extended nature can result in discoveries of radio halos and relics. This possibility was explored by identifying marginally resolved sources with ultra-steep spectra ($\alpha < -1.8$) from the NVSS (1400 MHz survey) and the VLSS (74 MHz survey). The morphologies of the sources in this sample turned out to be double lobed with no obvious radio core or jets. Thus a sample of relic radio galaxies has been serendipitously discovered. The injection (or activity) timescales for the progenitor AGN and the relic timescales were estimated using a model that accounted for the evolution of radio galaxy taking into account the synchrotron, the inverse-Compton and the adiabatic expansion losses. The model estimates also show that these sources are the relics of radio galaxies which were 10-100 times brighter than the brightest known radio galaxy in the local universe. Discoveries of such sources are valuable to learn about the life cycles of radio galaxies.

The next generation radio telescopes such as the LOFAR, the LWA and the SKA will provide observing capabilities at < 100 MHz, at sensitivities and resolutions

better than the best possible today at 1.4 GHz. The major contribution of the low frequency surveys carried out is expected to be in providing a statistically complete sample of radio halos and relics. Discoveries of new ultra-steep spectrum components in the known radio halo and relic sources and of an entire new sample of radio halos and relics are awaited from the new generation of telescopes. In this context, this thesis is a timely demonstration of what is to be expected from the facilities in future.

Prof. K. S. Dwarakanath
Thesis Supervisor

Ruta Kale

Contents

List of Figures

List of Tables

Dedicated to my (late)grandmother

Chapter 1

Introduction

1.1 Clusters of Galaxies

Clusters of galaxies are the most massive gravitationally bound systems in the Universe. These are the nodes in the large scale filamentary structure of the Universe formed by hierarchical growth. Numerical simulations have shown that primordial density perturbations lead to formation of the first structures in the Universe which grow further, driven by gravity. A slice of the Millennium Simulation (Springel et al 2005) is shown in Fig. 1.1 (left). It is a visual impression of the distribution of the dark matter on large scales in the Universe at the present epoch. A cluster of galaxies formed at the intersection of the filaments is shown in Fig. 1.1 (right). The clusters are fed by the filaments and continue to grow at the present epoch. Surveys such as the 2dF galaxy redshift surveys have provided a view of large scale structure in the Universe (Peacock et al 2001).

Clusters of galaxies were identified as regions of overdensities in the projected distribution of optically detected galaxies (eg. Zwicky 1938; Abell 1958). The clusters contain hundreds to thousands of galaxies in regions of linear sizes $\sim$ Mpc (eg. see Fig. 1.2, right). The galaxies move with typical velocity dispersion along the line sight of $\sigma_v \sim 10^3$ km s^{-1}. As seen in the X-ray band, galaxy clusters appear to be aggregates of hot plasma (eg. see Fig. 1.2, left). The X-ray emission

from clusters is dominated by the hot ($10^7 - 10^8$ K) plasma which pervades the space between the galaxies and emits by thermal bremsstrahlung mechanism. This plasma is part of the diffuse matter in clusters, called the intra-cluster medium (ICM). Clusters of galaxies typically have masses $\sim 10^{14} - 10^{15}$ $M_\odot$. Most of the mass is however not luminous, but is in the form of dark matter ($\sim 80\%$), known only through its gravitational interactions. About 15% of the total mass is in ICM and $\sim 5\%$ is in galaxies.

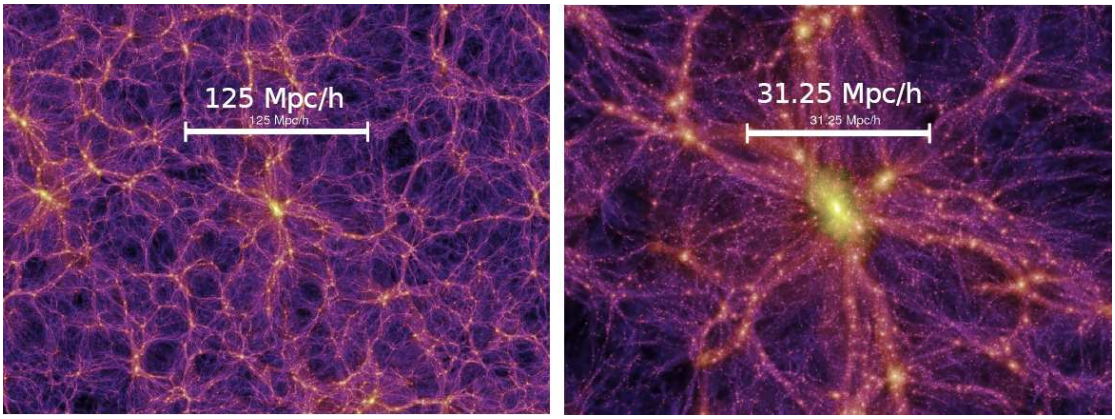

FIGURE 1.1: *(Left)*Visual impression of the dark matter structure on large scales at the present time as shown by the Millennium simulation. *(Right)* A closer view of a galaxy cluster formed at the intersection of filaments. (Images: VIRGO consortium)

1.1.1 The Intra-Cluster Medium

The ICM is composed of thermal plasma with electron densities $n_e \sim 10^{-3} - 10^{-4}$ cm^{-3}, relativistic particles and magnetic fields. The thermal plasma is detected due to the X-ray emission, reaching luminosities, $L_x \sim 10^{45}$ erg s^{-1} (eg. Ferrari et al 2008). Spectral lines from the ICM reveal that it has a metallicity of about a third of that of the sun (eg. Loewenstein 2003). The relativistic particles and magnetic fields are not easily detected. The presence of relativistic electrons and magnetic fields ($\sim 0.1 - 1\mu$G) is revealed by sources of synchrotron emission associated with the ICM (Ferrari et al 2008). These sources are termed as radio halos and relics (discussed in Sec. 1.3 and 1.4). Other method that led to infer the presence of magnetic fields in the ICM is by studying the Faraday rotation of the

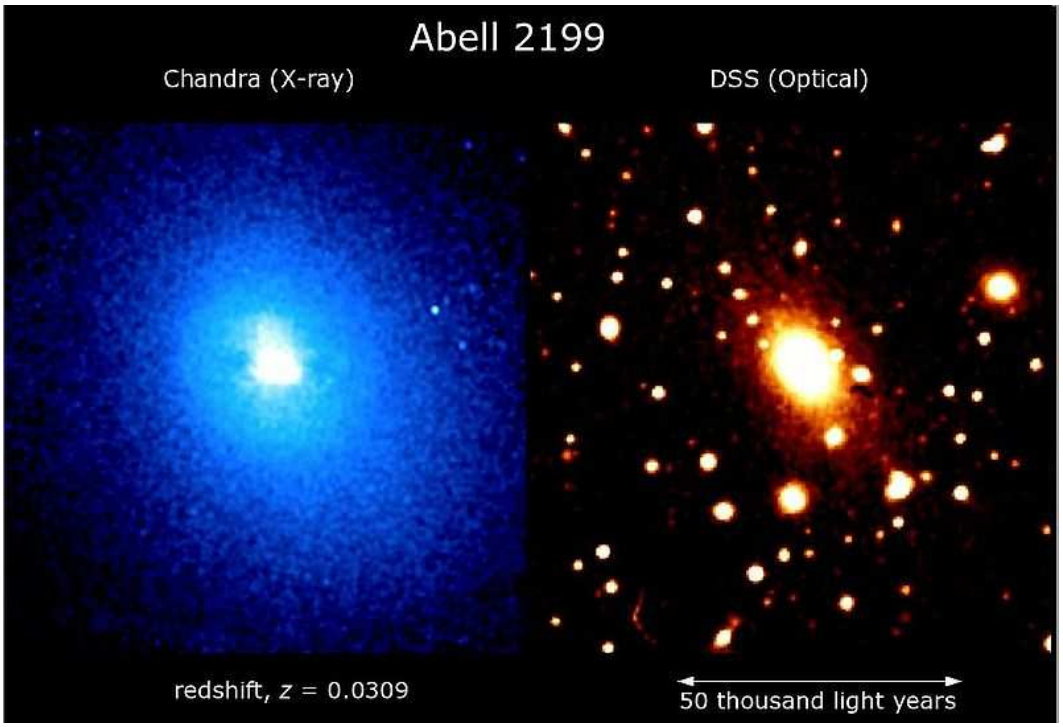

FIGURE 1.2: View of a galaxy cluster in X-rays and in optical. (Image: HEASARC)

plane of polarization of background sources (eg. Kim et al 1991). The minimum energy density contained in the non-thermal components of the ICM (relativistic particles and magnetic fields) is $\sim 10^{-14} - 10^{-13}$ erg cm^{-3} which is about 1000 times lower than the energy density of the thermal X-ray gas in the ICM (Feretti 2006).

Observations of clusters in the hard X-ray (HXR) bands ($\geqslant$ 10 keV) using the Beppo-SAX and the RXTE have also hinted at the presence of relativistic electrons in the ICM (eg. Coma, Fusco-Femiano et al 2004; Rephaeli & Gruber 2002; A2256, Fusco-Femiano et al 2005; Rephaeli & Gruber 2003). The HXR emission is detected as an excess over the emission expected by extrapolation of the soft X-ray (0.1-2 keV) spectrum due to thermal Bremsstrahlung from the ICM. The inverse-Compton scattering of the CMB photons by the relativistic electrons in the ICM is the main physical process which leads to an excess in HXR band (Rephaeli et al 2008). The detections of clusters in HXR bands being only at the levels of 3σ and the physical processes that lead to it are still debated (Rossetti & Molendi 2004; Fusco-Femiano et al 2007).

Mergers of clusters deeply affect the physical properties of the components of the clusters (Ferrari et al 2008). Apart from the signatures in the spatial distribution of optically detected galaxies (eg. Girardi & Biviano 2002), the ICM can be a very good tracer of the dynamical activities in the cluster. The substructure and discontinuities in the distribution of the X-ray emission from the ICM (Markevitch et al 2000; Buote 2002 and references therein), patchy distribution of temperature, pressure, entropy and metallicity maps of clusters (eg. Finoguenov et al 2005; Kapferer et al 2006) are all indicators of mergers.

1.2 Radio Emission from clusters of galaxies

Star formation, supernovae, activity at the nuclei of galaxies, jets and associated lobes of radio galaxies are sources of radio emission which are present in clusters of galaxies. Diffuse radio sources of size $\sim 200 - 400$ kpc around the giant elliptical galaxies at centres of clusters are referred to as radio mini-halos (eg. 3C 84 in the Perseus cluster, Burns et al 1992; for a review see Ferrari et al 2008). These are all associated with individual galaxies in the cluster. In some clusters, diffuse, extended radio emission that cannot be associated with radio galaxies or any individual galaxies is detected. Such radio sources are referred to as radio halos (Sec. 1.3) and relics (Sec. 1.4).

This thesis deals with radio halos and relics. Here the basic radiation physics required to understand the spectra of these sources is introduced. The radio spectrum is described by a power-law, $S \propto \nu^{-\alpha}$, where α is the spectral index. Theories which deal with the emission of cosmic rays (relativistic particles) that give rise to the radio emission, state that the spectral index α is ~ 0.7 at injection (eg. Blandford & Eichler 1987).

1.2.1 Mechanisms of energy losses

After generation, the spectrum changes due to various energy losses and gains. When relativistic electrons move in spiral trajectories around magnetic field lines, synchrotron radiation is emitted (classical counterpart being the cyclotron emission). Consider a population of relativistic electrons with an energy distribution of

$$N(E)dE = KE^{-p}dE, \tag{1.1}$$

where p is the electron energy index. Synchrotron radiation from such a population leads to a power law spectrum. The index p is related to the spectral index α by the relation, $\alpha = (p-1)/2$ (eg. Longair 1981). At injection the spectral index $\alpha = 0.7$. This spectrum is modified with time by losses due to synchrotron radiation, inverse Compton (IC) radiation (relativistic electrons scattering off the cosmic microwave background (CMB) photons) and adiabatic expansion. In the ultra-relativistic limit ($v \rightarrow c$), and assuming isotropic pitch angle distribution, the average rate of energy loss by synchrotron radiation is given by,

$$-\frac{dE}{dt}_{synch} = \frac{4}{3}\sigma_T c\gamma^2 U_{mag} = 6.6 \times 10^4 \gamma^2 B^2 eVs^{-1}, \tag{1.2}$$

where, σ_T is the Thomson scattering cross section, $\gamma = E/m_e c^2$ is the Lorentz factor and B is the magnetic field in units of Tesla ($= 10^4$ Gauss) (Longair 1981). Notice that the energy loss is proportional to the square of the energy of the electron and B. Thus higher energy electrons lose energy faster.

The CMB photons are omnipresent and electrons lose energy by IC scattering. The energy losses are similar to synchrotron losses, except that the magnetic energy density is replaced by the CMB energy density, U_{rad} in Eq. 1.2. The energy density of the CMB photons depends on the redshift and can be expressed as an equivalent magnetic field producing the loss. This equivalent IC field, B_{IC}, is given by,

$$B_{IC} = 3.25(1+z)^2, \tag{1.3}$$

where B_{IC} is in units of microgauss (μG) (eg. Feretti & Giovannini 2007). If the particle injection is not continuous and is left to evolve after a one time injection of a power-law distribution, the spectrum develops a break. The break frequency, ν_{br} (in units of Hz) is given by,

$$\nu_{br} \approx 3.4 \times 10^8 B^{-3} t^{-2}, \tag{1.4}$$

where t is the time elapsed since the injection in yr and B is the magnetic field in units of gauss (Moffet 1975).

The relativistic gas due to expansion in the surrounding medium will lose internal energy (PdV work done on the surrounding medium). The energy loss and change in the volume resulting in a change in the magnetic field affect the spectrum. On the other hand, if the relativistic gas is compressed, the magnetic energy density increases and leads to enhanced synchrotron emission. The theoretical framework for consideration of synchrotron, IC and adiabatic expansion (or compression) has been provided by Ensslin & Gopal-Krishna (2001) and will be discussed in Sec. 1.4.2 and in chapter 3.

1.3 Radio Halos

Radio halos have a regular morphology, are unpolarized ($\lesssim 5\%$) (exceptions of A2255, Govoni et al 2005 and MACS J0717.5+3745, Bonafede et al 2009a), and are centrally located in galaxy clusters like the hot gas emitting X-rays (eg. Ferrari et al 2008). The sizes of radio halos range between few hundreds of kpc to 2 Mpc. Those with sizes $\sim$ Mpc or more are often referred to as giant radio halos. The first radio halo to be discovered was in the rich nearby (z=0.02) cluster 'Coma' (Willson 1970; Schlickeiser et al 1987; Kim 1990; Giovannini et al 1993; Deiss et al 1997; Thierbach et al 2003). This is a prototype of the class of giant radio halos having a size $\sim$ Mpc (Fig. 1.3, left). The spectrum of Coma radio halo (Coma C) is shown in the right panel of Fig. 1.3. The spectrum is straight over 100 to 1000 MHz and shows steepening at higher frequencies. Two other examples of radio

halos are shown in the two panels of Fig. 1.4. The left panel shows the radio halo in the cluster A2163 (Feretti et al 2001). It is circular in shape, bright at the centre and weakens towards the peripheries. Some compact radio sources are also present in the image. The right panel shows the radio halo in contours overlaid on the spectacular X-ray emission in the 'Bullet' cluster (Liang et al 2000; Markevitch et al 2002). The radio emission is elongated in the direction of elongation of the X-ray emission but does not show any special features at the location of the bow shock seen at the right side in the X-ray image. Radio halos contain energies $\sim 10^{61}$ erg. The magnetic field derived using the standard condition of equipartition are $\sim 0.1 - 1\mu$G (eg. Ferrari et al 2008). Radio halos in about 30 galaxy clusters with redshifts less than 0.4 are known (Giovannini et al 2009).

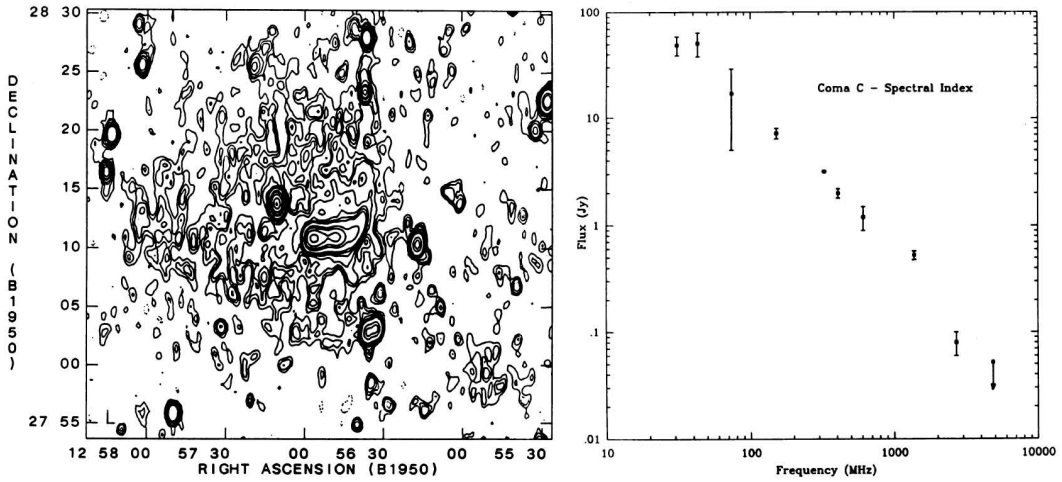

FIGURE 1.3: *Left* Image of Coma C at 608.5 MHz using the WSRT. The synthesized beam is $63'' \times 35''$ (P. A. 0°) and contours are at -1, 1, 1.5, 2, 3, 5, 7, 10, 30, 50, 100, 200, 300 mJy beam^{-1}.*Right* Spectrum of Coma C. Both the panels reproduced from Giovannini et al (1993).

The main issue regarding the explanation of radio halos is their large extent and the short radiative lifetimes of the relativistic electrons. The diffusion velocities of electrons are of the order of $\sim$ 100 km s^{-1} (Alfven speed, $v_A = B/\sqrt{4\pi\rho}$, where, ρ is the mass density; Petrosian & Bykov 2008). The time taken to diffuse to distances of the order of Mpc is 10-100 times longer than the typical radiative lifetime ($\sim 10^7 - 10^8$yr) of the relativistic electrons. Thus electrons accelerated at a single source could not have diffused out to Mpc distances to produce the observed radio halo emission. This problem was first identified by Jaffe (1977). This was

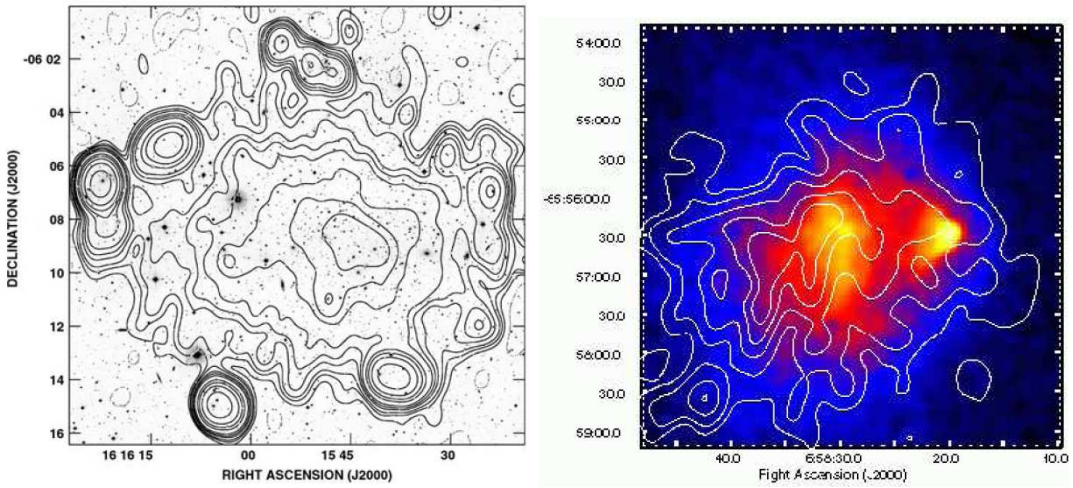

FIGURE 1.4: *Left* Radio contours of A2163 at 1400 MHz (VLA) overlaid on DSS optical R band image. Synthesized beam is $45'' \times 60''$ (P. A. 0°). Contour levels are ar -0.1, 0.1, 0.2, 0.3, 0.5, 0.7, 1, 2, 3, 5, 10, 25 mJy beam^{-1}(Feretti et al 2001). *Right* Radio contours of the radio halo in the 'Bullet' cluster at 1.3 GHz (ATCA) overlaid on Chandra X-ray image (0.5-5 keV) of the cluster shown in colour (Liang et al 2000; Markevitch et al 2002). Contours are at (3,6,12,18,24)×0.09 mJy beam^{-1}and the synthesized beam is $24'' \times 22''$ (P. A. 0°).

resolved by invoking the concept of in-situ reacceleration with an efficiency that is comparable to the energy loss processes. The mechanism that generated the radio halos must lead to energizing of electrons all over the cluster at the same time to create a source that is Mpc in extent and has a lifetime of $\sim 10^7 - 10^8$ yr.

1.3.1 Origin of relativistic electrons

A fundamental question for any mechanism to explain radio halos is about the origin of the relativistic electrons in the ICM. Models considered to explain the radio halos fall into two main categories, depending on the consideration for the origin of relativistic electrons: the primary models and the secondary models.

The primary models consider that the relativistic electrons in the ICM originated from the galaxies (star formation, supernovae, galactic winds and AGN) or from the thermal pool of electrons in the ICM. Merger shocks may be able to inject particles with $\gamma > 10^3$ (Sarazin 1999). In-situ acceleration by turbulence can also

continuously energise particles (Schlickeiser et al 1987). Another possibility is reacceleration of mildly relativistic electrons in the ICM by merger driven turbulence - turbulent reacceleration (eg. Brunetti et al 2001).

The secondary models attribute the origin of the relativistic electrons to the hadronic collisions in the ICM. The ineleastic collisions between hadrons produce relativistic electrons as secondary products which radiate the observed synchrotron emission in the presence of the cluster magnetic field (Dennison 1980; Blasi & Colafrancesco 1999; Dolag & Ensslin 2000). During the evolution of the cluster, all the particles may undergo acceleration. The relativistic electrons lose energy fast, but the protons can retain their energy for a much longer period. This leads to accumulation of a pool of relativistic hadrons in the ICM and collisions of these lead to continuous generation of relativistic electrons. This avoids the problem of diffusion of the electrons within their short radiative lifetimes. However, these models have two major problems: first, the gamma rays that are expected from the same hadronic interactions have not been detected by EGRET (Reimer et al 2003) and FERMI (Jeltema & Profumo 2010). Secondly, the hadrons would have accumulated in all clusters and led to radio halo emission from all clusters. From observations, it has been found that radio halos occur in only about 5% of all clusters (Feretti 2006; Sec. 1.3.3). These are serious drawbacks of the idea of the relativistic electrons being secondary products of haronic collisions.

1.3.2 Turbulent reacceleration model

Turbulent reacceleration is a mechanism by which Mpc scale radio emission can be generated in clusters of galaxies (eg. Harris et al 1980; Tribble 1993; Brunetti et al 2001; Fujita et al 2003; Brunetti et al 2004; Brunetti & Lazarian 2007). Currently, this is the most favoured scenario for explaining the radio halos. Here a very simple overview of this much complicated process is presented. The first step for this mechanism is injection of fluid turbulence in the ICM. Mergers of clusters are one of the most favoured routes for injection of fluid turbulence on scales of 0.5-1 Mpc in the ICM. Numerical simulations and observations have provided evidence for

the existence of fluid turbulence in the ICM on the scales of 0.1 - 1 Mpc (Sunyaev et al 2003; Schuecker et al 2004; Churazov et al 2004; Gastaldello & Molendi 2004; Dolag et al 2005; Vazza et al 2006). According to the simulations of cluster mergers by Cassano & Brunetti (2005), mergers with mass ratios in the range 3-10, as is the case of A2256, inject energy equivalent to $5-8\%$ of that of thermal gas in large-scale fluid turbulence. The next step in acceleration by turbulence is the conversion of fluid turbulence to MHD turbulence. This is believed to occur by the *Lighthill* mechanism (Brunetti et al 2004) in the ICM. Different modes of MHD turbulence such as Alfven waves, slow and fast magnetosonic(MS) waves can be activated and each of these have different channels of wave-wave and wave-particle interaction. Efficient cascade process due to wave-wave interactions must then produce the MHD scale relevant for wave-particle interaction. At this step the particle acceleration occurs. The MHD waves eventually get damped due to wave-particle interactions and thus the reacceleration is quenched.

Each of the modes of MHD turbulence have been considered for efficiency of particle acceleration in the ICM. The scale for particle acceleration via Alfven waves has been found to be ~ 1 pc and thus reacceleration is efficient only after significant cascade process (Feretti & Giovannini 2007). Moreover since Alfven waves are damped by protons, this requires that less than $5\% - 10\%$ of the cluster thermal energy be in protons, else the reacceleration will be suppressed (Brunetti et al 2004). For the fast magnetosonic (MS) waves the wave-particle interaction scale is $\sim$ kpc and thus the cascading required is not as much as for the Alfven waves (Feretti & Giovannini 2007). The MS waves are damped due to thermal electrons and thus the reacceleration is not affected by the energy content of the protons in the ICM (Cassano & Brunetti 2005).

The efficiency of turbulent reacceleration depends on many factors such as the timescale for cascading and wave-particle coupling which depend on many physical quantities which are unknown. For example, the spectrum of the MS waves and the structure of the magnetic fields are not known. However, Cassano & Brunetti (2005) have shown that MS waves with scales ~ 100 kpc can efficiently accelerate

fast electrons in the ICM to energies sufficient for producing the synchrotron emission detected in radio bands. The decay time of the MHD turbulence at injection length scales ($L_{inj} \sim$ 1Mpc) can be estimated using:

$$\tau_{kk}(Gyr) \sim (\frac{v_i}{2 \times 10^3 kms^{-1}})^{-1}(\frac{L_{inj}}{1Mpc})(\frac{\eta_t}{0.25})^{-1} \quad (1.5)$$

where v_i is the relative velocity of impact of merging clusters and η_t is the fraction of the energy in turbulence that is in MS waves (Cassano & Brunetti 2005). The value of η_t has been constrained by requiring that the accelerated electrons can produce synchrotron emission with spectral index $\sim 1.1 - 1.5$ between 327 and 1400 MHz (Cassano & Brunetti 2005).

1.3.3 Cluster mergers and radio halos

All the clusters that host radio halos exhibit properties which indicate the occurrence of a merger event in the last $\sim$ 1 Gyr or so (eg. Feretti 2006). Clusters hosting radio halos show substructure in the optical distribution of galaxies, distortions in X-ray surface brightness distribution and absence of cooling flows (Schuecker et al 2001; Buote 2002; Ferrari et al 2008). They have shown presence of high temperatures ($>$ 10 keV) and of temperature gradients (eg. Markevitch 1998; Markevitch & Vikhlinin 2001). The gravitational binding energy released in cluster-cluster mergers is $\sim 10^{63} - 10^{64}$ erg and thus if only $\sim$ 1% of it is utilised in accelerating particles, sources like the radio halos ($\sim 10^{60} - 10^{61}$ erg) could be produced (Feretti & Giovannini 2007).

The connection between cluster mergers and occurence of radio halos favours the models such as the turbulent reacceleration model. The injection of fluid turbulence on cluster wide scales is possible through mergers. An open question is whether all merging clusters have radio halos. Using projected distributions of galaxies and various tests for detection of substructure, a general consensus is that about 30-60% of clusters have substructure (eg. Girardi & Biviano 2002). However only 5% of all clusters and about 35% of X-ray luminous ($L_x > 10^{45}$ erg

s^{-1}) clusters have radio halos. Buote (2002) propose that radio halos form only in mergers of massive clusters where merger has proceeded fully into the core of the cluster.

The properties of thermal and non-thermal plasma in these clusters are also found correlated. Radio halo power is found to correlate with the cluster X-ray luminosity (Giovannini et al 1999), with total mass (Govoni et al 2001) and with the temperature of the thermal gas (Liang et al 2000). In Fig. 1.5, the $L_x - P_{1.4GHz}$ plot constructed by Giovannini et al (2009) using data from the literature (blue dots) and their new observations (red triangles) for all the known radio halos having redshifts less than 0.4 is presented. It is seen that the clusters most luminous in X-rays have the most powerful radio halos. The various surveys for radio halos have been mainly conducted on X-ray luminous clusters (Giovannini et al 1999; Venturi et al 2008). The relatively less luminous clusters ($L_x < 10^{44}$ erg s^{-1}) have not been surveyed at radio frequencies to indicate whether the correlation holds in this range of X-ray luminosities. Using the WENSS and the WISH surveys (330 MHz surveys with the WSRT, http://www.astron.nl/wow/testcode.php), Delian & Rudnick (2006) have reported discoveries of diffuse radio emission in poor clusters and groups, of power much larger than expected from the $L_x - P_{1.4GHz}$ correlation (also Brown & Rudnick 2009). However it still remains an open question whether the same correlation holds for lower luminosity clusters.

1.4 Radio Relics

Diffuse radio sources with filamentary, elongated morphologies, not associated with any active galactic nucleus are termed as radio relics (eg. Ferrari et al 2008). These can either be associated with galaxy clusters (cluster radio relics) or can be remnants of radio galaxies (relic radio galaxies). Such sources typically have steep synchrotron spectra ($\alpha > 1$) and high degree of polarization ($\sim 10\% - 40\%$) (Ferrari et al 2008 for a recent review). The linear sizes of the relics range from 200 kpc to 2 Mpc. The relic at the periphery of the Coma cluster is a prototype

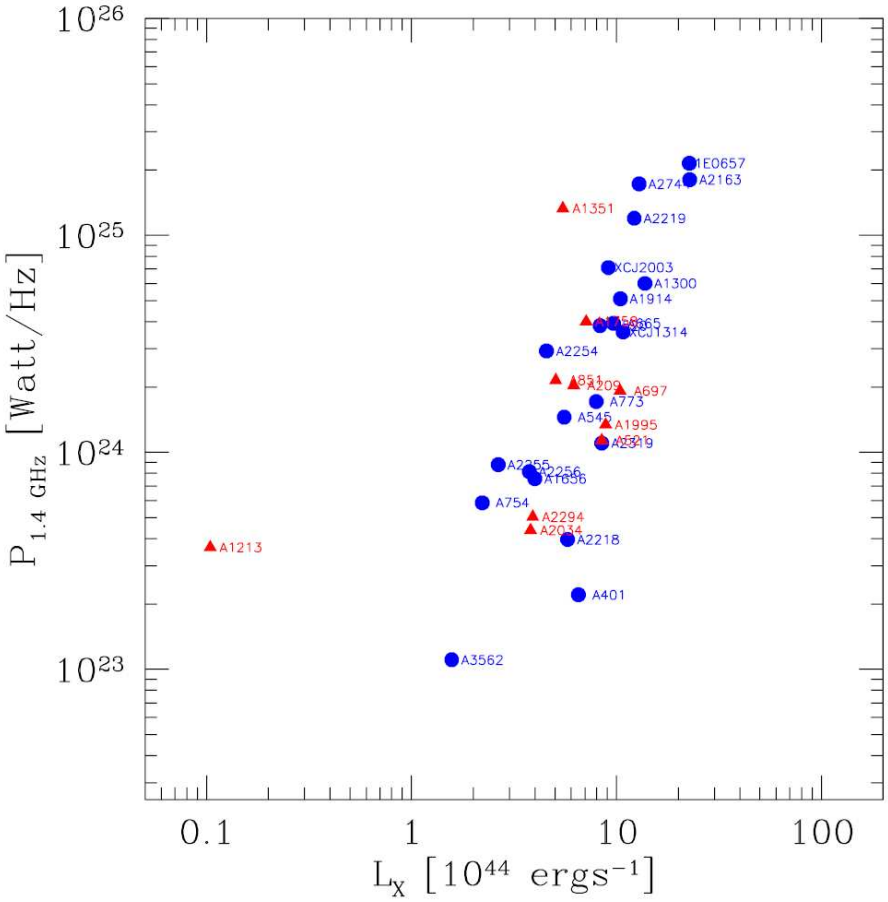

FIGURE 1.5: The $L_x - P_{1.4GHz}$ correlation for radio halos (Giovannini et al 2009). All the known radio halos with redshift < 0.4 are included.

of cluster radio relic (Giovannini et al 1993). The cluster relics show a variety in their morphologies and in their locations relative to centres of clusters. In Fig. 1.6 the relics in A3376 (Bagchi et al 2006) as an example of double arclike Mpc size relics occurring at peripheries of galaxy clusters are shown. In Fig. 1.7, the relics in A85 (left) and A133 (right) (Slee et al 2001) are shown. These are typical of the solitary, filamentary relics at cluster peripheries. Relics are also low surface brightness ($\sim$mJy arcmin^{-2} at 1.4 GHz) sources and occur in only $\sim$ 6% of all clusters (Giovannini et al 1999). The various origins that have been proposed for the radio relics are discussed below.

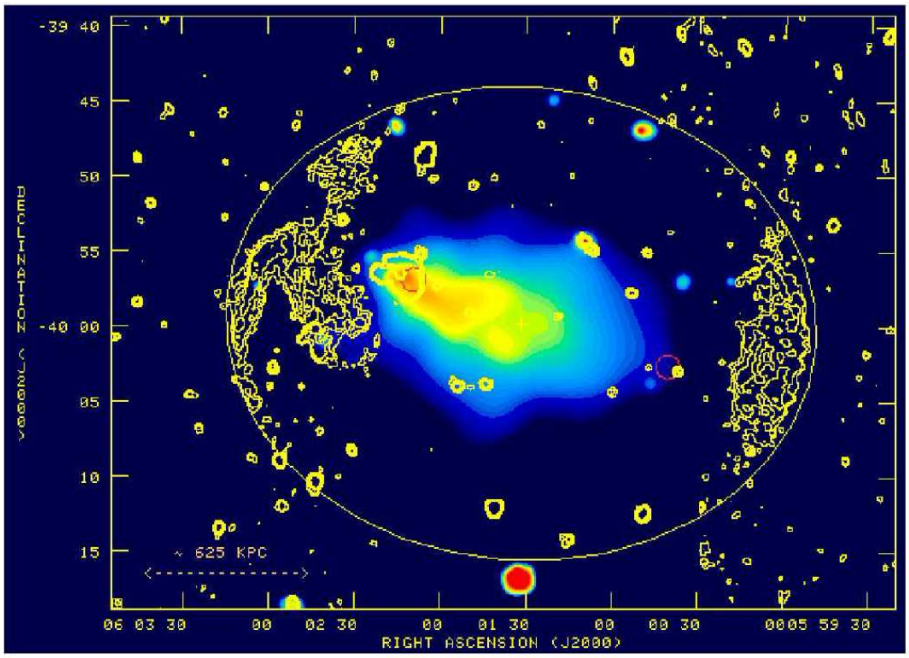

FIGURE 1.6: Image of the cluster A3376 at 1.4 GHz (VLA) shown in yellow contours overlaid on X-ray emission (ROSAT, 0.14 -2 keV) shown in colour. Contour levels are at 0.12, 0.24, 0.48, 1 mJy beam^{-1}and a beam width of 20″(FWHM). An elliptical fit to the relics is overlaid. The " + " marks the center of the ellipse and the red circles mark the positions of two brightest cluster galaxies (Bagchi et al 2006).

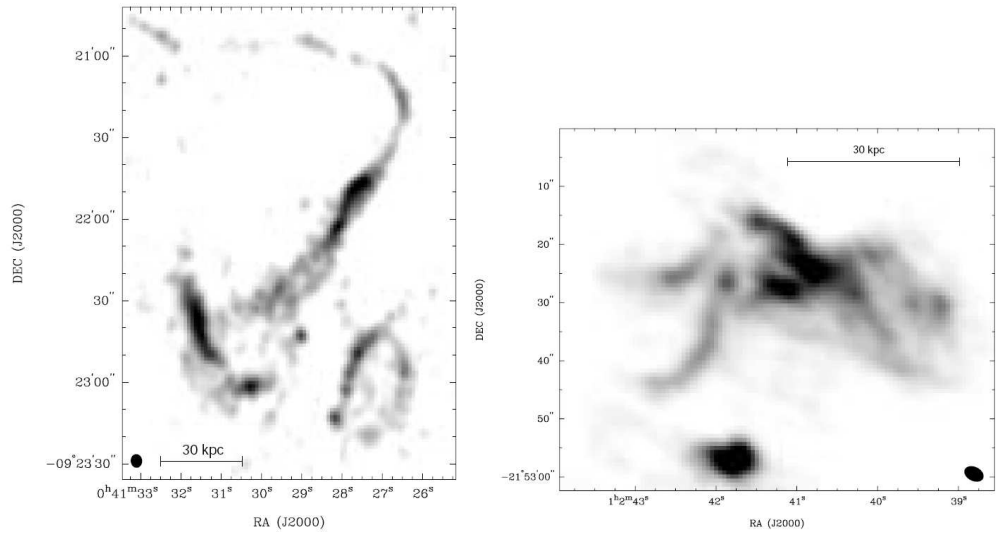

FIGURE 1.7: *Left* A85 at 1.425 GHz. Grey scale varies in the range 0.03 to 0.3 mJy beam^{-1}and the synthesized beam is $5'' \times 4.2''$(P.A. 5°) *Right* A133 at 1.425 GHz. Grey scale varies in the range 0.025 to 3 mJy beam^{-1}and the synthesized beam is $3.5'' \times 2.4''$ (P.A. 64°). Both the panels from Slee et al (2001).

1.4.1 Fossil/relic radio galaxies

Radio galaxies produce jets which pump relativistic plasma into the surrounding medium. Back flows of the relativistic plasma are formed at the end of the jet and the non-thermal plasma occupies regions surrounding the jets forming lobes. The overpressured lobes expand, even after the AGN switches off, until pressure equilibrium is attained and form structures like cocoons. The PdV work done on the surrounding medium during expansion amounts to a loss in energy. Such cocoons can remain detectable after the AGN stops to be active for only about 10-100 million years. These can be then seen as filamentary, elongated or double lobed radio sources with no obvious jets or cores. The short lifetimes can be the reason for a rarity of such sources. For example, the relic in the cluster A85 (Slee et al 2001) could be such a fossil (Fig. 1.7, left). Other examples of such relics are A133 (Fig. 1.6, right) (Slee et al 2001) and the relic in A4038 (Slee et al 2001; chapter 4).

There have been attempts to model the radio spectra of such sources to extract parameters such as the timescale over which the AGN was active, the time spent by the plasma in relic phase and the magnetic field (Komissarov & Gubanov 1994; Slee et al 2001; Kaiser & Cotter 2002). There are two basic approaches to the models.

a. The JP models (Jaffe & Perola 1973): In this approach the pitch angle of the electrons is assumed to isotropize much faster than the energy loss timescale. The scattering of electrons off the Alfen waves causes the isotropization. This produces an exponential cutoff in the spectrum towards high frequencies. The models which use the assumption of isotropization of pitch angles are regarded as JP models.

b. The KP models (Kardashev, 1962; Pacholzcyk, 1970): In this approach the electrons are assumed to preserve their original pitch angle. There is no exponential cutoff in the spectrum. While the continuous injection from the AGN is going on, the spectrum beyond the break frequency has a spectral index of $\alpha + 0.5$ ($S \propto \nu^{-\alpha}$). The models which preserve the pitch angles of electrons are termed as the KP models.

Modifications of the models by Komissarov & Gubanov (1994) were used by Slee et al (2001) to fit the spectra of 4 radio relics. They obtained the activity timescale of the AGN and the time spent by the plasma in relic phase considering synchrotron and inverse-compton losses in the model. However the losses due to adiabatic expansion of the cocoon were not considered. Slee et al (2001) obtained better fits using a model that included a distribution of magnetic fields in the source as opposed to a single field considered earlier.

Although KP models have been found to fit the observed spectra better, the assumption of isotropization of pitch angles is considered more realistic (Slee et al 2001). There are two ways in which the exponential cutoff in a JP spectrum can be avoided. One way is to consider the case where the magnetic fields in the source change from region to region (MJP model, Slee et al 2001). Weaker magnetic field regions result in less steep spectra as compared to those with higher magnetic fields. The resultant spectrum does not have an exponential cutoff. The second way of avoiding the exponential cutoff is to assume that the synchrotron spectra from different regions are of different age and these superpose to give a flatter spectrum. Both these methods assume a case more complex than the one with single magnetic field and a single epoch of generation of the relativistic electron population, but are likely to be closer to the real situations.

1.4.2 Revived cocoons of radio galaxies

Relics have been found in a variety of environments- near cluster centres and also at cluster peripheries. The relic experiences the effects due to disturbances in the surrounding medium. As discussed earlier, the dynamical activities of clusters stir the ICM and drive shocks through it. Ensslin & Gopal-Krishna (2001) (EG01, hereafter) have constructed a theoretical framework for modelling the radio spectrum of a cocoon which is compressed adiabatically by shocks. The compressed magnetic fields lead to enhanced synchrotron emission. Detailed three dimensional magneto-hydrodynamic simulations of the passage of radio cocoon through a shock have been carried out (Ensslin & Bruggen 2002). These show that the cocoon is

initially compressed and then torn into filamentary structures and can also have toroidal shapes. The relic in A85 (Fig. 1.7, left) has been discussed to be such a relic (Ensslin & Bruggen 2002).

1.4.3 Sites of shock acceleration

Radio relics of the kind which are arc-like and located at peripheries of clusters, sometimes forming symmetric double arcs, are believed to be results of acceleration at merger shocks (Ensslin et al 1998; Miniati et al 2001). A spectacular example of such a double relic in the cluster A3376 (Bagchi et al 2006) is shown in Fig. 1.6. The contours represent the radio emission and the X-ray emission is shown in colour. The symmetric relics form portions of an imaginary ellipse (shown in Fig. 1.6). The major axis of this ellipse coincides with the axis of elongation in X-ray surface brightness. Merger shocks along this axis could be responsible for the relics. The slope δ of the power-law distribution of electrons in the ICM is related to the Mach number (M) of the shock by,

$$\delta = 2\frac{M^2+1}{M^2-1} + 1, \tag{1.6}$$

(see Blandford & Eichler 1987 for a review). The spectral index of the resulting radio emission α ($S \propto \nu^{-\alpha}$), is $\alpha = (\delta - 1)/2$. Such radio relics are therefore known to be the tracers of structure formation shocks. Prototypes of these include the relics in A3667 (Rottgering et al 1997) and A3376 (Bagchi et al 2006).

There are relics which are far from cluster centres but occur as single relics. Possibly powered by structure formation shocks are relics such as the one near the cluster A786 called 0917+75 (see chapter 4). This is a single elongated structure, about 5 Mpc from the centre of the cluster and has a linear size of 1.6 Mpc. However since no X-ray emission is detected in the region of this relic, no other independent evidence for shock has been found. Ensslin et al (1998) have considered this relic to be the site of direct shock acceleration.

1.5 Observational Studies

Observational studies of radio halos and relics are important to discover more such sources, to provide constraints on the proposed models by revealing detailed properties and to verify predictions of the models. Radio halos and relics being extended (angular sizes $\sim 3' - 30'$ at 1.4 GHz, z between 0.4-0.02) and steep spectrum ($\alpha > 1$) sources, are ideal targets for low frequency (< 1.4GHz) observations. Along with a good uv-coverage at short baselines to image extended sources, good resolution is required to distinguish the diffuse emission from discrete sources. A single telescope facility fulfilling all these requirements at multiple frequencies is not available and thus a combination of different telescopes is required. Such studies have been difficult and thus rare (eg. Harris et al 1993; Giovannini et al 1993). In the last 10 years, the GMRT has provided the low frequency bands with good uv-coverage for the studies of radio halos and relics. The importance of recent low frequency studies and the need for more is highlighted.

Although spectra of radio halos and relics are crucial to learn about the acceleration processes active in the ICM, only a few multi-frequency studies have been possible. Of all the radio halos ($\sim$ 30), only 4 have radio spectra sampled at more than 3 frequencies over the range of $\sim$0.1 - 1.4 GHz (Giovannini et al 2009). Among those that have been observed at atleast 3 frequencies, spectral steepening has been reported in 5 radio halos so far (Coma C, Thierbach et al 2003; A754, Bacchi et al 2003; A2319, Feretti et al 1997; A3562, Venturi et al 2003, Giacintucci et al 2005; A521, Brunetti et al 2008). Thus the spectra of radio halos are not known well enough to conclude about the shape in general.

The radio spectra of radio relics have also not been sampled enough. Only a few studies exist. The relic in the Coma cluster has been observed at several frequencies (tens of MHz to few GHz) and the spectrum is a power law with a spectral index of 1.2 (Thierbach et al 2003). Relics such as A4038, A133, A85 and A13 (Slee et al 2001; Young et al 2004) have been observed at multiple frequencies (upto 1.4 GHz) and are known to have spectra well fitted by a single power law. Even among these, imaging at low frequencies with sensitivities and resolutions

comparable to that at 1.4 GHz has not been carried out. Thus the estimates of the flux densities of the relics rely on the subtraction of the contributions of discrete sources from the total flux densities measured using a single dish or poor resolution observations.

Recent attempts of low frequency observations have resulted in detections of new features in the previously known radio halo and relic sources. A steep spectrum radio halo was detected at 235 MHz in the cluster A521 where only a relic was known from earlier 1.4 GHz observations (Giacintucci et al 2008; Brunetti et al 2008). This new steep spectrum radio halo has been shown to be consistent with the expectations of the turbulent acceleration model (Brunetti et al 2008). New radio relics at distances $\sim$ 2.2 Mpc from the cluster centre were detected in the cluster A2255 at 150 MHz, thanks to the wide primary beam of the WSRT (Pizzo et al 2008). Recently, van Weeren et al (2010) have also reported detection of a relic far from the centre of the cluster A2256 at 330 MHz. Sensitive low frequency observations are thus leading to discoveries owing to the wider primary beams.

Studies of spectral index distribution over radio halos and relics, although crucial to provide clues on models, are very rare. These are due to the difficulties in obtaining comparable quality images at different frequencies. Spectral index maps of only a few radio halos (A665 and A2163, Feretti et al 2004; A2744 and A2219, Orru et al 2007; A3562, Giacintucci et al 2005; A2255, Pizzo & de Bruyn 2009; A2256, Chapter 2) have been constructed so far. Variations of spectral index on small scales ($<$ 100 kpc) which possibly reflect the complex process of reacceleration by turbulence have been found. Trends of spectral steepening from centre towards periphery in clusters A665 and A2163 have been used to infer the distribution of magnetic field in the clusters by assuming a reacceleration process of fixed efficiency (Feretti et al 2004). A patchy distribution of spectral indices having no correlation with X-ray brightness features has been found in the radio halo in A2744 (Orru et al 2007). The complex distributions favour the turbulent reacceleration scenario (Ferrari et al 2008). However, the complex features in only a few spectral index maps are not enough to conclusively rule out the possibility of the role of shocks in the generation of radio halos.

Spectral index studies of relics are even rarer. Spectral index distributions over the relics in A3667 (Rottgering et al 1997), Coma relic (Giovannini et al 1991), A2256 (Clarke & Ensslin 2006; Chapter 2), A2744 (Orru et al 2007), A521 (Giacintucci et al 2008) and A1242 and A2345 (Bonafede et al 2009b) have been reported. The spectral index steepening from inner to outer edges of the double relics in A1242 and A2345 have been interpreted to be consistent with the model of outgoing merger shocks (Bonafede et al 2009b). Giacintucci et al (2008) have also reported a mild trend of similar spectral steepening and shown it to be consistent with the shock acceleration scenario (Sec. 1.4.3). However, the evidence is scant due to large errors on the spectral index maps.

Radio halos and relics are rare sources and require radio observations with good sensitivity (surface brightness sensitivity $\sim$mJy arcmin^{-2} at 1.4 GHz) for detection. This makes the surveys for such sources difficult. Giovannini et al (1999) used the NVSS to search for radio halos and relics in Abell clusters brighter than X-ray flux, $f_X > 5 \times 10^{-12}$ erg cm^{-2}s^{-1} in the 0.1-2.4 keV range. This search led to the discovery of 18 possible radio halos and relics which have been studied further at 1.4 GHz (Govoni et al 2001; Bacchi et al 2003). A survey of X-ray luminous ($L_x > 5 \times 10^{44}$ erg s^{-1}) clusters in the redshift range of 0.2 to 0.4 was carried out using the GMRT at 610 MHz which resulted in the discovery of 10 radio halos and 3 radio relics (Venturi et al 2008).

1.6 This Thesis

1.6.1 Motivation

The primary motivation for this thesis is to explore the currently available lowest possible frequencies to study the radio halos and relics. As highlighted in the previous section, low frequency studies of radio halos and relics are rare but crucial to make progress in understanding them. Low frequencies also provide opportunities to discover diffuse sources which were either too far from the cluster centre (for

high frequency primary beams to image) or have steep spectra (for high frequency sensitivities to detect).

The GMRT (Appendix A) started regular observations in 2001 and provided observing facilities at 150, 235, 330, 610 and 1400 MHz bands. The hybrid configuration of the GMRT which provides good uv-coverage at short and long baselines is ideal for imaging of the radio halos and relics. Most of the early observations from GMRT were carried out in the relatively trouble-free 1400 MHz band. Some observations of radio halos and relics were also attempted at lower frequencies ∼235 MHz using the GMRT (eg. Giacintucci et al 2005; 2008). The lowest frequency band of 150 MHz was unexplored due to concerns regarding RFI and problems related to ionosphere. In this thesis we present the first studies of diffuse radio halo and relic sources at 150 MHz using the GMRT. A resolution of 20″ (FWHM) and a sensitivity to extended emission with angular size $\sim 68'$ are the highlights of the capabilities of the 150 MHz band at GMRT. Surface brightness sensitivities of $\sim$ 15 mJy beam^{-1}can be achieved (rms $\sim 1-6$ mJy beam^{-1}, dynamic range of 1000-1500) and are sufficient to image the bright (surface brightness ~ 1 mJy beam^{-1}, beam FWHM $\sim 45''$ at 1.4 GHz) radio halos and relics. The large primary beam at low frequencies (a FWHM of 4° at 150 MHz with the GMRT) allow imaging of regions around cluster centres out to distances of $\sim$ 4 Mpc or more even in nearby (z$<$ 0.1) clusters. This is of particular advantage to search for diffuse relics which can be located along the filaments in the large scale accretion shocks, far from the cluster centres (eg. 5 Mpc, in the case of 0917+75, Harris et al 1993).

In this thesis we utilise all the available frequency bands at the GMRT, including the lowest of those (150 MHz) to image radio halos and relics and present the most sensitive images of a select sample of these sources over the frequency range of 150 - 1400 MHz. Apart from the GMRT, the WSRT and the VLA are also used in this thesis to carry out multi-frequency study of radio halos and relics. A brief overview of these telescopes is provided in Appendix A.

The next step to obtaining images and well sampled radio spectra of the radio halos and the relics is to compare them with the expectations of proposed models. So far only a few attempts to reproduce the spectra of radio halos using models have been carried out (Coma C, Schlickeiser et al 1987; A521, Brunetti et al 2008). The complexity of the physical processes involved in models such as the turbulent reacceleration make the comparison with observed integrated spectra difficult. Geometries of merger inferred from spectral index maps and from X-ray surface brightness and temperature maps can be compared. Timescales for core passage of subcluster and the spectral age of the relativistic plasma will be similar if the acceleration of the particles has indeed occurred during the merger. Studies using maps at multiple frequencies and spectral index maps between more than one pair of frequencies is presented in this thesis.

The radio relics have been modelled as radio galaxies and sites of direct shock acceleration (Sec. 1.4). The adiabatic compression model (EG01) proposed to explain the radio relics has not been tested extensively. The theoretical framework provided by EG01 was coded and has been used to model the relic spectra in this thesis. The losses and gains due to adiabatic expansion and compression of the relativistic plasma are taken into account. The timescale for which the AGN was active and the time which the cocoon spent after the AGN switched off can be estimated.

1.6.2 Organisation of this thesis

A brief overview of the work presented in subsequent chapters of this thesis is given below.

Chapter 2: In chapter 2, a multi-wavelength analysis of the radio halo and the relic in the cluster A2256 is presented. An image of the radio halo and the relic in A2256 at 150 MHz using the GMRT is presented. Using this image with the images produced at 350 (WSRT) and 1369 (VLA) MHz, spectral index images of the radio halo and the relic were constructed. These were analysed and interpreted in the turbulent reacceleration scenario. These spectral index images show

a distribution of flat spectral index ($S \propto \nu^{-}\alpha$, α in the range 0.7 to 0.9) plasma in the NW of the cluster centre. Regions showing steep spectral indices (α in the range 1.0 to 2.3) are toward the SE of the cluster centre. These spectral indices indicate synchrotron life times for the relativistic plasmas in the range 0.08 - 0.4 Gyr. We interpret this spectral behaviour as resulting from a merger event along the direction SE to NW within the last 0.5 Gyr or so. Furthermore, the diffuse radio emission shows spectral steepening toward lower frequencies. This low frequency spectral steepening is consistent with a combination of spectra from two populations of relativistic electrons created at two epochs (two mergers) within the last ∼0.5 Gyr. For the first time, the properties of low frequency spectrum are interpreted in the context of multiple mergers in the cluster. The example of A2256 is used to point out the futility of correlating the average temperatures of thermal gas and the average spectral indices of diffuse radio emission in clusters.

Chapter 3: The chapter 3 consists of a low frequency study of the diffuse radio emission in the cluster A754. At 150 MHz, using the GMRT, 4 blobs of diffuse emission were detected – one of which is a new steep spectrum ($\alpha > 2$, $S \propto \nu^{-\alpha}$) feature. Among other three blobs one was detected at all the three frequencies (150, 330 and 1400 MHz) and it is located along the proposed merger axis (Zabludoff et al 1995) in A754 and 0.7 Mpc away from the peak of X-ray emission; we refer to it as a relic. We have made use of the framework of adiabatic compression model (Ensslin & Gopal-Krishna 2001) to model the spectra. We show that the spectrum of the relic is consistent with that of a cocoon of a radio galaxy lurking for $\sim 9 \times 10^7$ yr; no shock compression is required. The other three diffuse emission have spectral indices steeper than 1.5 and could be cocoons lurking for longer time. We discuss other possibilities such as shocks and turbulent reacceleration being responsible for the diffuse emission in A754.

Chapter 4: A multi-frequency (150, 240, 330, 610 and 1400 MHz) study of radio relics associated with the galaxy clusters A4038, A1664 and A786 is presented. Spectacular plumes of steep spectrum ($\alpha > 1.5$, $S \propto \nu^{-\alpha}$) radio emission are detected in the low frequency (150, 240 and 606 MHz) images of the relic in A4038. The adiabatic compression model fit to the spectrum is consistent with that of a

shock compressed cocoon with a time ~ 0.3 Gyr spent in the relic phase. A Mach number ~ 2 is estimated. The relic in A1664 is imaged at 150 and 330 MHz. The spectral index of the relic is ~ 1 between 150 and 1400 MHz and the model fit is consistent with that of a cocoon lurking for 0.04 Gyr. The relic in A786 is imaged at 150, 350, 610 and 1400 MHz. The model fit is consistent with that of a cocoon lurking for 0.06 Gyr.

Chapter 5: In this chapter a sample of ultra-steep spectrum sources identified from the VLSS and the NVSS is imaged using the VLA and the GMRT. The detailed images indicate double lobed morphologies for these sources but there is no evidence for cores or jets. Most of these sources appear to be dead double radio sources. Two of these sources are cospatial with galaxy clusters identified from the ROSAT observations. Neither of the two are giant radio halos or Mpc scale relics at cluster peripheries. Spectral fits to these relics imply that these sources have been in relic phase as long as these were in the active phase. This property makes this sample of relics the first of its kind. The current data allowed estimates of the relic and the continuous injection timescales to 3σ errors of 30% and 50% respectively. The mean redshift of 4 of the 10 sources reported here is ~ 0.2. At a redshift of 0.2, the linear extents of the sources in the current sample are ~ 250 kpc with their spectral luminosities at 1.4 GHz in the range 2-25 x 10^{23} W Hz^{-1}. The steep spectra of these sources are a result of the cessation of AGN activities in them about 15 – 100 million years ago. Before the cessation of AGN activity, the radio luminosities of these galaxies were ~ 1000 times brighter than their current luminosities and would have been 10-100 times brighter than that of the brightest active radio galaxies detected in the local universe ($L_{1.4} \sim 10^{27}$ W Hz^{-1}). Quantifying the abundance of such a population has important implications to the life cycle of the AGN.

Chapter 6: A discussion of the work in this thesis in the context of the larger picture is presented. Possible directions for future research are indicated.

Chapter 2

Spectral Index Studies of Diffuse Radio Emission in Abell 2256: Implications for Merger Activity

Kale. R. & Dwarakanath, K. S. 2010, ApJ, 718, 939

2.1 The galaxy cluster Abell 2256

A2256 is a rich, X-ray luminous ($L_{X[0.1-2.4keV]} \sim 7 \times 10^{44}$ erg s^{-1}, Ebeling et al 1996) galaxy cluster at a redshift of 0.0581 (Struble & Rood 1999). The X-ray surface brightness is elongated in the east-west direction and shows substructures (Briel et al 1991; Sun et al 2002); the radial velocity distribution of galaxies shows the presence of three distinct groups of galaxies (Berrington et al 2002). These have been interpreted to be indicators of ongoing merger in A2256. Recent temperature maps of A2256 with *Chandra* (Sun et al 2002) and *XMM-Newton* (Bourdin & Mazzotta 2008) show variation between 4 - 10 keV in ~ 0.6 Mpc region around the cluster centre. Apart from several head-tail radio galaxies, A2256 hosts diffuse radio emission in the north-west of the cluster centre (the radio relic) and at the centre (the radio halo). It has been studied in radio wavelengths for the

past three decades (Bridle & Fomalont 1976; Bridle et al 1979; Rottgering et al 1994 (hereafter R94); Clarke & Ensslin 2006 (hereafter CE06); Brentjens 2008 (hereafter B08)). Polarization of $\sim 20 - 40\%$ was detected at 1400 MHz in the relic by CE06; at 350 MHz it is unpolarized ($< 1\%$) (B08). A2256 also hosts the peculiar steep spectrum source 'F'; the optical identification of it is still being debated (B08). New steep spectrum sources have been detected in the 330 MHz images of A2256 made using the GMRT by van Weeren et al (2009); these are at the periphery of the cluster and are unrelated to the halo and the relic that will be discussed in this chapter.

Study of the integrated spectrum (including the radio galaxies, the compact radio sources as well as the diffuse radio emission) of A2256 has shown that it steepens at low frequencies (B08); a property unique to this cluster. The properties of the relic in A2256 are inconsistent with the scenario of acceleration in structure formation accretion shocks (Ensslin et al 1998). They propose a shock radius of ~ 1 Mpc for the geometry of the relic in A2256, which implies an origin in shocks interior to the cluster – the merger shocks. Based on the simulations of Roettiger et al (1995), a merger between clusters having mass ratios 2:1, in the direction northwest to southeast, such that the smaller cluster is moving towards the observer has been discussed in the case of A2256. This model was proposed to explain the X-ray properties and temperature distribution in A2256 as estimated by *ROSAT* (Briel & Henry 1994); further sensitive X-ray measurements (*ASCA, Chandra, XMM Newton*) do not confirm the measurements of temperature by the *ROSAT* (Sun et al 2002; Bourdin & Mazzotta 2008); rendering the model unusable. Based on X-ray substructure and identification of three distinct groups of galaxies in A2256, two mergers have been discussed (Sun et al 2002; Berrington et al 2002; Miller et al 2003). Berrington et al (2002) propose two mergers – one between two comparable mass subclusters and another between a group and the primary cluster. Miller et al (2003) have favoured the possibility of the group being responsible for the radio relic whereas CE06 favour the merger of two subclusters. The case of A2256 is complex. The spectral distribution across the diffuse radio emission in A2256 is presented in this chapter and its implications to the mergers are discussed.

We adopt a Λ-dominated cosmology with a Hubble constant, H_0, of 73 km s^{-1} Mpc^{-1}, $\Omega_M = 0.27$ and $\Omega_\Lambda = 0.73$ which implies a distance scale of $\sim$ 70 kpc arcmin^{-1} at the redshift of A2256.

2.2 Radio Observations and Data Reduction

2.2.1 GMRT Data

The observations of A2256 were carried out with the GMRT (Oct. 2007) at 150 MHz for a duration of $\sim$ 7 hr with a bandwidth of 6 MHz. The Astronomical Image Processing System (AIPS) was used to analyse this data. The GMRT data at 150 MHz are affected by radio frequency interference (RFI). Using the data visualization and editing tasks in AIPS, data affected by RFI were identified and removed. About 35% of the data were excised. Standard procedures of absolute flux density, gain and bandpass calibrations were carried out. This calibrated data were imaged and several self-calibration iterations were performed to obtain the best images. Use of uniform and natural weighting of the visibilities resulted in images at 150 MHz at resolutions of 21″ and 33″ with rms sensitivities of $\sim$ 2.2 and $\sim$ 2.5 mJy beam^{-1}, respectively. The 150 MHz image with a resolution of 21″ of the A2256 field is presented in Fig. B.1.

A2256 was also observed at 610 MHz using the GMRT (Aug. 2007) for a duration of 5 hr with a bandwidth of 32 MHz. These data were also reduced using AIPS. An image with a synthesized beam of 23″ $\times$ 22″ (PA 0.9°)and an rms of 0.8 mJy beam^{-1} was produced at 610 MHz. The uv-coverage at 610 MHz was not sufficient to detect the extended low surface brightness regions of the radio halo and the relic in A2256. The central portion of this image is presented in Fig. B.2.

2.2.2 Archival Data

Data in the form of visibilities at 1400 MHz (project code AC522) were obtained from the archives of the Very Large Array (VLA). This data contained observations for a duration of 6 hr with the VLA in the D configuration. A bandwidth of 25 MHz at each of the 2 intermediate frequencies (IFs), namely, 1369 and 1417 MHz, was used in these observations. Images at each of 1369 and 1417 MHz are published (Fig. 1, top two panels in CE06). CE06 have detected the largest extent of the diffuse emission in the image at 1369 MHz and thus this frequency was chosen to obtain an image for our purpose. Visibilities at 1369 MHz were edited, calibrated and imaged using AIPS. Natural weighting of the visibilities resulted in an image at 1369 MHz with a resolution of $67''$ and an rms of 0.07 mJy beam^{-1}. This image is similar in terms of rms and detection of extended sources to that in Fig. 1 in CE06 (rms $\sim$ 0.06 mJy beam^{-1}; beam $\sim 52'' \times 45''$).

Visibilities recorded in frequency bands around 350 MHz containing observations of A2256 were obtained from the Westerbork Synthesis Radio Telescope (WSRT) archives. This data contained $\sim$ 11 hr observations of A2256 with the WSRT in a configuration with the shortest baseline of $\sim$ 72 m. These visibilities were recorded in 8 frequency bands, between 310-390 MHz, each having a bandwidth of 10 MHz. Natural weighting of the visibilities resulted in a beam $\sim 62''$ (FWHM). For easy comparison with the 1369 MHz image, a beam of $67''$ (FWHM) was chosen for imaging and an rms of 0.6 mJy beam^{-1} was achieved using visibilities in all the frequency bands. This image is similar in quality to that in Fig. 2 in B08 produced from the same data set. For spectral comparison, an image with a beam of $67''$ (FWHM) was produced at 150 MHz from the GMRT data.

2.2.3 Primary Beam Corrections

Primary beam corrections to images at each of the frequencies were applied using the task 'PBCOR' in AIPS. At 150 MHz and 1369 MHz, the coefficients of the polynomials representing the respective primary beams reported on the GMRT and

the VLA websites were used. The primary beam of the WSRT is approximated by the function $cos^6(\theta)$, where θ is a function of the frequency and the angular distance from the pointing centre. Using this function, parameters for the task 'PBCOR' appropriate for the WSRT were calculated and used (See Appendix C for details). These primary beam corrected images were used for obtaining spectral index images between these frequencies.

2.3 Results

2.3.1 Radio Images

The central portion of the GMRT 150 MHz image of the A2256 region at a resolution of $67'' \times 67''$ is presented in Fig. 2.1. This image shows sources with extents ranging between $\sim 67''$ and $\sim 15'$. The sources are labelled according to the convention in Bridle et al (1979) and R94 for easy reference (also see the 610 MHz image (Appendix B, Fig. B.2) for locating the discrete radio sources). The radio sources A, B, C and D are radio galaxies with optical counterparts in A2256 (R94; Miller et al 2003). The sources A, B, C, D and F have extents ranging between $\sim 67''$ and $\sim 6'$. The source F is an extended ultra-steep spectrum source (Masson & Mayer 1978; Bridle et al. 1979; R94). The extent of source F at 150 MHz is $\sim 4'$ which is ~ 280 kpc if it is at the redshift of A2256. The identification of source F as a radio tail of optically identified galaxy 122 of Fabricant et al (1989) is still being debated (B08).

The sources G and H are extended ($\sim 10'$) sources and are together termed as the "radio relic" in A2256 (R94). High resolution ($\sim 1.4'' \times 1.2''$) 20 cm maps with the VLA in the A configuration by R94 resolve out G and H completely; thus confirming their diffuse nature. No unique optical counterpart can be associated with these sources (Miller et al 2003). The radio relic seen at 150 MHz, covers a region of $\sim 1 \times 0.4$ Mpc^2. CE06 have reported an extent of $\sim 1.125 \times 0.52$ Mpc^2 for the relic. The larger extent reported by CE06 and also detected in our 1369

MHz image covers a region of extent $\sim$ 100 kpc toward the northwest and north of the boundaries of the relic shown in Fig. 2.1. The surface brightness of this $\sim$ 100 kpc region is $\sim$ 0.4 mJy arcmin^{-2} at 1400 MHz (CE06). This surface brightness implies a surface brightness of 2.4 mJy arcmin^{-2} at 150 MHz assuming a spectral index of -0.8 ($S \propto \nu^{-\alpha}$). This is $\sim$6 times lower than the sensitivity in the 150 MHz image presented here. The diffuse emission pervading the central region around source D is the "radio halo" (CE06). The radio halo and the relic emission overlap and thus it is difficult to determine the exact extents of each. The region toward south-east that is detected at 1369 MHz by CE06 ($\sim$ 0.2 mJy arcmin^{-2}) and at 350 MHz by B08 is beyond the SE boundary shown in Fig. 2.1 and is not detected at 150 MHz due to its low surface brightness ($\sim$1.2 mJy arcmin^{-2} at 150 MHz).

2.3.2 Integrated spectrum

The total flux densities inclusive of the radio halo, the radio relic and the discrete sources are 10.0 ± 1.5, 3.6 ± 0.1 and 1.47 ± 0.07 Jy at 150, 350 and 1369 MHz, respectively. The total flux densities were measured using the same area at all the three frequencies. In Table 2 of B08, total flux density measurements of A2256 at frequencies ranging from 22.25 to 2695 MHz have been reported. Our estimates at 350 and 1369 MHz are within $\sim 1\sigma$ errors of the values reported by B08. The total flux density recovered at 150 MHz is $\sim$ 25% higher than that reported by B08 (8.1 ± 0.8 Jy at 151 MHz from Masson & Mayer 1978). These total flux density estimates imply spectral indices of $\alpha_{150}^{350} = -1.20 \pm 0.06$ and $\alpha_{350}^{1369} = -0.65 \pm 0.01$ for the integrated spectrum of A2256. Total flux densities of 17 ± 2 Jy at 81.5 MHz (Branson 1967) and 3.51 ± 0.06 Jy at 351 MHz (B08) imply a spectral index of $\alpha_{81.5}^{351} = -1.08 \pm 0.06$. Our estimate of spectral index between 150 and 350 MHz is consistent within 1σ error with this low frequency spectral index. The total flux density of A2256 at 1369 MHz is not available in CE06. Using the total flux density estimate at 351 MHz from B08 and our estimate at 1369 MHz, the spectral index of A2256 is $\alpha_{351}^{1369} = -0.63 \pm 0.01$; our estimate ($\alpha_{350}^{1369}$) is consistent within 1σ error.

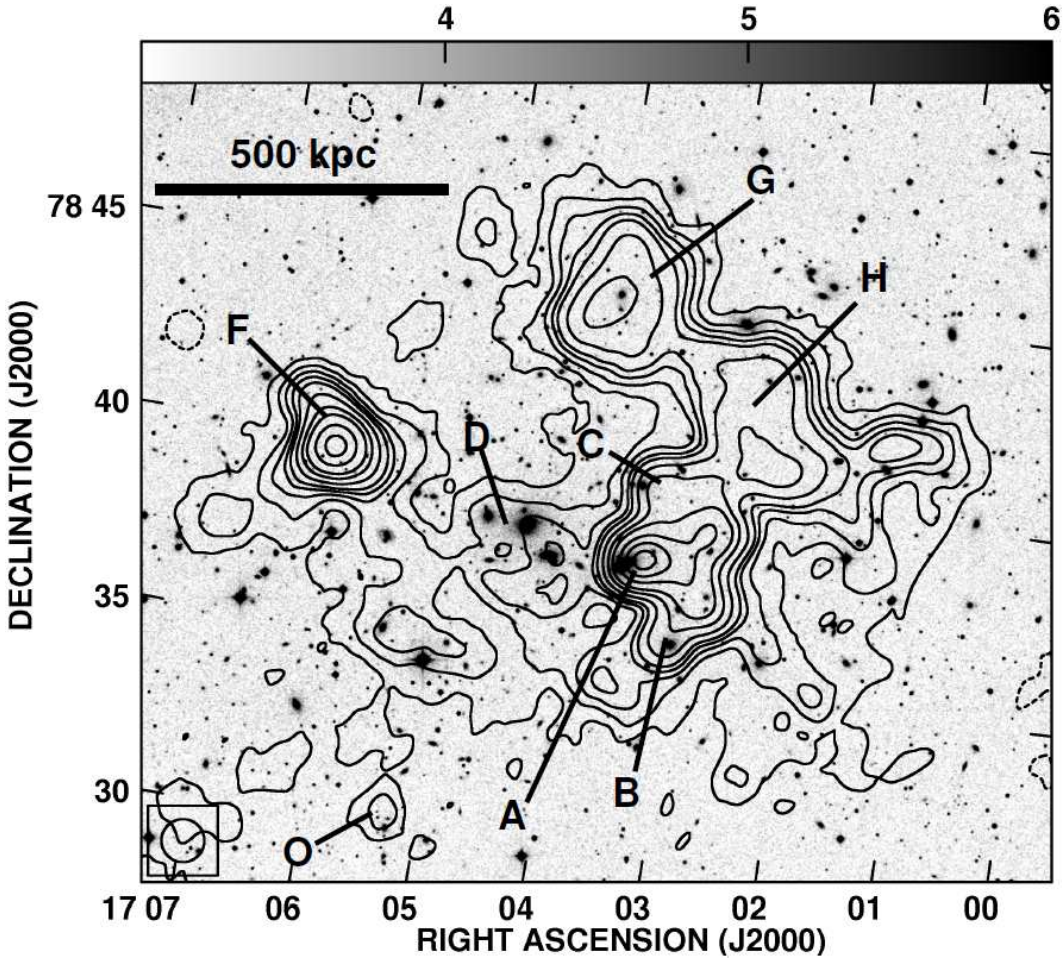

FIGURE 2.1: A2256: GMRT 150 MHz image with a synthesised beam of $67'' \times 67''$ and an rms of 3.6 mJy beam^{-1} . Contours are at -18, 18, 36, 54, 72, 90, 126, 180, 240, 360, 480, 600 mJy beam^{-1}. The DSS R band image is shown in greyscale. The linear scale is marked for an assumed redshift of 0.058. The labels A, B, C, D, F, O, G and H for the radio sources are according to the convention in Bridle et al (1979) and R94.

2.3.3 Spectral index maps

The uv- coverages at 150, 330 and 1369 MHz were comparable. The (u,v)-plane was sampled sufficiently to short baselines $\sim$0.1 kλ to image extents of $\sim 20'$ at the three frequencies. With the use of the VLA-D configuration at 1369 MHz, the WSRT at 350 MHz and the GMRT at 150 MHz, such a uv-coverage could be achieved. Total flux densities were recovered at all the frequencies and thus these images were considered suitable for producing spectral index maps. The spectral index maps of A2256 were obtained using the primary beam gain corrected images produced at 150, 350 and 1369 MHz having resolutions of $67'' \times 67''$. Pixels having

flux densities less than 5σ level in the respective images were blanked before making spectral index maps to minimise uncertainties. Thus, pixels having flux densities less than 18 mJy beam^{-1} at 150 MHz, 3 mJy beam^{-1} at 350 MHz and 0.3 mJy beam^{-1} at 1369 MHz were blanked. To obtain the spectral index map of the radio halo and the relic, subtraction of the radio sources (A, B, C, D and F) contaminating the diffuse emission was attempted. Visibilities of short baselines were excluded to obtain images of only the discrete sources. Such images were subtracted from the respective images made using all the visibilities at each of the frequencies. This procedure resulted in either a partial subtraction of the relic or an incorrect subtraction of the discrete sources. As an alternative, models including upto 4 Gaussian components were used to fit the discrete sources. Those were subtracted from the images. This subtraction also resulted in artefacts in the images. The discrete sources have complex structures and require sophisticated modeling. To minimise the uncertainties, no discrete sources were subtracted from the final maps that were used in making the spectral index maps. The positions of discrete sources will be kept in mind while discussing the spectra of diffuse sources.

We present the spectral index maps of A2256 in Fig. 2.2 and the corresponding error maps in Fig. 2.3. The extent of the spectral index map between 150 and 350 MHz (Fig. 2.2, right) is limited by the emission detected at 150 MHz. As can be seen in the spectral index error maps (Fig. 2.3), the typical error in each of the spectral index maps is < 0.10. The error is uniform except at the edges of the radio emission where it is between 0.2 and 0.3 in the 350-1369 MHz spectral index error map (Fig. 2.3, left) and between 0.2 and 0.5 in the 150-350 MHz spectral index error map (Fig. 2.3, right).

Before studying the spectra of the diffuse radio emission, we examined the spectral behaviour of the discrete sources for consistency with earlier measurements. The discrete sources, except F, have spectral indices $\sim -0.7 \pm 0.1$ which are typical of radio galaxies and can be seen in Fig. 2.2. The components of the source F, namely F1, F2 and F3, discussed in detail by B08 are marked in the spectral index maps (Fig. 2.2) . The source F2 has spectral indices of $\alpha_{350}^{1369} = -1.80 \pm 0.05$ and $\alpha_{150}^{350} = -1.10 \pm 0.05$. These values of spectral indices of F2 are consistent with

the values $\alpha_{610}^{1446} = -1.71 \pm 0.08$ and $\alpha_{150}^{350} = -1.20 \pm 0.05$ obtained by B08. The tail of source C extends in the north-west direction and is visible in the spectral index map (Fig. 2.2, left) as a linear feature. The spectral index, α_{350}^{1369}, gradually steepens from $\sim -0.8 \pm 0.1$ near the head (marked C) to $\sim -1.20 \pm 0.05$ in the tail. Such a spectral steepening from the head towards the lobes has been seen in radio galaxies and is believed to be due to spectral ageing. Bridle et al (1979) term the tail of C as source "C(ii)" and report a spectral index of -1.04 ± 0.13 between 610 and 1415 MHz. Our estimate is consistent with that of Bridle et al (1979). Note that the discrete source O has a spectral index ~ -0.7 over the range of 150 to 1369 MHz (Fig. 2.2) as expected. Source L is not detected at 150 MHz. While discussing the spectral indices of diffuse emission, the regions having large errors ($\sim 0.4 - 0.5$, see Fig. 2.3 for error maps) are not considered. A complex distribution of spectral indices is seen over the extent of the diffuse radio emission (Fig. 2.2). Occurrence of flat spectral indices ($\alpha \sim -0.7$ to -0.9) is noticed in the northwest (NW) regions marked G and H of the diffuse emission. Towards southeast (SE) of the discrete source D the spectra are steeper ($\alpha \sim -1.2$ to -2.3). To establish the significance of this trend, six slices across each of the spectral index maps in the direction NW-SE (approximately 30° clockwise from the north) separated by $2'$ from each other in the perpendicular direction were taken. Plots of spectral index versus distance from the SE edge of the diffuse radio emission were produced. Towards the NW, the diffuse radio emission shows average spectral indices of $\alpha_{350}^{1369} \sim -0.8 \pm 0.05$ and $\alpha_{150}^{350} \sim -0.9 \pm 0.2$. Toward SE of the source D, the average spectral indices are $\alpha_{350}^{1369} \sim -1.4 \pm 0.1$ and $\alpha_{150}^{350} \sim -2.3 \pm 0.2$.

As noted in earlier works the integrated spectrum of A2256 which included the diffuse as well as discrete sources showed steepening at lower frequencies (B08). To find out whether such a steepening occurs in the diffuse radio emission, independent regions, each having a size of the synthesised beam, were chosen along the SE-NW direction (broken line in Fig. 2.2, right). The regions affected by the discrete sources were avoided. Flux densities of the chosen regions at each of 150, 350 and 1369 MHz were estimated from the images and plotted. These spectra are presented in Fig. 2.4. The flux densities have been scaled and shifted along

the y-axis such that the topmost spectrum is of the region extreme NW and the spectrum at the bottom is of the region extreme SE. It was found that each of these independent patches of diffuse radio emission have steeper spectral indices between 150 and 350 MHz as compared to that between 350 and 1369 MHz; except for the extreme NW where the spectrum is straight. From the NW to the SE, α_{150}^{350} steepens from -0.60 to -2.30. The value of α_{350}^{1369} shows mild variation in the first 3 curves from the top (Fig. 2.4) but steepens to -1.23 further towards SE edge. It was also noted that the difference, $|\alpha_{150}^{350} - \alpha_{350}^{1369}|$, increases from NW to SE (Fig. 2.4).

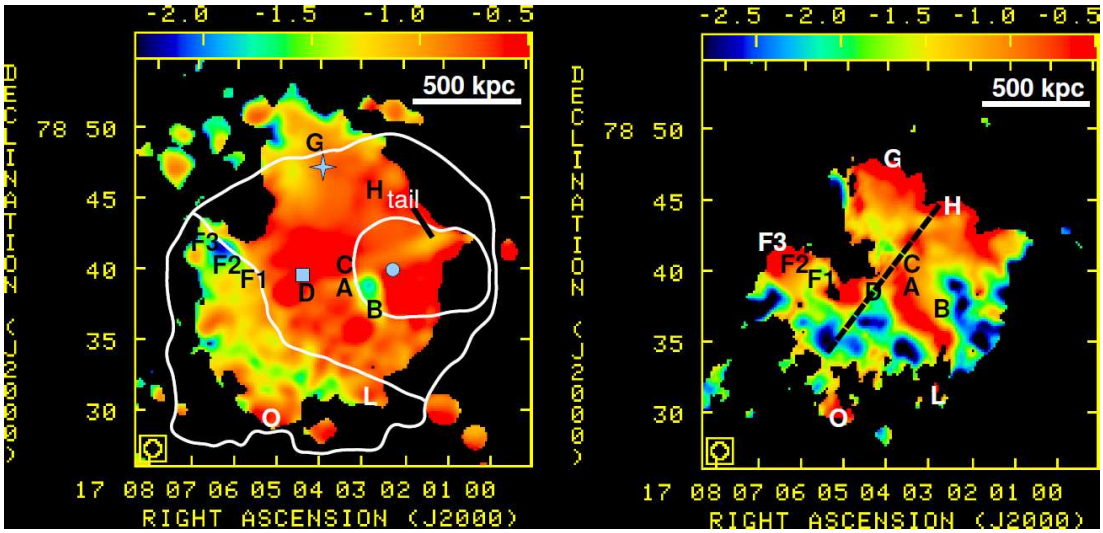

FIGURE 2.2: Colour represents the spectral index of radio emission in A2256 between 350 and 1369 MHz(*left*) and between 150 and 350 MHz (*right*). The synthesized beam is $67'' \times 67''$. The symbols square, circle and star (left panel) represent the centroids of the primary cluster, the sub-cluster and the group, respectively (Berrington et al 2002). In the left panel, the white contours are a schematic representation of regions at different temperatures (Bourdin & Mazzotta 2008). Contours enclose regions with temperatures of 4-6 keV (innermost), 6-8 keV (region surrounding the innermost region) and 8-10 keV (region toward SE) respectively.

2.4 Discussion

Most galaxy clusters with radio halos and relics also show signatures of recent or ongoing merger activities (Ferrari et al 2008). The cluster A2256 is a complex

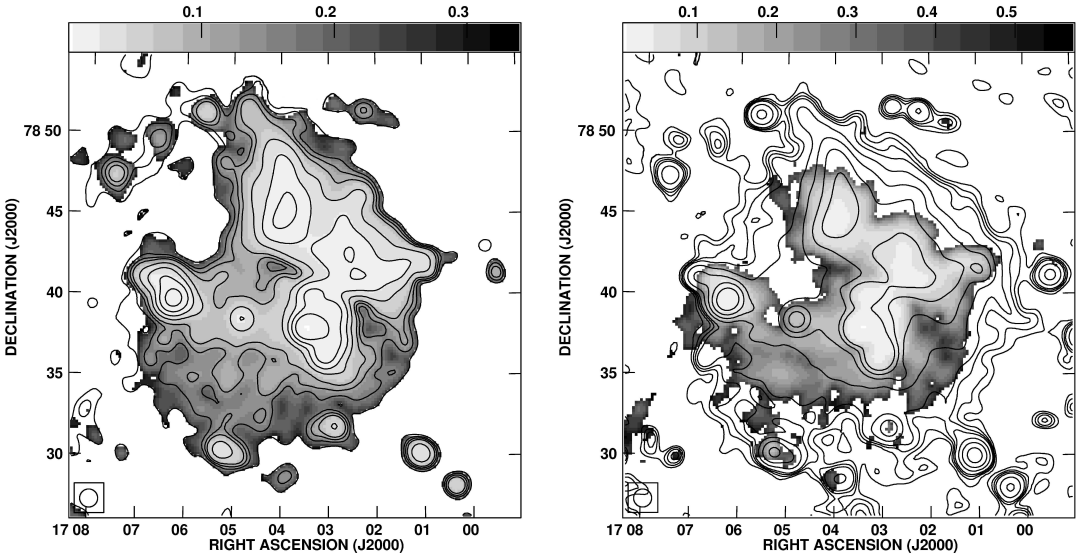

FIGURE 2.3: Spectral index error maps in greyscale. *Left* 350-1369 MHz. *Right* 150-350 MHz. Overlaid are the images at 350 and 1369 MHz in the left and the right panels respectively. Synthesized beams in both the panels are $67'' \times 67''$. Contours (starting at 5σ) are at: *(Left)* 3.0, 4.8, 6.6, 9.0, 18.0, 36.0, 72.0, 144.0 mJy beam^{-1} and *(Right)* 0.35, 0.56, 0.77, 1.05, 2.1, 4.2, 8.4, 16.8 mJy beam^{-1}.

case involving more than one merger (Berrington et al 2002; Sun et al 2002). The implications to the spectral index trends in the diffuse radio emission in A2256 from the proposed origins in merger shocks and/or in turbulence are explored further here. The diffuse radio emission in A2256 has been referred to as the relic (G & H in Fig. 2.1) and the halo (the region S and SE of the source D in Fig. 2.1) in earlier works.

2.4.1 Spectral Index and ICM Temperature

A schematic representation of the temperature map of A2256 (Bourdin & Mazzotta 2008) is shown by the black (white in online version) contours in Fig. 2.2 (left). In A2256, the spectral index of the diffuse emission varies over the range -0.7 to -2.5 and the temperature of X-ray emitting gas varies over the range 4 - 10 keV. It is found that the steep spectrum (< -1.5) region towards the SE is co-spatial with the hottest ($\sim$ 10 keV) region in the cluster. The NW region having a flat spectrum (~ -0.8) has temperatures $\sim 4 - 7$ keV. The cluster A2256 does not show any correlation between the hot X-ray and the flat radio spectrum regions;

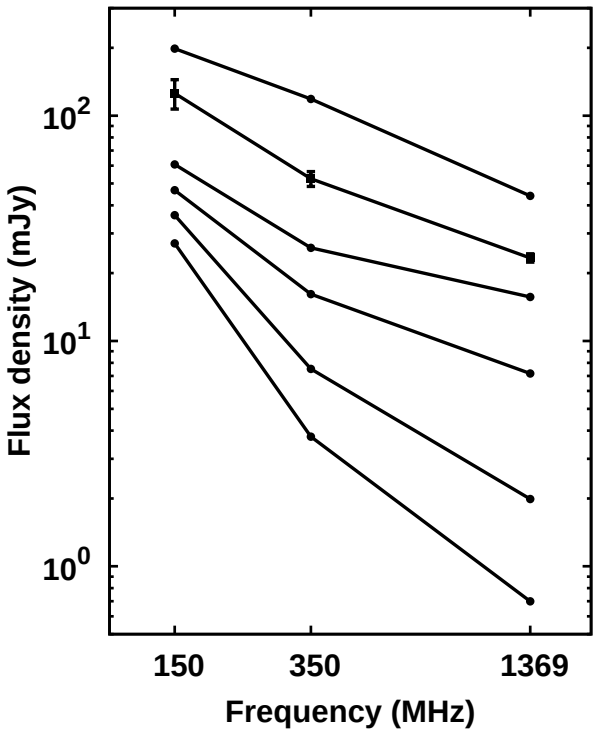

FIGURE 2.4: Spectra of diffuse radio emission from six patches spaced equally along the broken line shown in Fig. 2.2 (right panel). The spectral indices, (α_{150}^{350}, α_{350}^{1369}), for the spectra from top to bottom are: (-0.60, -0.72), (-1.03, -0.59), (-1.00, -0.36), (-1.25, -0.59), (-1.85, -0.97) and (-2.30, -1.23). Typical errors are indicated in the second spectrum from the top for which there is no scaling in the flux density. All other spectra are shifted along the y-axis.

in fact the SE region is a clear anti-correlation. Cooling times of thermal gas in merging clusters are typically more than the lifetime of the cluster (Hubble time) (Buote 2002). Synchrotron cooling times are at least 10-100 times shorter than a Gyr for break frequencies in the GHz range and typical intra-cluster magnetic fields. The thermal plasma will essentially be at the same temperature while the synchrotron spectrum ages (steepens) and finally fades.

Earlier studies have explored possible correlations between the temperature of the thermal gas and the spectral indices of radio halos confined in them. Feretti et al (2004) report the absence of one to one correspondence between the high

temperature and the flat (~ -0.8) synchrotron spectrum regions in the radio halo in A665 and only a mild correspondence in A2163. This can be easily understood by comparing the cooling time of the thermal plasma and that of the synchrotron plasma. Recently, Giovannini et al (2009) have reported a mild correlation between the average temperatures of the ICM and the average spectral indices of the radio halos in the respective clusters. As seen in A2256, the temperature varies over a range of 4 - 10 keV and the spectral index varies over a range of -0.7 to -2.5. Similar variations have been found in other clusters (Feretti et al 2004; Govoni et al 2005; Bourdin & Mazzotta 2008) too. Therefore comparing the average values of ICM temperatures and of spectral indices of radio halos in respective clusters can be misleading. Moreover, the estimates of temperatures in clusters and the co-spatial occurrence of radio emission and hot gas are affected by projection effects.

2.4.2 Spectral index and cluster dynamics

The implications of the properties of the complex spectral index distribution in A2256 to the geometries and timescales of mergers are discussed here. The diffuse radio emission in A2256 shows the presence of two regions in spectral index maps. A region NW of the discrete sources A, B and D with flat spectral indices and another SE of these sources having steep spectral indices (Fig. 2). In order to estimate spectral age of radio emission a knowledge of the magnetic field in that region and of the break frequency is required. In A2256, the estimates of magnetic field based on the depolarization properties of the filament G in the NW are in the range 0.02 - 2 μG (B08) and those of the SE region based on the classical minimum energy, equipartition and hadronic minimum energy conditions range between $1.5 - 8\mu$G (CE06). For simplicity, a typical value of 1μG for cluster magnetic field (Carilli & Taylor 2002) is used. Synchrotron spectrum is curved and requires measurements at several frequencies, over the entire range from a few MHz to tens of GHz, to identify the break frequency. Flux density estimates of regions within the diffuse radio emission in A2256 are available from the images at 150, 350 and 1369 MHz as presented in this chapter; the break frequencies cannot

be identified using these. However, from the spectral indices, upper and lower limits on the break frequencies of different regions in the diffuse radio emission can be estimated. The values of spectral indices in the NW and the SE regions discussed in Sec. 2.3.3 imply that 1369 and 150 MHz can be considered as the lower and the upper limits on the break frequencies of these regions, respectively. Using these break frequencies, the upper and lower limits on the spectral ages of the NW and of the SE regions of the diffuse radio emission are $\sim$ 0.08 and 0.4 Gyr, respectively. The spectral ages imply that the radio emission in the NW relic region is young and the acceleration is very efficient. The relic could be the present location of a shock front. One possibility is that a cluster merger in the direction SE to NW drove shocks and injected turbulence in the ICM along its way. Cluster merger shocks can accelerate particles to relativistic energies (Ensslin et al 1998; Hoeft & Bruggen 2007). But the distances to which the shock accelerated particles can diffuse within their radiative lifetimes are short ($\sim$ 200 kpc, see Brunetti et al 2008). Thus shock acceleration alone cannot be responsible for the Mpc scale radio emission as seen in A2256. However, the relic region having a sharp edge at the NW and a projected width of $\sim$ 300 kpc towards the SE could be the result of shock acceleration.

The reasons for the possibility of shock acceleration in the relic region are as follows. An average linear polarization fraction of $\sim$ 20% has been detected across the relic at 1.4 GHz with the averaged B-vector oriented with an angle 10° (measured east of north) (CE06). In the region of shock, the magnetic fields become alligned with the shock plane. Based on the polarized fraction in the relic, CE06 propose that the shock plane is alligned at an angle of $\sim$ 45° with the plane of the sky. This orientation is consistent with the SE to NW direction in which the shock is likely to have propagated based on the spectral ages discussed above. At the location of the shock, which is the site of reacceleration, flat spectral indices are expected and gradually in the wake of the shock, the spectra would be steeper. The relic has a flat spectral index of $\alpha \sim -0.7$ between 150 and 1363 MHz but shows a gradual steepening from NW to SE in the frequency range 1363 -1700 MHz (CE06).

It should be noted that there is no evidence for a shock in A2256 from the X-ray observations with *Chandra* and *XMM-Newton* (Sun et al 2002; Bourdin & Mazzotta 2008). Viewing angle can be a reason for the non-detection of shock in X-rays. Nevertheless there is evidence for mergers in A2256. The distributions of the optical galaxies and of the X-ray emission in A2256 show substructures which are believed to be due to 2 merger events (Berrington et al 2003; Sun et al 2002). Based on the optical substructure, Berrington et al (2003) propose two mergers in A2256. One is a merger between the primary cluster (PC) and the sub-cluster (SC) and another between a group (Gr) and the combined system of PC and SC or the PC. The symbols box, circle and star (Fig. 2.2, left) indicate the positions of the optical centroids of the PC, the SC and the Gr, respectively. The estimates of mass for the PC, the SC and the Gr are $1.6\times10^{15}M_{\odot}$, $0.51\times10^{15}M_{\odot}$ and 0.17 $\times10^{15}M_{\odot}$, respectively. Of the two mergers one is major merger (PC+SC, mass ratio ~ 3) and another is a minor merger (PC+Gr or (PC+SC)+Gr, mass ratio ~ 10). Numerical simulations have shown that mergers with mass ratios $\sim 3-10$ can give rise to shocks of Mach numbers $\sim 1.5-3$, but these are not sufficient for accelerating particles that are responsible for observed synchrotron emission (Gabici & Blasi 2003). Thus, even in the region of the relic in A2256, mechanisms other than shock acceleration may be active.

Turbulent reacceleration is a mechanism by which Mpc scale radio emission can be generated in clusters of galaxies (See Sec. 1.3.2). The decay time of the MHD turbulence at injection length scales ($L_{inj} \sim$ 1Mpc) can be estimated using:

$$\tau_{kk}(Gyr) \sim (\frac{v_i}{2\times10^3 kms^{-1}})^{-1}(\frac{L_{inj}}{1Mpc})(\frac{\eta_t}{0.25})^{-1} \tag{2.1}$$

where v_i is the relative velocity of impact of merging clusters and η_t is the fraction of the energy in turbulence that is in MS waves (Cassano & Brunetti 2005). The value of η_t has been constrained by requiring that the accelerated electrons can produce synchrotron emission with spectral index $\sim 1.1-1.5$ between 327 and 1400 MHz (Cassano & Brunetti 2005). The spectral index of the radio halo in A2256 is ~ 1.6 and the relative velocity between merging sub-clusters (PC+SC) is

$\sim$ 2000 kms^{-1} (Berrington et al 2002). The timescale for the decay of turbulence ($\tau_{kk} \sim$ Gyr) is comparable to the crossing time for merging subclusters. If the mergers in A2256 have occurred over the last Gyr then the presence of Mpc scale radio halo is consistent with the timescale over which the turbulence decays.

Further we compare the spectral trends and the geometries of mergers in A2256. The mean radial velocity of the Gr is $\sim$ 2000 kms^{-1} higher than that of the PC and is moving along the line of sight into the PC (Miller et al 2003). Such a merger event could lead to a shock travelling from the SE to the NW and also inject turbulence in the swept ICM if the direction of merger is inclined to the line of sight. The shock and turbulence in the NW region and the turbulence in the region that was swept by the passage of the Gr can generate diffuse radio emission. Moreover the major merger between PC and SC must also result in injection of turbulence in the ICM. The spectral index trend in the diffuse radio emission(steepening from NW to SE) is consistent with the geometry of the merger of the Gr with the PC. Miller et al (2003) point out the frequent occurrence of radio sources associated with the star forming galaxies in the Gr and interpret it as an effect of merger. Thus there is evidence for the Gr to have undergone merger in a direction into the plane of the sky; the exact orientation is not clear. Miller et al (2003) have argued that the merger of the Gr viewed 0.3 Gyr after the core passage is responsible for the diffuse radio emission in the NW of the cluster. The co-spatial occurrence of the brightest diffuse radio emission and the Gr and the direction of spectral index steepening being consistent with the proposed direction of the Gr - PC merger, support the picture of Miller et al (2003). The radiative lifetimes discussed earlier also support the passage of the Gr within the last 0.4 Gyr. If the merger between PC and SC has been in progress for the past Gyr it will contribute to enhance the radio emission but its role in producing the spectral index distribution is not clear. Another possibility is that the amount of energy that was injected as fluid turbulence in different regions is different and thus has resulted in flat spectrum emission in one region and steep spectrum emission in another. The dependence of acceleration by turbulence on

the many unknown parameters mentioned earlier make further progress in testing this possibility difficult.

The group Gr, being less massive and not being part of a major merger in A2256 is not favoured by CE06 to have created the radio emission in the NW region. Instead, CE06 have proposed two scenarios involving the major merger between the PC and the SC (see Fig. 11 a and 11 b in CE06); in both the scenarios the SC approaches the PC from the NW in projection on the plane of the sky. In the first scenario the SC approaches the PC from the NW and is proposed to be in the early stages of merger. In this picture the merger shock crosses from the NW to the SE or is along the line of sight towards the observer (see Fig. 11a in CE06). This implies steep spectra in the NW edge and flatter spectra towards SE or a uniform distribution of spectral indices as seen by the observer, respectively. The diffuse radio emission in the SE (radio halo) is considered a remnant of an older merger (CE06). This picture is contradictory to the observed spectral steepening from the NW to the SE and does not account for the radio emission in the SE region (radio halo). In the second scenario of CE06, the SC is in an advanced stage of merging. The outgoing merger shocks are proposed to create the radio emission. One of the shock waves is along the line of sight towards the observer (Fig. 11b) and thus might result into complex spectral index distribution; it cannot explain the spectral index variation from the NW to the SE.

Apart from the trend of spectral steepening from NW to SE, the spectrum of the diffuse radio emission steepens at lower frequencies (Fig. 2.4). Since a synchrotron spectrum is expected to steepen at higher frequencies due to energy losses, this low frequency steepening in the diffuse emission cannot be explained by a single population of emitting particles. Superposition of at least two spectra having unequal amount of steepening can give rise to a spectrum that steepens at low frequencies. It is possible that the two superposing spectra are due to populations of electrons accelerated at different epochs. The two merger events in A2256 could be the two epochs at which the electrons were accelerated; the merger of SC with PC and that of the Gr with the PC and the SC. According to the models proposed to explain the X-ray substructure, the merger between the PC and the

SC is viewed 0.2 Gyr prior to the core passage and the Gr merger is viewed 0.3 Gyr after the core passage (Miller et al. 2003; Roettiger et al 1995). These timescales are consistent with the timescale of $\sim 0.08 - 0.4$ Gyr over which the radio emission remains detectable in the frequency range of 150 -1400 MHz. Due to lack of detailed simulations, the chronology between the two merger events and the exact mechanism of acceleration of electrons to relativistic energies cannot be established with confidence. Hydro/ N body simulations reproducing the optical and X-ray substructure and the temperature distribution are required to obtain the detailed geometries and the chronological order of the two mergers in A2256. An alternative possibility is that a complex distribution of turbulence and magnetic fields in the cluster may result in regions with flat and steep spectra. Such regions seen projected along the line of sight could also produce a low frequency steepening in the integrated spectrum.

The peculiar low frequency steepening trends seen in the integrated spectra of A2256 and of the diffuse radio emission in it have been discussed above. It should be noted that at high frequencies, the synchrotron spectra are expected to steepen due to energy losses. The synchrotron emission due to acceleration mechanisms such as turbulence or shocks have a cutoff due to the maximum energy that is available in turbulence or the strength of the shock. In the case of A2256, a spectral index map of the NW region (marked G and H in the Fig. 2.2 and referred to as the relic by CE06) between 1369 and 1703 MHz (Fig. 4 in CE06) is available. This spectral index map in CE06 is affected by the loss of sensitivity to extended structure at 1703 MHz due to instrumental limitations and larger noise level. Nevertheless, the spectral indices in the high surface brightness relic region can be used for comparison with our spectral index maps. The spectral index map in CE06 shows a flat spectrum ($\alpha \sim -0.9$) emission at the NW edge and a steeper spectrum ($\alpha \sim -1.6$) emission in the SE region of the relic. The same relic region (marked G and H) in our spectral index map between 350 and 1369 MHz (Fig. 2.2, left) shows flatter spectral indices ~ -0.7 to -1.0. The steeper spectral indices in the 1369-1703 MHz spectral index map in CE06 could be the effect of ageing of the synchrotron spectrum due to energy losses. Thus putting together the spectral

information across the frequency range of 150 to 1703 MHz for the NW region a picture consistent with a high frequency steepening due to the energy losses and a low frequency steepening due to a second component of electron population emerges. Further deeper observations at high frequencies (> 1.4 GHz) which can image the entire extent of the diffuse emission in A2256 are required to confirm the steepening due to energy losses.

2.5 Summary

We have presented a multi-wavelength analysis of the merging rich cluster of galaxies Abell 2256. We have observed A2256 at 150 MHz using the GMRT and successfully detected the diffuse radio halo and the relic emission over an extent ~ 1.2 Mpc^2. Using this 150 MHz image and the images made using archival observations from the VLA (1369 MHz) and the WSRT (350 MHz), we have produced spectral index images of the diffuse radio emission in A2256. These spectral index images show a distribution of flat spectral index ($S \propto \nu^{\alpha}$, α in the range -0.7 to -0.9) plasma in the NW of the cluster centre. Regions showing steep spectral indices (α in the range -1.0 to -2.3) are toward the SE of the cluster centre. These spectral indices indicate synchrotron life times for the relativistic plasmas in the range 0.08 - 0.4 Gyr. We interpret this spectral behaviour as resulting from a merger event along the direction SE to NW within the last 0.5 Gyr or so.

Furthermore, the diffuse radio emission shows spectral steepening toward lower frequencies. This low frequency spectral steepening is consistent with a combination of spectra from two populations of relativistic electrons created at two epochs (two mergers) within the last $\sim$0.5 Gyr. Earlier interpretations of the X-ray and the optical data also suggested that there were two mergers in Abell 2256 in the last 0.5 Gyr, consistent with the current findings. For the first time it has been possible to find an evidence of multiple mergers in a cluster in the spectrum of the radio emission. This study highlights the importance of spectral index maps in

different frequency bands for interpretation of the properties of the diffuse radio emission.

In this study the example of A2256 is used to point out the futility of correlating the average temperatures of thermal gas and the average spectral indices of diffuse radio emission in clusters. The variation in the spectral index of the diffuse radio emission can span a range of -0.7 to -2.5. It should also be noted that the spectral index can be different in different frequency bins due to the intrinsic curved nature of the synchrotron spectrum. Thus correlations of average spectral indices with any other average properties of the cluster should be interpreted with care.

Chapter 3

Diffuse Radio Emission in the Galaxy Cluster Abell 754

Kale, R. & Dwarakanath, K. S. 2009, ApJ, 699, 1883

3.1 The galaxy cluster Abell 754

3.1.1 X-ray and Optical Studies

A754 is a rich galaxy cluster at a redshift of 0.0542 (Strubble & Rood 1999), with an X-ray luminosity of $6.4 \times 10^{44}\ h_{75}^{-2}$ erg s^{-1} measured in the *ASCA* energy band of 0.5 - 10 keV (Henriksen & Markevitch 1996) and a temperature of 9.0 ± 0.3 keV (Wu et al 1998; Govoni et al 2004). Non-virialized nature of A754 has been inferred from the morphologies of X-ray emissions in the images made with ROSAT (Henry & Briel 1995), *Chandra* (Markevitch et al 2003) and *XMM-Newton* (Henry et al 2004). The projected distribution of optical galaxies has been reported to be bimodal and oriented along the east-west axis; the mean redshifts of the two galaxy concentrations being identical within errors (Fabricant et al 1986; Zabludoff & Zaritsky 1995, hereafter ZZ95). The peak of X-ray emission in A754 is not spatially coincident with either of the two major galaxy concentrations (ZZ95). A

merger of two sub-clusters approximately in the plane of the sky along the east-west axis has been suggested (ZZ95). Henriksen et al (1996) using *ASCA* data proposed a non-head-on collision of subclusters in A754. Roettiger et al (1998), using 3D MHD/N-body simulations, have proposed explanations for most of the observed X-ray properties of A754 by considering an off-axis merger between two smaller clusters of mass ratio less than 2.5:1. Markevitch et al (2003), based on the temperature map obtained using the *Chandra* data on A754, have suggested a complex geometry of merger involving more than two subclusters or a cool gas cloud sloshing independently from its former host subcluster. The temperature, pressure and entropy maps of A754 have been made using observations from *XMM-Newton* by Henry et al (2004). They infer a weak shock with Mach number 1.9 ± 0.4 in A754 and the merger axis to be the direction north-west to south-east. Fusco-Femiano et al (2003) have reported a 3.2σ detection of excess X-ray emission at energies above 45 keV with the *BeppoSAX* which is possibly due to the inverse-Compton emission by the relativistic plasma in the ICM of A754. Absence of cooling flow (White et al 1997; Peres et al 1998) in A754 is another property indicating the on-going dynamical activity in the cluster.

3.1.2 Diffuse Radio Emission in A754

The diffuse radio emission in A754 has been under investigation for more than 25 years. Diffuse radio emission in A754 at 2.7 GHz (Wielebinski et al 1977) and at 408 MHz (Mills, Hunstead & Skellern 1978) have been reported. The diffuse emission could not be distinguished from the blend of discrete sources due to poor resolutions of $3'-4'$ in those images. The presence of diffuse halo source in A754 at 610 MHz was also suggested by Harris et al (1980) based on the deficit in the flux recovered from the emission of discrete sources compared to the total flux reported in earlier low frequency observations. Attempts of investigating the diffuse radio emission at 330 MHz in a 40 minute observation with the VLA in B and C arrays (Giovannini et al 1999; Giovannini & Feretti 2000) failed to detect the diffuse emission due to lack of uv-coverage. The presence of diffuse emission in A754 has

been confirmed by Kassim et al(2001; hereafter, KA01) in the images made from 3 hr observations at each of 330 and 74 MHz with the VLA-C array. In a deep image of A754 at 1.3 GHz with the VLA-D array, Bacchi et al (2003; hereafter BA03) have confirmed the presence of two components in the diffuse radio emission.

A ΛCDM cosmology with $\Omega_m = 0.27$, $\Omega_\Lambda = 0.73$ and a value of 73 km s^{-1}Mpc^{-1} for the Hubble constant, H_o is used. This implies a length scale of 61.9 kpc arcmin^{-1} at the redshift of A754.

3.2 Observations at 150 MHz

GMRT observations of the A754 region at 150 MHz for a total of $\sim$ 5hr were conducted on 17 Sep. 2007. High resolution (HIRES) mode of the GMRT correlator provided frequency resolution of 31.25 kHz over a bandwidth of 8 MHz. This mode was used to minimize the effects of bandwidth smearing and for better excision of radio frequency interference(RFI). Sources 3C48 and 3C147 were used for the flux and the bandpass calibration, respectively. The source 0837-198 was used as a complex gain calibrator.

3.3 GMRT 150 MHz Data Reduction

3.3.1 RFI

Data at 150 MHz with the GMRT were adversely affected by RFI. An RFI affecting about 10 consecutive frequency channels and drifting over 2 MHz in frequency during the total 5 hr of observation was found along with other RFIs which affected certain channels for limited amount of time. While examining the visibility data from each baseline the AIPS (Astronomical Image Processing System) task SPFLG was used to remove channels affected by RFI. This minimized the loss of any good data while removing the RFI affected data. About 35% data were lost due to RFI.

3.3.2 Imaging

Polyhedron imaging with 66 facets over a region of $\sim 4 \times 4$ deg^2 was carried out to account for the non-coplanarity of the incoming wavefront within the large primary beam. Hydra A, a strong radio source, $\sim 3.5^\circ$ from the phase centre was imaged to remove the effect of its sidelobes from the field of interest.

Isoplanicity can be a poor assumption for GMRT at low frequencies like 150 MHz (Rao 2003). We checked the accuracy of positions of sources in the 150 MHz images made using data separated by a few hours. About 10 min of data at the beginning and at the end of the observation were selected. Images were made to check if there was any effect of non-isoplanicity. Positions of the sources in the entire primary beam in both the 10 min images were consistent with each other and also with those in the NRAO VLA Sky Survey(NVSS) catalogue within 1σ error of $3''$. Self calibration worked equally well for all the sources in the entire primary beam. No effects of non - isoplanicity were seen.

Use of natural and uniform weights for the visibilities resulted in images with resolutions $35''$ (FWHM) and $21''$ (FWHM) respectively.

3.4 Archival Data and Images

Data at 330 MHz from the GMRT archive were also edited and calibrated using AIPS. At 330 MHz $\sim 20\%$ data were lost to RFI. Polyhedron imaging was carried out with 32 facets over a region of $\sim 1.5 \times 1.5$ deg^2. Standard steps of self calibration were performed. Image with a resolution of $10'' \times 10''$ was produced. We used the VLA D-array data from the archive at 1363 MHz to make an image with a resolution of $50'' \times 50''$. These images using the archival data were used to estimate the contributions of unresolved sources to the diffuse emission. Images at 74 and 330 MHz(KA01) with resolutions of $316'' \times 233''$ (P. A.$= -7^\circ$) and $90'' \times 90''$ (P. A.$= 0$), respectively, were provided by N. Kassim and the image with a resolution of $70'' \times 70''$ at 1363 MHz (BA03) was provided by G. Giovannini. These images were used to study the diffuse emission. Details of the observations and the images

are given in Table 3.1.

TABLE 3.1: Summary of Observations of A754

Frequency (MHz)	Telescope	Date of obsn.	Time (min)	Synthesized beam (P.A.)	rms (mJy beam^{-1})
74(KA01[a])	VLA-C	21 Mar. 2000	180	$316'' \times 233''$[b]	200
150	GMRT	17 Sep. 2007	225	$21'' \times 21''$	2.6
330	GMRT	23 Jun. 2005	150	$10'' \times 10''$	0.6
330(KA01)	VLA-C	21 Mar. 2000	180	$90'' \times 90''$	5.3
1363(BA03[c])	VLA-D	25 Sep. 2000	180	$50'' \times 50''$	0.1

[a] KA01 = Kassim et al 2001

[b] P.A. = -7°

[c] BA03 = Bacchi et al 2003

3.5 Results

3.5.1 Radio Images

3.5.1.1 High Resolution Image of A754 at 150 MHz

The highest resolution image of A754 that was possible with our data at 150 MHz using the GMRT is presented in Fig. 3.1. The central $\sim 1.5 \times 1.5$ deg^2 is shown here although the entire primary beam of 4×4 deg^2 was imaged. The position of the peak of the X-ray emission associated with A754 is marked by a '+' in Fig. 3.1. Radio galaxies with spectacular extended structure are marked by boxes. The contours of the radio emission in these galaxies at 150 MHz are overlaid on optical R-band images obtained from the Digitized Sky Survey (DSS) and displayed in Fig. 3.2. The galaxies in the first two panels from the left in Fig. 3.2 have bent radio jets and the one on the right is a head-tail radio galaxy.

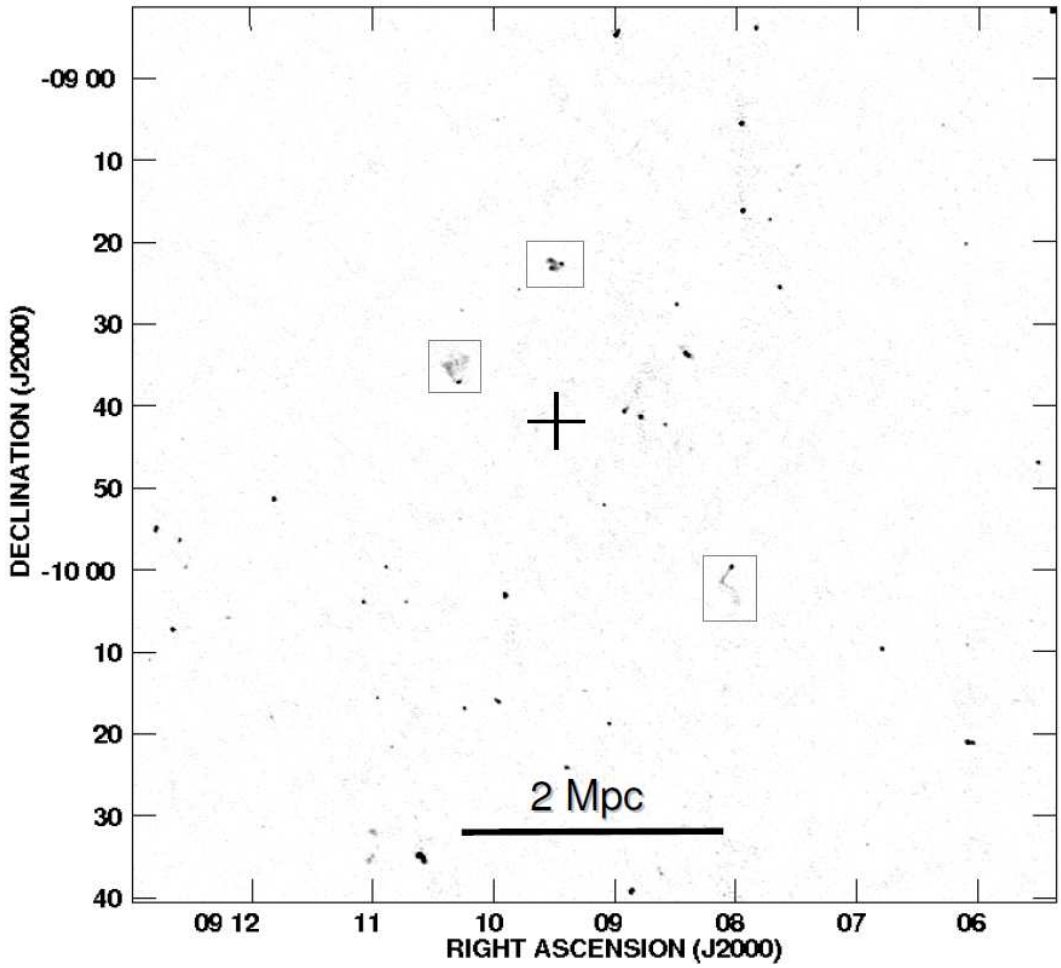

FIGURE 3.1: The GMRT image of Abell 754 at 150 MHz with an rms of 2.6 mJy beam^{-1}. The synthesized beam is $21'' \times 21''$. The grey scale flux density is in the range 0.006 - 1 Jybeam^{-1}. The length scale shown is assuming a redshift of 0.0542 for the cluster A754.

3.5.1.2 Detection of Diffuse Emission at 150 MHz

The high resolution images produced using uniform weights for the visibilities showed the detailed morphologies of radio galaxies. However the diffuse radio halo emission in the cluster was not detected due to insufficient sensitivity with the synthesized beam of 21″ (FWHM). Images with natural weights for the visibilities were produced at 150 MHz to detect the diffuse halo emission. For a comparison with the 1363 MHz image, we produced an image at 150 MHz with a beam of $70'' \times 70''$ (rms of 5.5 mJy beam^{-1}). The images of A754 at 150 MHz and at 1363 MHz (courtesy G. Giovannini) are shown in Figs. 3.3 a and b respectively. In

FIGURE 3.2: Contours of 150 MHz flux densities for 3 radio galaxies in A754 are overlaid on the DSS images of those galaxies. The synthesized beam is $21'' \times 21''$. Contours are at: (*left and middle*) 3×(-3, 3, 6, 9, 12, 15, 20, 25, 30, 35, 45) mJy beam^{-1}; (*right*) 3×(-3, 3, 6, 8, 12, 15, 20, 25, 30, 35, 45, 55, 65, 80, 95) mJy beam^{-1}. The length scales are marked assuming a redshift of 0.0542 for A754.

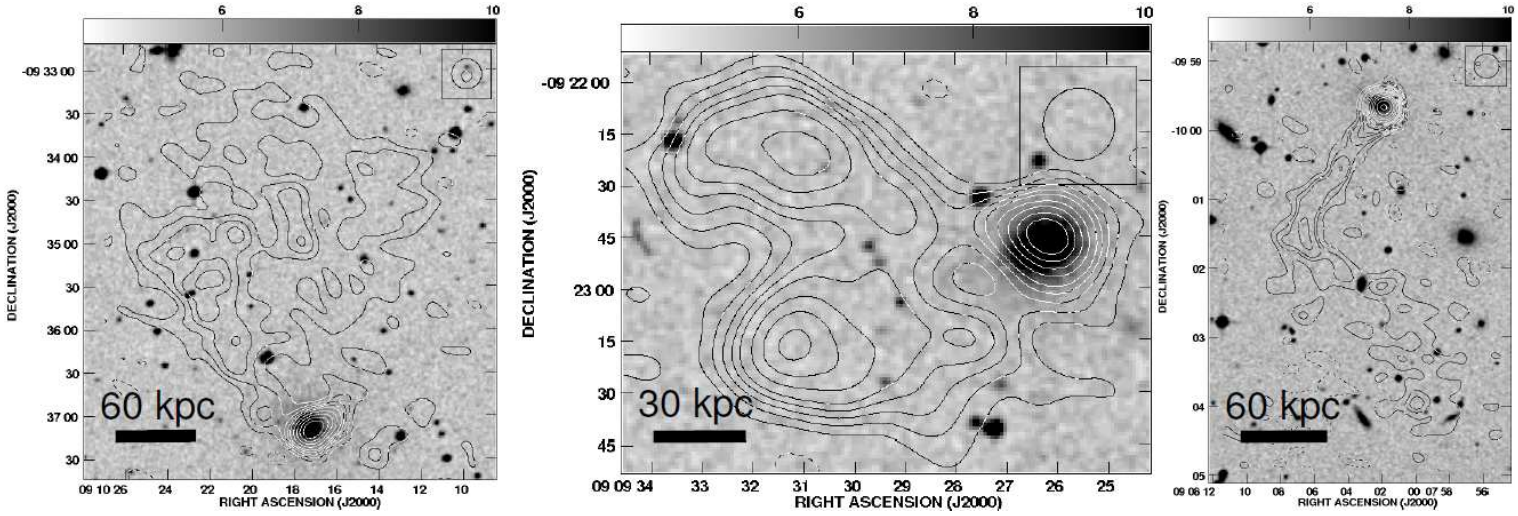

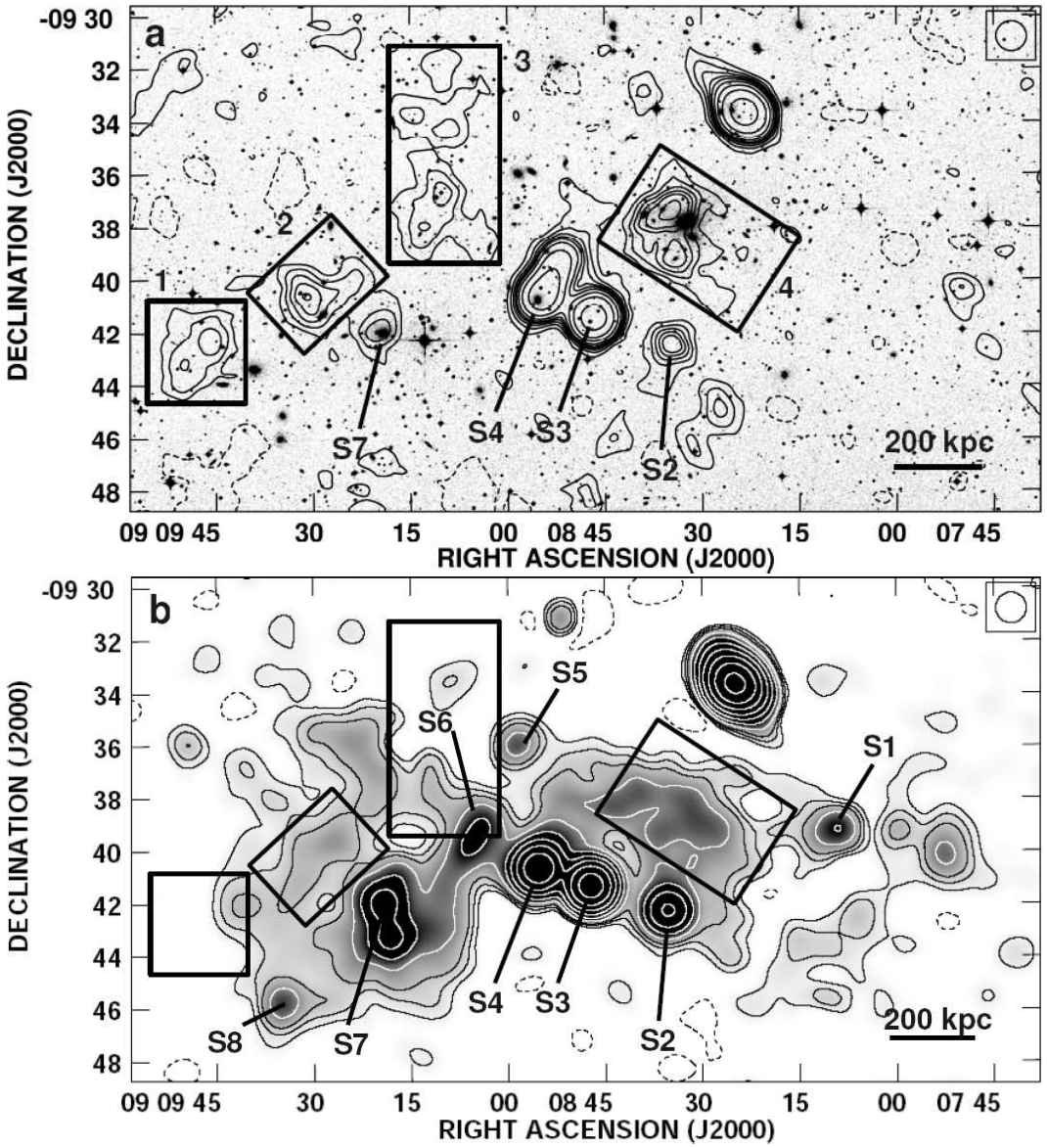

FIGURE 3.3: A754: (a) Shown in grey-scale is the POSS2 R-band image with the contours at 150 MHz (GMRT) overlaid. (b) Image at 1363 MHz is shown in greyscale and contours(courtesy G. Giovannini). The blobs of diffuse emission detected at 150 MHz are marked by rectangles and the discrete sources are indicated by labels in each of (a) and (b). Contour levels: (a) 150 MHz: -16.5, 16.5, 33, 49.5, 66, 82.5, 110, 165, 220, 330 mJy beam^{-1}; (b) 1363 MHz (VLA):-0.39,0.39, 0.78, 1.17, 1.56, 1.99, 2.8, 3.9, 7.8, 13 mJy beam^{-1}. The convolving beam shown at the top right corner is $70'' \times 70''$. The rms in the 150 MHz image is 5.5 mJy beam^{-1} and that in the 1363 MHz image is 0.13 mJy beam^{-1}.

Figs. 3.4 a and b, the images at 330 and 74 MHz (Kassim et al 2001) of the same region, respectively, are shown.

We use labels for discrete sources in the A754 field as used in Fig. 3 of BA03. For estimating the flux densities of discrete sources we have made use of images with resolutions (FWHM) of $50''$ and $10''$ at 1363 and 330 MHz respectively. The source S6 in Fig. 3.3 b is not detected at 150 MHz. It has flux densities of 33.0 and 7.0 mJy at 330 and 1363 MHz respectively which imply a spectral index of 1.0 ($S \propto \nu^{-\alpha}$). The non-detection of S6 above the 3σ level of 16.5 mJy at 150 MHz indicates that the spectrum has turned over. The non-detection of S5 (2.5 mJy at 1363 MHz) at 330 and 150 MHz is consistent with a spectral index of 0.8. Flux density of S1 at 1363 MHz is 3.6 mJy and the non-detection at 330 and 150 MHz implies a spectrum flatter than 0.8.

We have detected 4 diffuse features (blobs) at 150 MHz. These are marked by rectangles numbered 1, 2, 3 and 4 in Fig. 3.3a. Same rectangles are marked on the images at 1363 (Fig. 3.3 b), 330 and 74 MHz (Figs. 3.4 a and b) for comparison. The diffuse blobs 2, 3 and 4 are present in both Figs. 3.3a and b. Blob 1 is a new feature detected at 150 MHz. It does not show any obvious association with any galaxy detected in that region in optical band. It is not detected in the high resolution images and thus is a diffuse feature. The non-detection at 330 and 1363 MHz of blob 1 implies spectral index steeper than 2.0. The largest extent of this blob seen at 150 MHz is $\sim$ 200 kpc.

In the 74 MHz image by Kassim et al (2001), a feature which they called the 'west relic' was detected at the position RA=09h07m25s DEC=-09d36m52s (J2000)(outside of Fig. 3.4 b). This feature is not detected in any of the 150, 330 and 1363 MHz images. If the 'west relic' is real then the non-detection at 150 MHz implies a spectral index steeper than 1.8 between 74 and 150 MHz .

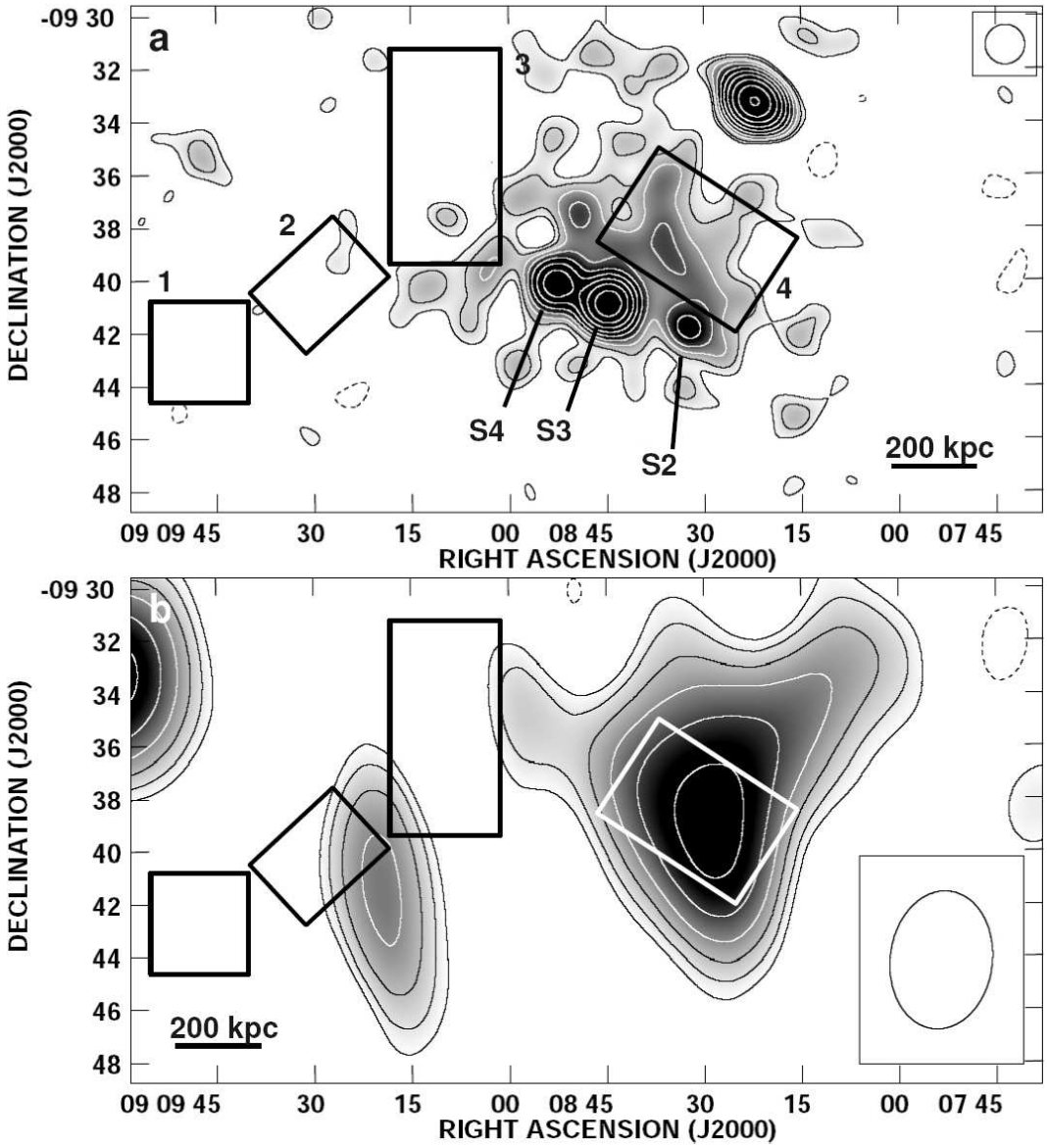

FIGURE 3.4: In (a) and (b) are 330 and 74 MHz images of A754, respectively, in greyscale and in contours(courtesy Kassim N.). Contour levels are at: (a) 16 mJy beam^{-1} × (-1, 1, 1.4, 2, 2.8, 4, 5.7, 8, 11.3, 16, 22.6, 32) and (b) 0.4 Jy beam^{-1} × (-1, 1, 1.4, 2, 2.8, 4, 5.7, 8, 11.3). Beam sizes are $90'' \times 90''$ and $316'' \times 233''$(P. A.= -7°) in (a) and (b) respectively.

3.5.2 Integrated Spectra of the Diffuse Components

The details of the flux densities of each blob of diffuse emission marked by rectangles in Figs. 3.3 and 3.4 are given in Table 3.2. The integrated spectra of each of the blobs 1, 2, 3 and 4 with 3σ error bars are plotted in Fig. 3.5. The flux densities of the blobs at each of the frequencies were estimated using rectangles of the same dimension as shown in Fig. 3.3a. The 1σ error on the total flux density at 150

TABLE 3.2: Flux densities of diffuse radio emission in A754

	Integrated Flux density(mJy)			α_{1363}^{150}	Extent
	(150 MHz)	(330 MHz)	(1363 MHz)		(kpc^2)
Blob 1	174	<28	<2.0	2.0	240× 200
Blob 2	188	<38	6.5	1.5	260× 160
Blob 3	340	<130	5.0	1.9	280× 540
Blob 4	540	230	23.0	1.4	350× 400

and 330 MHz is 20% and at 1363 MHz is 10%. In the case where the emission was not detected, the total flux density recovered in the corresponding box is reported as an estimate of upper limit. These upperlimits are plotted for blobs 1, 2 and 3 at 330 MHz and for blob 1 at 1.4 GHz. In the case of blob 3, the discrete source S6 contributed 4.8 mJy to the box shown. This value has been subtracted from the total flux density in box 3 to get the estimate of the flux density of blob 3.

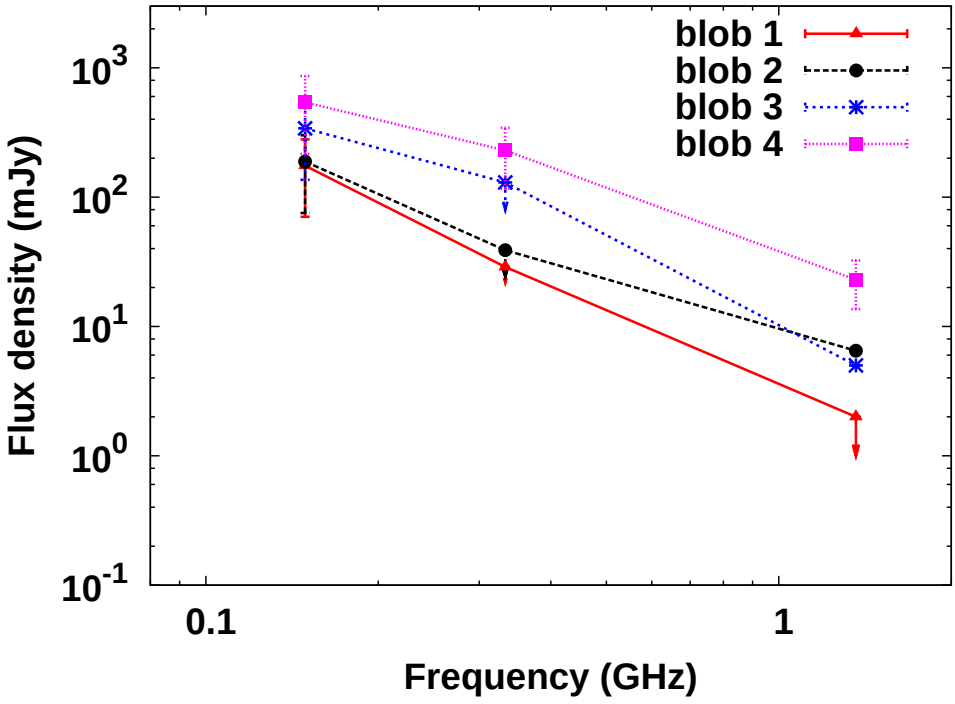

FIGURE 3.5: Integrated spectra of blobs 1, 2, 3 and 4. For blob 1 upperlimits at 330 and 1363 MHz are plotted; for blobs 2 and 3 upperlimits at 330 MHz are plotted.

3.5.3 Comparison with X-ray Maps

The locations of the diffuse radio emission are marked by boxes on the X-ray image (*XMM-Newton*, 0.8-2 keV, Henry et al (2004)) of A754 (Fig. 3.6). The locations of optical subclusters (ZZ95) are marked by star symbols. The proposed direction of merger of 2 sub-clusters of galaxies in A754 is along the line joining the two optical clumps (ZZ95). The peak of the X-ray emission is elongated perpendicular to the proposed direction of merger and so is blob 4 emission but ~ 700 kpc from the X-ray peak. There is no clear indication of a shock in the X-ray images of the region where the blobs are located. The blob 4 is cospatial with the western clump of optical galaxies. Based on the comparison of temperature map and radio image of A754, Govoni et al (2004) show a clear anti-correlation between the location of the diffuse radio sources and the regions of hottest X-ray emitting gas in A754.

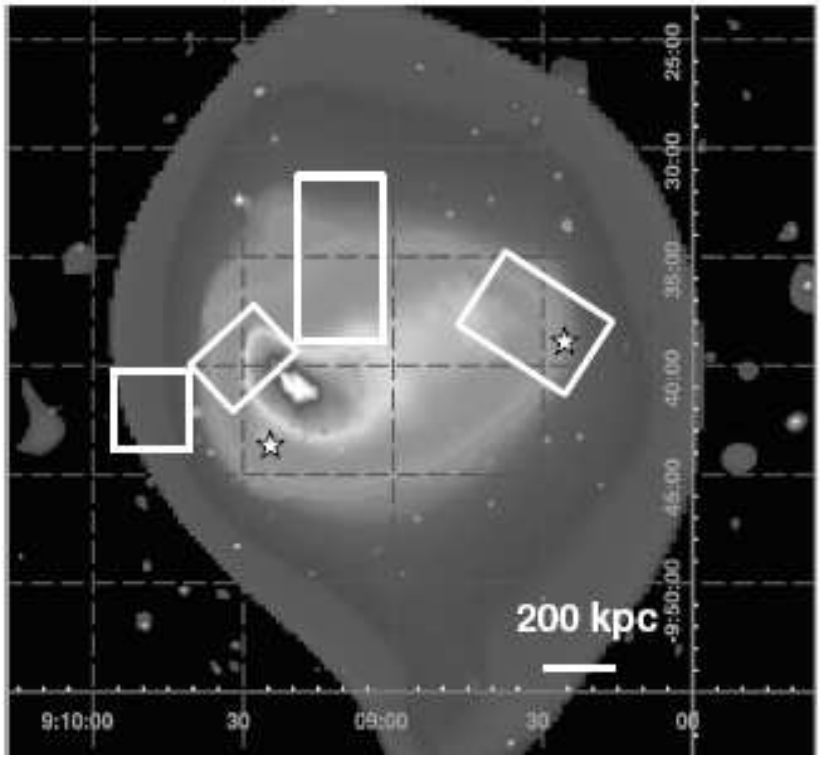

FIGURE 3.6: X-ray image in the band 0.8-2 keV from *XMM-Newton* (Henry et al 2004). Positions of optical clumps of galaxies (ZZ95) are marked by star symbols. The locations of the diffuse radio emissions blobs 1, 2, 3 and 4 are marked by rectangles.

3.5.4 Blob 4: The Relic

The blob 4 in Fig. 3.3a is consistent with the "halo" marked in the Fig.1 of Fusco-Femiano et al (2003). However, we shall refer to the blob 4 as a 'relic' due to its elongated morphology and the location away from the peak of the X-ray emission. A spectral index of 1.4 ± 0.2 was estimated using a linear fit to the spectrum between frequencies 150-1363 MHz. The extent of the relic projected in the plane of the sky is $\sim 350 \times 400$ kpc^2. The volume of the relic, estimated assuming a cylindrical geometry with the smaller side of the box as the diameter, is ~ 0.04 Mpc^3. The equipartition magnetic field of 0.7μG was computed using standard formulae (Pacholczyk 1970), integrating the radio emission between 10 MHz and 10 GHz, with a radio spectral index $\alpha = 1.4$, and assuming equal energy density in protons and electrons, and a volume filling factor of 1.

3.6 Adiabatic Compression Model

The diffuse radio emission in A754 is complex. It is possible that the diffuse blobs of emission are results of different phenomena in the cluster such as shocks or turbulence induced by the ongoing mergers. The morphology, the orientation with respect to the proposed merger axis and the location of the 'relic' described in Sec. 3.5.4 seems to suggest a connection with the ongoing merger in the cluster. Adiabatic compression of cocoons of radio galaxies by shocks is one of the models proposed to explain steep spectrum relic sources in clusters of galaxies (EG01) (Sec. 1.4.2). We have tried to understand the 'relic' emission in A754 in the context of this model.

Radio galaxies deposit relativistic plasma in the ICM through jets. After the jets turn off, apart from the PdV work done while expanding in the ICM, the relativistic plasma in the radio lobes loses energy by synchrotron and inverse Compton cooling on timescales of $\sim 10^8$ yr. From numerical simulations and observations it is known that cluster mergers drive shocks in the ICM (eg. Miniati et al 2000;

Markevitch et al 2002). The lobes of non-thermal plasma do not experience the shocks due to high sound velocities in them unlike the thermal plasma. Such fossil lobes would get compressed adiabatically by shock waves in the ICM and emit detectable radio emission. This idea of reviving fossil radio lobes by adiabatic compression is discussed in EG01 in detail. The salient features of this model are described here.

3.6.1 Formalism of EG01

The aim is to find the evolution of the distribution of energy among relativistic electrons in a given volume and a magnetic field which also change with time due to expansion and compression. This is achieved using the formalism that is described below.

Consider relativistic plasma in a radio lobe of a radio galaxy. The rate of change of momentum (p), of a relativistic electron is proportional to the magnetic energy density, u_B (synchrotron losses), the energy density of the cosmic microwave background radiation, u_C (inverse Compton losses) and the adiabatic gain or loss due to the change in the volume (V) of the radio plasma:

$$-\frac{dp}{dt} = a_0(u_B + u_C)p^2 + \frac{1}{3}\frac{1}{V}\frac{dV}{dt}p \tag{3.1}$$

where $a_0 = \frac{4}{3}\frac{\sigma_T}{(m_e c)}$. Due to very low particle densities in the plasma, Bremsstrahlung and Coulomb losses have been neglected. Sufficient pitch angle scattering of electrons is assumed so that the pitch angle distribution is isotropic (Jaffe & Perola 1973; EG01). Introduction of a compression ratio and a change of variable yields a solution for p. A ratio of the initial volume of the radio cocoon (V_0) and the volume at time t ($V(t)$) is called the compression ratio, $C(t) = V_0/V(t)$. Further, the change in the volume is approximated to be a power law in time, $V(t) = V_0(t/t_0)^b$. The photon energy density of the cosmic microwave background does not change over the timescales such as $\sim 10^8$ yr and thus u_C does not change. However, u_B, the magnetic energy density will change during adiabatic

expansion (or compression). Adiabatic expansion of a spherical volume (radius r_o to r) of ultra-relativistic particles of energy E_o leads to the scaling of energy as $E = E_o(r_o/r) = E_o(V/V_o)^{-1/3}$ (eqn. 11.30, Longair 1981) and thus of energy density as $E/V = (E_o/V_o)(V/V_o)^{-4/3}$. Assuming an isotropic adiabatic expansion of the magnetized plasma, the magnetic field energy density (u_B) scales as $u_B = u_{B,0}(V(t)/V_0)^{-4/3}$. With these assumptions, the solution of Eq. 3.1 for p can be obtained in terms of a characteristic momentum $p_*(t)$ which can be given in the form:

$$p_*(t) = \frac{C^{\frac{1}{3}}}{a_0 t(\frac{C^{5/3}-C^{1/b}}{1-5b/3}u_{B0} + \frac{C^{1/3}-C^{1/b}}{1-b/3}u_C)} \tag{3.2}$$

where $C = C(t)$. The characteristic momentum p_* denotes where a sharp cut-off would be expected due to energy losses by synchrotron and IC mechanisms. If the original electron distribution $f_0(p_0)$ at time t_0 and extends to infinity, at a later time t a sharp cutoff would be found at p_* in the distribution $f(p,t)$. The distribution of electrons at time t, $f(p,t)$ is obtained in the following manner.

The electron density per unit volume and momentum, $f(p,t)dpdV$ for $p < p_*(t)$ is given by,

$$f(p,t) = f_0(p_0(p,t))\frac{\partial p_0(p,t)}{\partial p}C(t), \tag{3.3}$$

where,

$$p_0(p,t) = \frac{pC(t)^{-\frac{1}{3}}}{1 - p/p_*(t)}. \tag{3.4}$$

The Eq. 3.4 is obtained using the solution of Eq. 3.1.

The case of interest is when the initial distribution of electrons is a power law,

$$f_0(p_0) = \tilde{f}_0 p^{-\alpha_e}. \tag{3.5}$$

Using Eq. 3.4 and 3.5, for $p_{min0} < p_0 < p_{max0}$, the resulting spectrum is,

$$f(p,t) = \tilde{f}_0 C(t)^{\frac{\alpha_e+2}{3}} p^{-\alpha_e}(1 - p/p_*(t))^{(\alpha_e-2)} \tag{3.6}$$

for $p_{min}(t) = p(p_{min0}, t) < p < p_{max}(t) = p(p_{max0}, t)$.

The situation where the plasma undergoes cooling and expansion is of interest. EG01 have formulated a way to find out the distribution of electrons at distinct intervals of time which are of interest. The final momentum and compression factor after n phases of expansion and cooling are given by,

$$p_n(p_0) = \frac{p_0}{C_{0n}^{-\frac{1}{3}} + p_0/p_{*0n}}, \tag{3.7}$$

where

$$C_{0n} = \prod_{i=1}^{n} C_{i-1i} = \prod_{i=1}^{n} \frac{V_i - 1}{V_i} = \frac{V_0}{V_n} \tag{3.8}$$

and the maximal final momentum is given by,

$$\frac{1}{p_{*0n})} = \sum_{i=1}^{n} \frac{C_{0i-1}^{\frac{1}{3}}}{p_{*i-1i}}. \tag{3.9}$$

In the formulation of EG01, a phase i where expansion or compression is given by the index b_i, can be described if two of the three parameters are given:τ_i, the timescale for expansion, C_{i-1i}, the compression ratio during the phase i, and Δt_i, the duration of the phase. These quantities are related via,

$$C_{i-1i} = (1 - \Delta t_i/\tau_i)^{-b_i}. \tag{3.10}$$

The characteristic momentum,

$$p_{*i-1i} = \frac{C^{\frac{1}{3}}}{a_0 t_i \left(\frac{C^{5/3} - C^{1/b}}{1-5b/3} u_{Bi} + \frac{C^{1/3} - C^{1/b}}{1-b/3} u_C \right)}, \tag{3.11}$$

with $C = C_{i-1i}$ and $t_i = \tau_i + \Delta t_i$. The magnetic energy density in the i^{th} phase is the one at the end of the phase $i-1$,

$$u_{Bi-1} = u_{B0} C_{0i-1}^{4/3}. \tag{3.12}$$

The resulting electron distribution from an initial power law distribution, at the end of the i^{th} phase is,

$$f_i(p) = \tilde{f}_0 C_{0i}^{\frac{\alpha_e+2}{3}} p^{-\alpha_e}(1 - p/p_{*0i})^{\alpha_e - 2}, \tag{3.13}$$

for $p_{mini} = p_i(p_{min0}) < p < p_i(p_{max0})$ and $f_i(p) = 0$ otherwise. The synchrotron emission is given by,

$$L_{\nu i} = c_3 B_i V_i \int_{p_{mini}}^{p_{maxi}} dp f_i(p) \tilde{F}(\nu/\nu_i(p)), \tag{3.14}$$

where $c_3 = \sqrt{3}e^3/(4\pi m_e c^2)$ and the characteristic frequency is $\nu_i(p) = 3eB_i p^2/(4\pi m_e c)$. The dimensionless spectral emissivity of a mono-energetic isotropic electron distribution in isotropically oriented magnetic fields $\tilde{F}(x)$ can be approximated by (Ensslin et al 1999),

$$\tilde{F}(x) \approx \frac{2^{2/3}(\pi/3)^{3/2}}{\Gamma(11/6)} x^{1/3} exp\left(-\frac{11}{8}x^{7/8}\right). \tag{3.15}$$

In this formulation the magnetic field is assumed to be isotropic. EG01 mention that if the magnetic field is not isotropic, this formulation can only calculate the luminosity, not the flux density.

3.6.1.1 The Phases

The evolution of the radio plasma is divided into five discrete phases - (0) injection, (1) expansion, (2) lurking, (3) flashing and (4) fading. These phases are described below and are represented schematically in Fig. 3.7.

Phase 0 (Injection): The radio galaxy is active. A large expanding volume is filled with relativistic plasma by the jets. The typical timescale over which this phase lasts is ~ 0.015 Gyr (EG01; Alexander & Leahy 1987). This expansion is supersonic with respect to the external medium with an index $b = 9/5$, with the assumption that there is no gas density gradient in the vicinity of the radio galaxy (EG01; Kaiser & Alexander 1997).

Phase 1 (Expansion): The jets of the radio galaxy are turned off; the radio cocoon expands in the surrounding medium due to higher internal pressure compared to the surrounding ICM. The expansion is considered Sedov-like ($b = 6/5$) throughout this phase for simplicity (EG01).

Phase 2 (Lurking): The radio cocoon reaches pressure equilibrium with the ICM and thus the volume of the plasma remains constant. The energy losses due to radiation continue to steepen the spectrum.

Phase 3 (Flashing): If a shock compresses a lurking radio cocoon, there is enhanced radio emission due to adiabatic compression of the magnetic field. The spectrum flattens.

Phase 4 (Fading): The compressed cocoon continues to lose energy by synchrotron and inverse Compton losses and fades.
Each phase is characterised by its duration (Δt), the timescale of expansion (τ) and an index (b) that determines the rate of expansion/compression of the radio cocoon. The spectrum is obtained using the formulation described in Sec. 3.6.1.

3.6.1.2 The Scenarios

Further, the five phases are discussed under three scenarios by EG01.
Scenario A: Cocoon at cluster centre- The external pressure provided by the ICM is large and thus the pressure inside the radio cocoon is considered to be only twice the external pressure. The lurking phase lasts only for 0.1 Gyr; the cocoon will not be able to emit detectable radio emission after compression if it is older.
Scenario B: Cocoon at cluster periphery- The freshly injected plasma is over pressured compared to the surrounding medium by a factor $\sim$ 100. Pressure equilibrium with the surrounding medium is achieved faster. The plasma can be revived by shock compression even after 1 Gyr.
Scenario C: Cocoon near an active radio galaxy(smoking gun)- A radio galaxy which is possibly the source of the relativistic electrons is visible near the relic. This case is illustrated by the example of the relic in Coma by EG01.

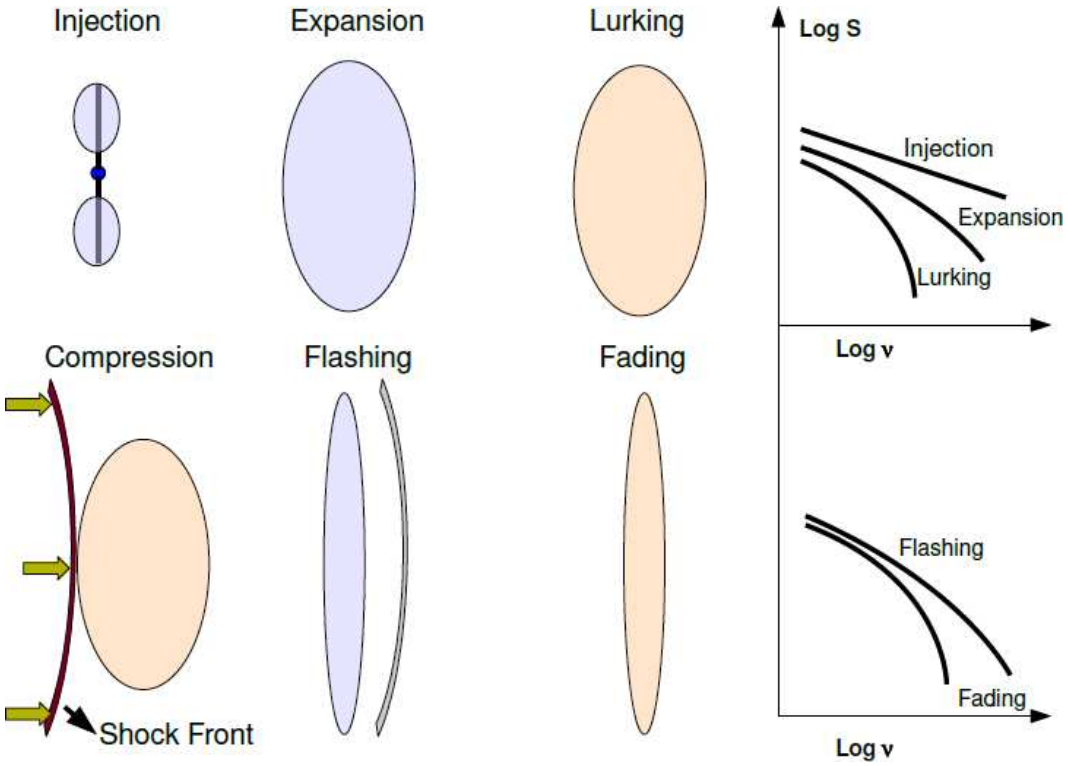

FIGURE 3.7: A schematic representation of the various phases in the adiabatic compression model. On the right, the spectra obtained in each of the phases are sketched. The injection phase is shown by an active radio galaxy. The jets turn off and the lobes expand forming a cocoon. The cocoon lurks while it loses energy. A shock front in the ICM hits the cocoon resulting in a compression. During compression of the cocoon, the spectrum flattens (flashing phase) and then steepens in the fading phase.

3.6.2 Coding of the Model

The code for the EG01 formulation was written in Fortran 77. The spectra for the scenarios A, B and C for the parameters given in Table 1. of EG01 were reproduced. This served as a check for the code written. The normalization of the luminosities is arbitrary since the parameter $\tilde{f}_0$, of the initial distribution is not known.

3.6.3 Application to the Relic in A754

In A754 the relic (blob 4) has been detected at all the 3 frequencies. The EG01 model has been used to obtain a spectrum which fits the observed spectrum of the relic best. Scenario A was considered best suited for A754 since the relic is

located in a region where the X-ray emission has been detected (Henry et al 2004). The relic in A754 is only weakly polarized ($< 9\%$ at 1.4 GHz, BA03). Thus, using the redshift of A754, the flux density was calculated from the luminosity (Eq. 3.14). The steps carried out to arrive at the model spectra from the adiabatic compression model for the relic are described below.

1. The radio plasma was assumed to be in i^{th} phase and the estimated magnetic field (B) and volume (V) of the relic were used.

2. Using compression ratio (C) for the i^{th} phase, back calculation was carried out to find the B and V for $(i-1)^{th}$ phase successively till Phase 0.

3. The spectra were obtained for each of the phases.

4. It was checked whether the model spectrum in the i^{th} phase, in which the relic was assumed to be in, was a good fit to the integrated spectrum of the relic.

5. If the spectrum was a bad fit to the observed spectrum, the plasma was assumed to be in another phase and the same steps were carried out.

In a case where the relic was assumed to be in Phase 1, the corresponding model spectrum was flatter than could fit the observed data. In another case where the relic was assumed to be in Phase 2, the spectrum was steeper. A phase intermediate to 1 and 2 was tried and the best fit to the observed spectrum was obtained. This intermediate phase is referred to as "Phase 1.5". The model spectra are shown in Fig. 3.8. These spectra were constructed using the parameters listed in Table 3.3. The observed values of the flux density of blob 4 at 150, 330 and 1363 MHz with the 3σ error bars are plotted along with the model spectra. The initial energy distribution of the relativistic electrons was assumed to be a power law with a spectral index of 2.6 ($f_0 = \tilde{f}_0 p^{-\alpha_e}; \alpha_e = 2.6$). The flux density at 150 MHz was used to normalize the model spectrum.

A good fit was obtained by considering the relic to be in flashing phase ("Phase 3") too. The volume in the injection phase (Phase 0) required in this case to produce the observed size of the relic after compression by shock is ~ 0.15 Mpc^3. This implies that a volume of ~ 0.15Mpc^3 must have been filled with radio plasma by cluster radio galaxies forming a gigantic cocoon. Considering the typical size of a radio galaxy to be 100 kpc (middle value in Fig. 9 of Blundell et al 1999) and

TABLE 3.3: Adiabatic compression model fit parameters

	Δt (Gyr)	τ (Gyr)	b	V (Mpc^3)	B (μG)
Phase 0	0	0.015	1.8	0.02	1.0
Phase 1	0.0054	0.01	1.2	0.04	0.7
Phase 1.5	0.09	∞	0	0.04	0.7
Phase 2	0.1	∞	0	0.04	0.7
Phase 3	0.069	-0.11	2.0	0.006	2.42
Phase 4	0.02	∞	0	0.006	2.42

assuming it to fill a sphere of that radius with relativistic plasma, at least ~ 35 such sources are required to be active within a period of $\sim$ 1Gyr, to fill a giant cocoon of volume 0.15 Mpc^3. Such a situation is improbable in any typical galaxy cluster.

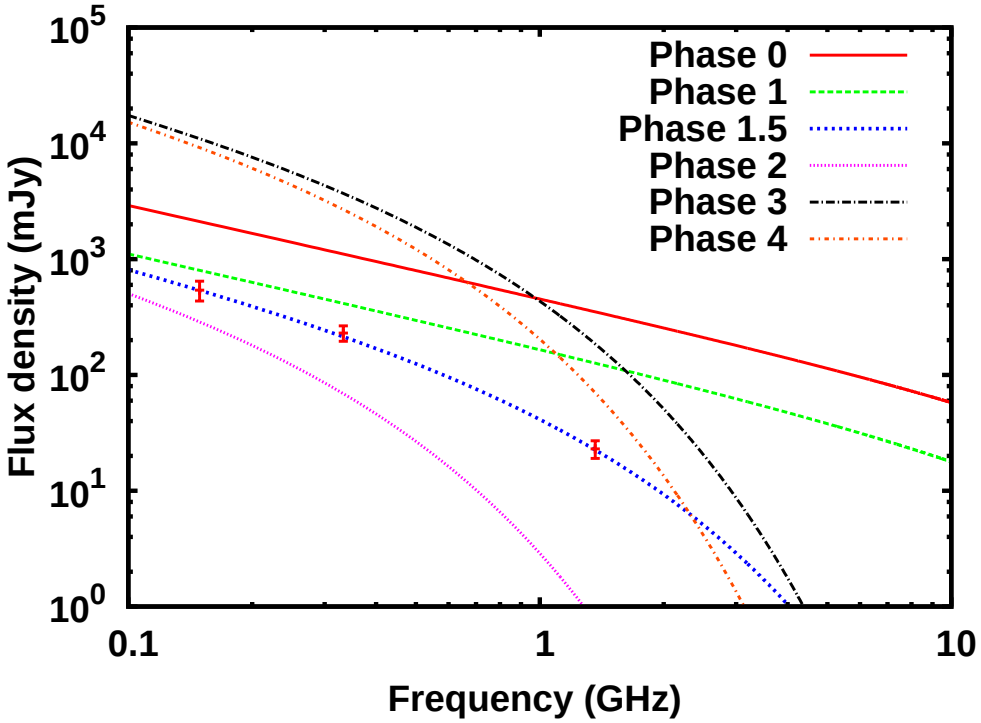

FIGURE 3.8: Model spectra obtained using the adiabatic compression model (See Table 3.3 for the parameters). The model spectrum in phase 1.5 fits the observed spectrum (dots) of blob 4 best.

3.7 Discussion

In imaging extended emission at radio frequencies crucial roles are played by the uv-coverage, the sensitivity and the field of view. These vary with the observing frequency and the instrument used. Further, the spectra of halos and relics are not the same over the extent of the source; there can be isolated regions of steep and flat spectral indices. Due to this interplay between the different aspects of the observational limitations and the intrinsic properties of the diffuse emission, multi-frequency observations of halos and relics are necessary to obtain maximum information and to make further inferences. Radio halos and relics are extended and steep spectrum sources which makes the role of low frequency observations crucial. Statistical studies of the radio halos predict that at low frequencies such as 150 MHz about ten times more number of giant radio halos having flux densitites above a few mJy will be detected as compared to 1.4 GHz (Cassano et al 2006). Recently 235 MHz observations with the GMRT have resulted in the detection of a steep spectrum radio halo in the cluster A521 (Brunetti et al 2008). Using the WSRT at 150 MHz two steep spectrum relic sources about 2 Mpc away from the cluster centre of A2255 (Pizzo et al 2008) have been discovered. Sensitive low frequency observations of galaxy clusters have three fold advantages: imaging of large regions around cluster centres due to larger primary beams, sensitivity to ultra-steep spectrum components and better short spacing coverage as compared to high frequency observations with similar telescope configurations. The observations of A754 at 150 MHz using the GMRT have resulted in the detection of one new diffuse feature (blob 1) which has spectral index steeper than 2. The blob 1 has an extent of $\sim$ 200 kpc at 150 MHz. This diffuse blob represents the population of steep spectrum features which might exist in many other clusters and are waiting to be discovered using sensitive low frequency observations.

In the case of A754, blob 1 has been detected only at 150 MHz whereas blob 4 is detected at all of 150, 330 and 1363 MHz, but better at 1363 MHz. The spectra of blobs 1, 2 and 3 are steeper than that of blob 4. Considering the 'relic' like features of blob 4 (Sec. 3.5.4), the adiabatic compression model proposed to explain the

relics was tested. The framework of adiabatic compression model (EG01) was coded and spectra were obtained to compare with the observed spectrum of the relic (blob 4). It was found that, the relic (blob 4) can be considered as a cocoon of a radio galaxy lurking for $\sim 9 \times 10^7$ yr in the ICM. No shock compression was required to produce the spectrum of the relic. The consideration of blob 4 as a compressed radio cocoon (Flashing phase) led to an unrealistic situation of the cluster having a gigantic (~ 0.15 Mpc^3) radio cocoon in the past, which appears unlikely. Thus, merger shocks need not be invoked to explain the observed properties of the relic. Since only upper limits at 330 and 1363 MHz were available for blobs 1, 2 and 3, model fitting was not carried out for those. The flux density at 150 MHz and the upperlimits at 330 and 1363 MHz imply spectral indices steeper than 1.5 for blobs 1, 2 and 3. Based on the result for blob 4 from the adiabatic compression model, these blobs of diffuse emission are likely to be radio cocoons lurking in the ICM for more than 10^8yr.

In a few clusters that have relics, merger shocks have been considered to be responsible for accelerating electrons (eg. A3376, Bagchi et al 2006). According to the numerical model of Roettiger et al (1998) for A754, a large subcluster has crossed the main cluster from east to west. The 4 diffuse blobs in A754 lie along the east-west axis which is approximately the proposed axis of merger (ZZ95). The proposed location of the eastern shock wave is coincident with the X-ray peak and is close to blobs 1 and 2. The steep spectral indices of blobs 1 and 2 could be explained in the Fermi I acceleration scenario by a low Mach number shock (Mach number < 2 for a spectral index steeper than 2.0; Blandford & Eichler 1987). The western shock has been proposed to be at a location $\approx 1.8 h_{75}^{-1}$ Mpc from the X-ray peak (Roettiger et al 1998; KA01). The blob 4 which is in the western region is only 0.7 Mpc from the X-ray peak and is not coincident with the proposed location of the shock. According to the numerical model the shocks crossed the cluster more than 0.3 Gyr ago which is longer than the radiative lifetime of the electrons observed at 150 MHz. In A754, no other relics have been detected in the primary beam at 150 MHz. Sensitive polarization study of the diffuse emission has not been carried out to find other signatures of shocks such as alignment of

magnetic field in the plane of the shock. Upperlimits on polarized flux density of 9% and 15% have been obtained by BA03 on the western and eastern diffuse emission respectively in A754.

Mergers can create turbulence in the ICM which could then accelerate particles. It has been proposed that Fermi acceleration powered by turbulence in the ICM can accelerate particles to relativistic energies (Brunetti et al 2008 and references therein) if the turbulence lasts for more than 10^8yr. Particles in the ICM, through resonant scattering off the turbulent waves, can be stochastically accelerated to relativistic energies (Melrose 1980). The relation between mergers and turbulent acceleration of particles is complex and the details are not clear. The steep spectrum with a cutoff at high frequencies is a signature of turbulent reacceleration (Kuo et al 2003; Brunetti et al 2004; Cassano et al 2005). A halo has been detected in A521 at low frequencies such as 235, 330 and 610 MHz (Brunetti et al 2008) having spectral index of ~ 2. A high frequency spectral cutoff is suspected by the authors for this halo making it undetectable at 1.4 GHz with the reported sensitivity of their observation. Turbulent reacceleration model has been invoked to explain the low frequency halo. It is likely that many such diffuse features having cutoff at high frequencies could be lurking in clusters but have not been detected since no low frequency observations have been carried out. The non-detection of blob 1 at 330 and 1363 MHz indicates cutoff in its spectrum. This implies the possibility of turbulent reacceleration. The case of blob 4, not requiring shock to explain the radio emission, is also consistent with the picture of turbulent reacceleration.

Another possibility is that the shocks accelerated the protons in the ICM which produced secondary electrons and positrons by hadronic collisions. These secondary particles then produced the observed radio-halo emission. In this case the radio emission can last long after the passage of shock. This scenario will be tested with the detection of gamma ray flux expected from the decay of neutral pions after the p-p collisions (Ensslin et al 1997; Colafrancesco & Blasi 1998; Blasi 1998; Dolag & Ensslin 2000).

3.8 Summary

We have presented a GMRT 150 MHz image of the A754 region. We detected 4 blobs of diffuse emission at 150 MHz with a resolution of $70'' \times 70''$. We made high resolution images using the archival data at 330 (GMRT) and 1363 MHz (VLA) to estimate flux densities of discrete sources and used the published images of A754 at 74, 330 and 1363 MHz (VLA) to compare the diffuse features. The 'blob 1' is a new diffuse feature with linear size $\sim$ 200 kpc detected at 150 MHz. The upperlimits on the flux density of 'blob 1' at 330 and 1363 MHz indicate a spectral index steeper than 2.0. The detection of such a feature is an evidence of the crucial role that low frequency observations can play in the studies of diffuse emission from clusters of galaxies.

The diffuse blob 4 lies along the axis of merger in A754 and on the far side of the X-ray peak; thus we referred to it as a relic. The adiabatic compression model that has been proposed to explain the relics was coded and applied to this relic. Within the framework of this model, we found that the blob 4 can be explained as an ageing cocoon of an old radio galaxy in the cluster. The spectra of blobs 1, 2 and 3 of diffuse emission are steeper and thus can be considered as radio cocoons older than the relic. Cluster wide turbulence injected by cluster- cluster mergers are one of the favoured mechanisms for the generation of diffuse radio emission in clusters (Brunetti 2004 and references therein). Turbulence has also been considered to produce steep spectrum radio halos such as the one in A521 (Brunetti et al 2008). Considering the detection of a steep spectrum blob (blob 1), the inconsistency of the spectrum of blob 4 with shock compression scenario and the complex merger in A754, the role of turbulence is likely to be important.

Chapter 4

Radio Relics in Clusters of Galaxies

Kale. R. & Dwarakanath, K. S. in prep.

4.1 Introduction

Radio relics in clusters of galaxies are a class of diffuse radio sources that show variety in their morphologies, spectra and locations in the cluster relative to the cluster centres. Typically relics have steep spectra ($\alpha < -1.2$, $S \propto \nu^{\alpha}$) and elongated filamentary morphologies. The relics are modelled as remnants of radio galaxies or as sites of acceleration at merger/accretion shock fronts (Sec 1.4). Most of the studies of relics have been carried out at frequencies close to 1.4 GHz. So the nature of the relics at low frequencies remains unknown. It has been shown in previous chapters that low frequency observations of radio halos yield new information about their morphologies and spectra. Populations of relativistic electrons having ultra-steep spectrum can be discovered at low frequencies. In this chapter we present our low frequency studies of radio relics.

The main aims of this study are: (a) to find if there are new steep spectrum components in the relics; (b) to construct the integrated spectra of the relics at

low frequencies; (c) to test whether the adiabatic compression model can provide best fits to the integrated spectra of the relics.

This chapter is organized as follows: Sec. 4.1.1 provides basic information about the clusters and the relics chosen for study. The radio observations are presented in Sec 4.2. Results for each cluster are presented and discussed separately under Secs. 4.3-4.8 followed by a summary of the chapter in Sec. 4.9.
We adopt a cosmology with $H_0 = 73$ km s^{-1}Mpc^{-1}, $\Omega_{matter} = 0.27$ and $\Omega_{vacuum} = 0.73$.

4.1.1 The clusters

We have undertaken a study of 3 radio relics which reside in the clusters A4038, A1664 and A786. The basic properties of these clusters are given in Table 4.1. The redshifts of A4038 and A786 are from Struble & Rood (1999) and the redshift for A1664 is from Pimbblet et al (2006). The variety in the morphologies and the locations of these relics relative to cluster centres were the main criteria, apart from the suitability for low frequency observations with the GMRT, the VLA and the WSRT, in selecting these relics for observations and further study.
Abell 4038 (also known as Klemola 44): The relic in A4038 was discovered as an ultra-steep spectrum source in surveys by Slee & Reynolds (1984) and Slee et al (1994). Further observations were carried out at 1.4 GHz using the VLA by Slee & Roy (1998) (hereafter, SR98) and Slee et al (2001) (hereafter, SL01). Based on those observations, the extent of the relic was reported to be 56 kpc and a polarized intensity of 4% was detected. Spectral index (α) over a narrow range of frequencies around 1.4 GHz was estimated to be -3.1. No optical counterpart ($m_R \geq 23.0$) was found (SR98).
Abell 1664: This is a relic identified from the NVSS by Giovannini et al (1999). It is known for its circular morphology (Govoni et al 2001) unlike other relics which have irregular or elongated morphologies. The cluster A1664 has a cooling flow at the centre (Aleen et al 1995) but does show some distortions in the X-ray surface brightness indicating a recent minor merger (Govoni et al 2001). It has not

been imaged at any frequency other than 1400 MHz and thus the spectral index is unknown.

Abell 786: This relic was first identified and studied by Dewdney et al (1991) and Harris et al (1993). This relic is unique in its location. The cluster centre nearest to the relic is of A786 and is at a distance of $\sim$ 5Mpc. It is likely to be the site of a large scale cosmological shock (Ensslin et al 1998). This relic is also referred to as '0917+75' in literature.

TABLE 4.1: Properties of the Clusters

Cluster	R. A.[a]	Dec.[a]	R[b]	BM[c]	z	σ_V	log	LLS[d]
	hh mm ss	dd mm ss				km s^{-1}	($L_X$erg s^{-1})	(kpc)
A4038	23 47 43	-28 07 28	2	III	0.03	839	44.1	210
A1664	13 03 41	-24 13 06	2	-	0.128	900	44.8	927
A786	09 22 00	75 00 00	0	-	0.1241	-	44.1	1640

[a] Epoch = J2000

[b] R=Richness Class

[c] BM=Bautz-Morgan Classification

[d] LLS=Largest Linear Size of the relic

4.2 Radio Observations and Data Reduction

The GMRT and the WSRT were used to image the relics at frequencies < 1.4 GHz. A summary of the radio observations carried out is given in Table 4.2. The relics selected here have been observed earlier at 1.4 GHz (see Sec. 4.1.1). Archival data at 1.4 GHz from the VLA in the form of visibilities was used to make images of the relic in A786. In the cases of A1664 and A4038, images from the NVSS (1400 MHz) and VLSS (74 MHz) were used.

Reduction of all the data mentioned above was carried out using AIPS. Standard steps of data editing (flagging) and complex gain calibration were carried out. The data lost due to RFI varied between $5-35\%$ over the range of frequencies 1288 to

150 MHz at the GMRT. At 150, 240, 350 and 606 MHz polyhedron imaging was carried out to overcome the effects of non-coplanarity. The frequency channels were suitably averaged in every data set to reduce the size of the data set but avoid bandwidth smearing. The final set of visibilities was used for imaging. Self-calibration was carried out to obtain deeper images at all the frequencies.

TABLE 4.2: Summary of Observations

Source	Freq., BW (MHz)	Telescope, Date	Time (min)	Synthesized beam($''\times''$)	P.A. ($^\circ$)	rms mJy beam^{-1}
	74	VLA-A (VLSS)	-	80×80	0	100
A4038	150 , 6	GMRT, Sep.'07	40	25×25	0	4.0
	240 , 8	GMRT, Aug.'09	240	15×9	-11	1.0
	606 , 16	GMRT, Aug.'09	240	6×3	28	0.26
	1288 , 32	GMRT, Sep.'09	200	3×2	35	0.093
	1400	VLA-D (NVSS)	-	45×45	0	0.45
A1664	150 , 6	GMRT	210	53×45	4	7.0
	325 , 16	GMRT	120	39×30	40	1.0
	1400	VLA-D (NVSS)	-	45×45	0	0.3
A786	150 , 6	GMRT	210	67×52	22	10.0
	350 ,16	WSRT	544	52×51	7	0.8
	606 ,16	GMRT	240	64×64	0	2.3
	1400, 50	VLA-D	20	50×50	0	0.2

4.3 Results- I : Abell 4038

4.3.1 Discoveries of Extended Components at Low Frequencies

Images of A4038 using the GMRT at 1288, 606, 240 and 150 MHz are presented in Figs. 4.1a, b, c and d respectively. The synthesized beams and the rms noise levels in each of these images are reported in Table. 4.2. The elongated, filamentary, 'hook' shaped structure in Fig. 4.1 a is the relic studied by SR98 and SL01 using the VLA at 1.4 GHz. We have discovered a much more extended structure of the diffuse emission in A4038 in our images at 606, 240 and 150 MHz. In Fig. 4.1d, the

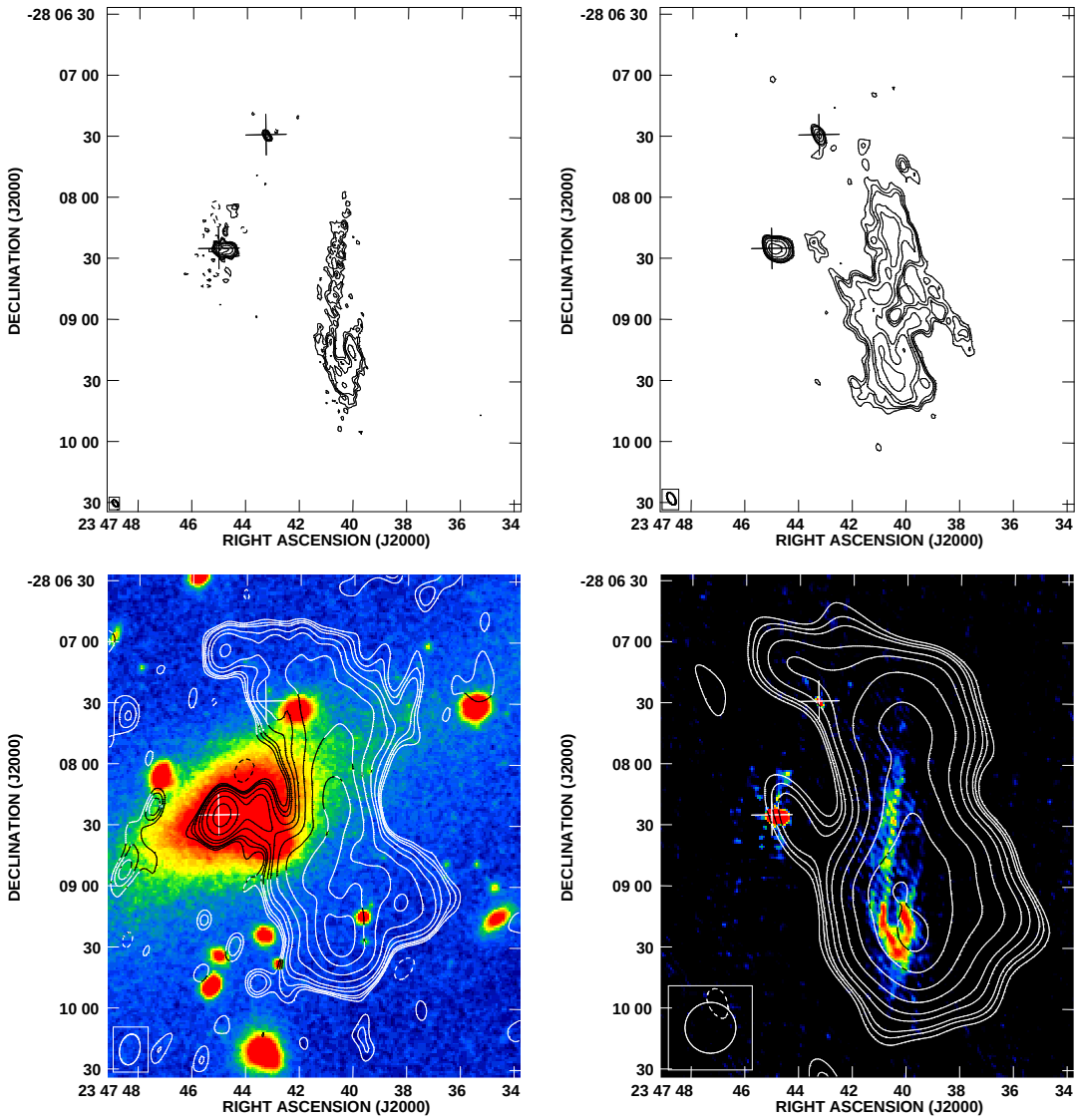

FIGURE 4.1: GMRT images of A4038 at: *Top left* (a) 1288 MHz, *Top right*(b) 606 MHz, *Bottom left* (c) 240 MHz and *Bottom right* (d) 150 MHz shown in contours. See Table 4.2 for the synthesized beams and rms values in each of the images. The contours are at (a) -0.3, 0.3, 0.4, 0.5, 0.8, 1.2, 2.4, 4.8, 9.6, 15.4 mJy beam^{-1}; (b) -0.75, 0.75, 1.0, 1.25, 2.0, 3.0, 6.0, 12.0, 24.0, 38.5 mJy beam^{-1}; (c) -2.7, 2.7, 3.6, 4.5, 7.2, 10.8, 21.6, 43.2, 86.4, 138.6 mJy beam^{-1}; (d) -15, 15, 20, 25, 40, 60, 120, 240, 480, 770 mJy beam^{-1}. The DSS R band image is shown in colour in (c). In (d), the 1288 MHz image in (a) is shown in colour.

1288 MHz image is shown in colour on the 150 MHz contours. The 'hook' shaped relic is but a small fraction of the extended source detected at low frequencies.

The crosses in Figs. 4.1a, b, c and d mark the positions of two discrete radio sources in A4038. The first cross from the top marks A4038_10, which is an unidentified

radio source presumed to be a background source unrelated to A4038. The second cross marks A4038_11, which is the radio source associated with the cD galaxy (see the DSS R band image in colour in Fig. 4.1 c) in A4038. The names A4038_10 and A4038_11 are according to SL01.

The morphology of the relic at low frequencies extends beyond the L-band relic in all directions, but much more in the north. The portion of the relic (Figs. 4.1c, d) north of A4038_10 has a peak flux density of 30.3 mJy beam^{-1} at 240 MHz and 97.0 mJy beam^{-1} at 150 MHz making it a source with spectral index, $\alpha_{150}^{240} \sim -2.5$. The non-detection of it at 1288 MHz implies that the spectral index $\alpha_{240}^{1288} < -2.7$. We refer to it as the 'North relic'.

The extent of the relic detected at 150 MHz is $3.8'$ along the N-S which is equal to a linear extent of 133 kpc and $2.3'$ in the E-W which is 80.5 kpc at the redshift of A4038.

4.3.1.1 A low surface brightness extension ?

An image at 240 MHz with a resolution $15'' \times 15''$ is presented in Fig. 4.2 a. Examination of the 240 MHz image indicated that some extended emission in the image could have been resolved out. Blobs of emission are seen scattered to the NW of the relic and to the east of the cD (A4038_11). We produced low resolution images at 240 MHz to confirm the presence of the suspected extended feature toward the NW. For comparison with the 150 MHz image and to detect the extended feature better, the 240 MHz image was convolved to a resolution of $25'' \times 25''$. The resulting image is presented in Fig. 4.2b overlaid on the DSS R band image in grey-scale. The 240 MHz image showing a larger field around the relic is presented in Fig. D.1. Only those features which have peak flux densities $\geq 5\sigma$ are considered significant and are discussed below.

An extension of the relic toward the NW is detected along with two patches of emission to the east of A4038_11. No obvious optical counterparts to the new sources are found. We refer to the newly detected extension toward north west

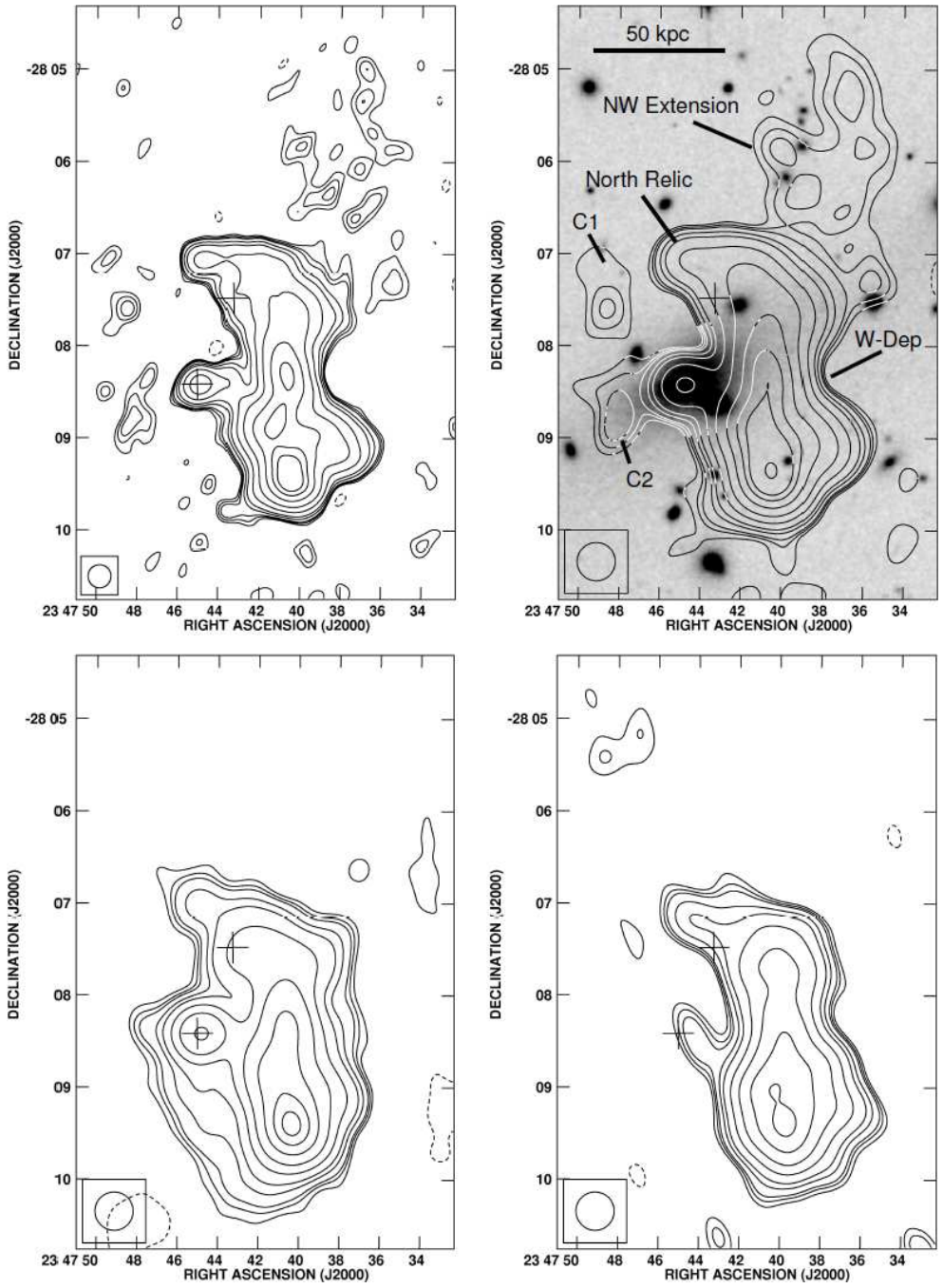

FIGURE 4.2: *Top left (a)* GMRT 240 MHz image of A4038 with a beam of $15'' \times 15''$. Traces of an extension toward the NW of the relic are visible. Contours are at -2.7, 2.7, 3.6, 4.5, 7.2, 10.8, 21.6, 43.2, 86.4, 138.6 mJy beam^{-1}. *Top right (b)* The 240 MHz image convolved with a beam of $25'' \times 25''$. The NW extension is detected. Two other components are also detected toward east of A4038_11 (the cD). The DSS R band image is shown in grey scale. Contours are at -4.5, 4.5, 6.0, 7.5, 12.0, 18.0, 36.0, 72.0, 144.0, 231.0 mJy beam^{-1}. *Bottom left (c)* Image at 606 MHz with a synthesized beam of $25'' \times 25''$. Contours are at -1.2, 1.2, 1.6, 2.0, 3.2, 4.8, 9.6, 19.2, 38.4, 61.6 mJy beam^{-1}. *Bottom right (d)* Same region as in the 240 MHz image at 150 MHz with a synthesized beam of $25'' \times 25''$. Contours levels are the same as in Fig. 4.1d.

as the 'NW-Extension' or 'NW-Ext' for brevity, hereafter. The other two new components detected east of A4038_11 are referred to as C1 and C2 (see labels in Fig. 4.2b). The NW-Ext has a linear size of 84 kpc along the N-S (angular size of 2.4′) and 56 kpc along the E-W (angular size of 1.6′). The average surface brightness of the NW-extension at 240 MHz is ∼7 mJy beam^{-1} (beam=25″ × 25″).

The image at 606 MHz convolved to a resolution of 25″ × 25″ is presented in Fig. 4.2c. The 150 MHz image showing the same region as Fig. 4.2b is presented in Fig. 4.2d for comparison. The surface brightness detections limited to ∼ 2 mJy beam^{-1} at 606 MHz and to ∼ 20mJy beam^{-1} at 150 MHz resulted in non-detections of the NW-Ext, C1 and C2 at these frequencies. These non-detections imply that the limits on the spectral indices of these features are $\alpha_{240}^{606} < -2.2$ and $\alpha_{150}^{240} > -1.3$ ($S \propto \nu^{\alpha}$).

We refer to the high surface brightness regions of the relic detected at the frequencies 150, 240 and 606 MHz (Figs. 4.1) as the 'main relic'. The reference to 'the relic', hereafter will mean the 'main relic' together with the NW-Ext.

4.3.2 Integrated Spectrum

The total flux density in a box enclosing the relic was found using the images with resolutions 25″ × 25″ at each of the frequencies (150, 240 and 606 MHz). Total flux densities were also estimated at 1400 and 74 MHz using the NVSS (Condon et al 1998) and the VLSS (Cohen et al 2007) images, respectively, using boxes of same dimensions. These images are presented in Figs. 4.3. The positions of sources A4038_10 and A4038_11 are marked in Figs. 4.3. To obtain the flux density of the relic, contribution from the sources A4038_11 and A4038_10 had to be subtracted from the total flux density in the box. The high resolution images at 1288 and 606 MHz were used to find the flux densities of the sources A4038_11 and A4038_10. Since these sources are embedded in the diffuse emission of the relic at 74, 150, 240 and 1400 MHz and could not be resolved, the spectral index between 1288 and 606 MHz was used to estimate their contributions at these frequencies. The

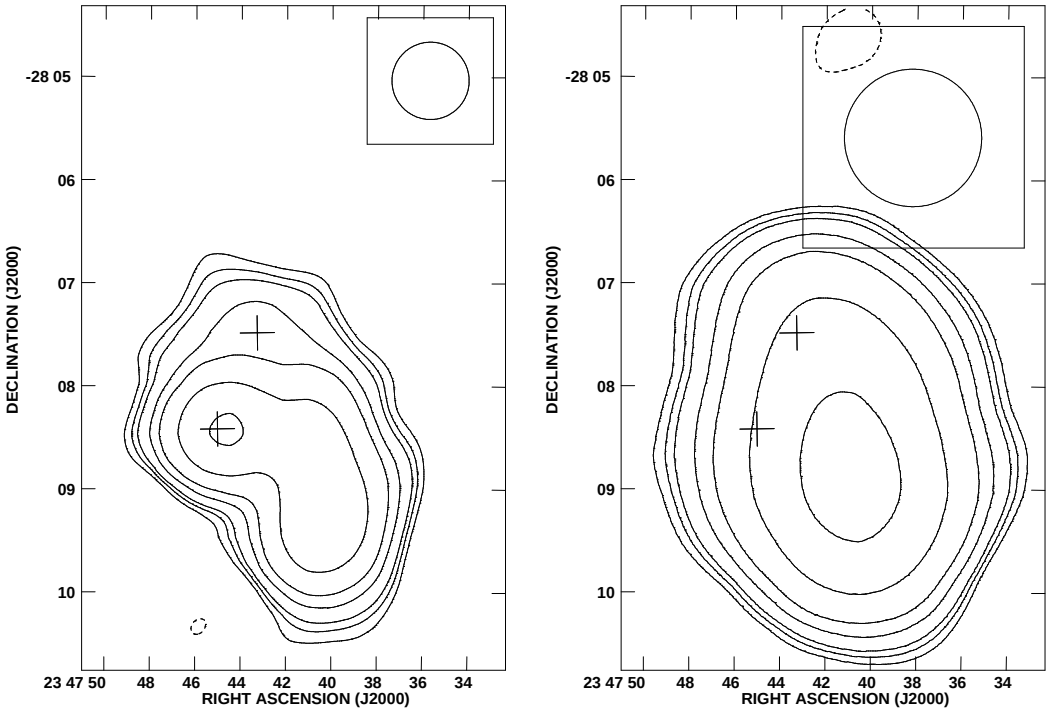

FIGURE 4.3: *Left* Image of A4038 from the NVSS (1400 MHz)(Condon et al 1998). The synthesized beam is $45'' \times 45''$. *Right* VLSS (74 MHz)(Cohen et al 2007) image of A4038. The synthesized beam is $80'' \times 80''$. Contours are at (left) -1.35, 1.35, 1.80, 2.25, 3.6, 5.4, 10.8, 21.6 mJy beam^{-1} and (right) -300, 300, 400, 500, 800, 1200, 2400, 4800 mJy beam^{-1}.

spectral indices (α_{606}^{1288}) of A4038_11 and A4038_10 were found to be -0.55 and -0.88, respectively. It was assumed that the spectral indices are constant over the frequency range of 74 to 1400 MHz. In Table 4.3 the flux densities of the discrete sources and the relic are listed. The flux densities at 29, 327, 408 and 843 MHz corrected for the contributions from the sources A4038_11 and A4038_10 and also other sources in the beams as reported by SL01 are given in Table 4.3. The integrated spectrum of the relic is plotted in Fig. 4.4.

Flux densities of the relic at 80 and 160 MHz are reported to be 19.0 ± 2.7 Jy and 4.3 ± 0.5 Jy respectively, by SL01. However since we have better estimates at 74 and 150 MHz (Table 4.3), we do not use the SL01 values at 80 and 160 MHz.

TABLE 4.3: Integrated flux densities of the relic in A4038.

Freq. (MHz)	Flux density (total) Jy	A4038_11 mJy	A4038_10 mJy	relic Jy
29	42 ± 7	–	–	32 ± 7[a]
74	12.6 ± 1.5	117 ± 20	24 ± 5	12.45 ± 1.5[b]
150	5.26 ± 0.11	84 ± 10	13 ± 2	5.16 ± 0.11
240	3.04 ± 0.06	65 ± 5	9.0 ± 2.0	2.96 ± 0.06
327	1.54 ± 0.15	–	–	1.44 ± 0.15[a]
408	0.96 ± 0.11	–	–	0.91 ± 0.11[a]
606	0.427 ± 0.008	39.0 ± 3.0	4.5 ± 0.8	0.38 ± 0.008
843	0.21 ± 0.03	–	–	0.17 ± 0.03[a]
1288	-	25.0 ± 2.0	2.1 ± 0.5	–
1400	0.086 ± 0.004	23.0 ± 0.1	2.3 ± 0.1	0.060 ± 0.004[c]

[a] Table 3 in Slee et al (2001).

[b] VLSS

[c] NVSS

4.3.3 Model Fit to the Integrated Spectrum

Radio relics are believed to be either remnants of radio galaxies or sites of accretion shocks where particles are accelerated to relativistic energies. The remnants of radio galaxies can be ageing lobes or lobes compressed by shocks in the ICM. In the case of A4038, SL01 attempted a fit considering the relic as a remnant of a radio galaxy. The SL01 fits were based on estimates of volume and magnetic field using the extent of the relic (LLS=56 kpc) as detected by SL01 at 1.4 GHz. These can no longer be considered due to discoveries of new features at lower frequencies as described earlier. Further the models considered by SL01 neglected energy losses due to expansion of the lobes. We describe our attempt to fit the integrated spectrum of the relic with a model which overcomes the above mentioned drawbacks.

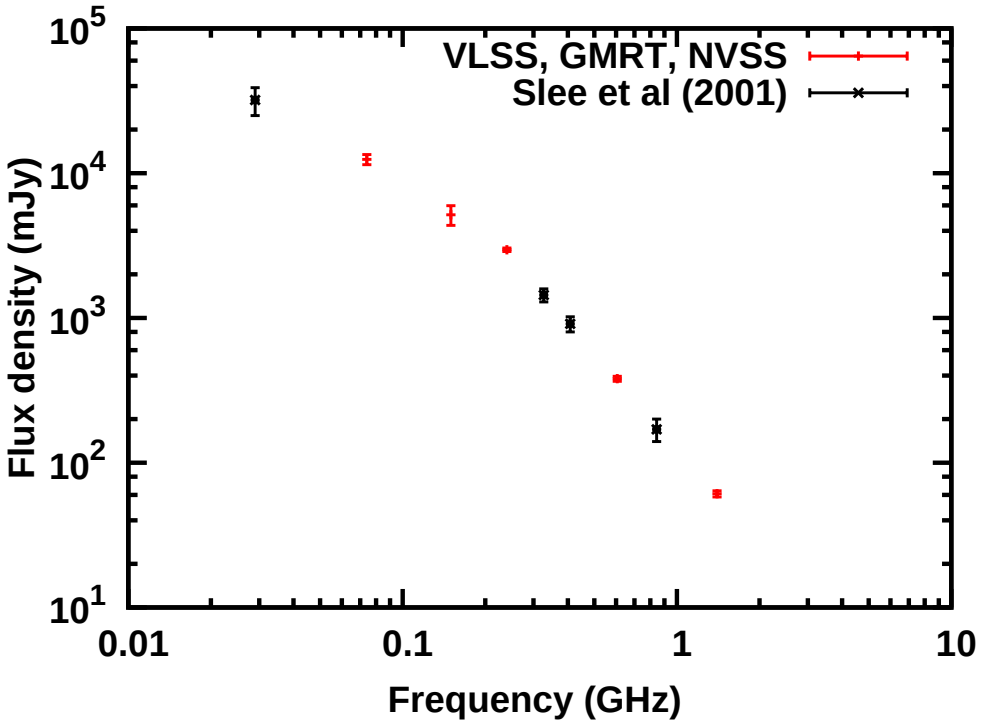

FIGURE 4.4: Integrated spectrum of the relic in A4038 (Table 4.3). The red points mark values estimated using our GMRT images (150, 240 and 606 MHz) and the images from the VLSS (74 MHz) and the NVSS (1400 MHz). Black points mark values from Slee et al (2001).

Revival of fossil radio lobes by adiabatic compression by passage of shocks is one of the models favoured for radio relics (Ensslin & Gopal-Krishna 2001, EG01 hereafter). The framework of EG01 (described in Sec. 3.6) considers revival of fossil radio cocoon by adiabatic compression due to shocks in the ICM. The evolution of the spectrum of a radio galaxy before and after the jets cease to be active and after adiabatic compression of the lobes occurs can be obtained. Energy losses due to synchrotron, inverse Compton (IC) and expansion are accounted for. There are five phases of evolution, viz. injection, expansion, lurking, flashing and fading. These are considered under scenarios A (relic at cluster centre), B (relic at cluster periphery) and C (relic powered by a radio galaxy).

The largest linear extent of the relic in A4038 is 210 kpc. It is is located close to the cD galaxy and resides almost at the cluster centre. This makes scenario A, which considers the relic to be close to the cluster centre, relevant for obtaining the model fit for the spectrum of the relic. The volume of the complete relic was

TABLE 4.4: Model fit parameters for the A4038 relic

Phase		Δt (Gyr)	τ (Gyr)	b	V (Mpc^3)	B (μG)
0	Injection	0	0.005	1.8	0.00200	1.3460
1	Expansion	0.0054	0.01	1.2	0.00340	0.9528
2	Lurking	0.05	∞	0	0.00340	0.9528
3	**Flashing**	0.3	-0.52	2.0	0.00061	3.0000
4	Fading	0.1	∞	0	0.00061	3.0000
0	Injection	0	0.005	1.8	0.00120	1.8886
1	Expansion	0.0054	0.01	1.2	0.00200	1.3370
2	Lurking	0.05	∞	0	0.00200	1.3370
3	Flashing	0.1	-0.22	2.0	0.00061	3.0000
4	**Fading**	0.025	∞	0	0.00061	3.0000

approximated to be the sum of the volumes of the main relic ($110 \times 75 \times 75$ kpc^3) and that of the NW ext (25^3 kpc^3). Magnetic field of 3μG was estimated using the minimum energy condition under standard assumptions. The model spectra were normalized using the observed flux density at 240 MHz.

Best fit in "Flashing Phase": A best fit was obtained when the relic was considered to be in the 'flashing' phase. The parameters used in the model for the best fit are listed in Table 4.4. The spectra in each of the phases with the parameters given in Table 4.4 are plotted in Fig. 4.5 (left). The black line in Fig. 4.5 (left) is the best fit. The estimated duration of the 'flashing' phase is 0.3 Gyr. The model spectra obtained when the value of the duration of the flashing phase (Δt_3) was changed by 30% from the best fit value are plotted in Fig. 4.5 (right) along with the best fit. **Best fit in "Fading Phase"**: A good fit was also obtained if the relic was assumed to be in the 'fading' phase (Table 4.4, Fig. 4.6, left). The duration of the fading phase was 25 Myr. In Fig. 4.6 (right), model spectra with the duration of the fading phase, Δt_4 changed by 30% from the best fit value are shown.

No good fit could be obtained by assuming the relic to be in Expansion or Lurking phases using the EG01 formalism.

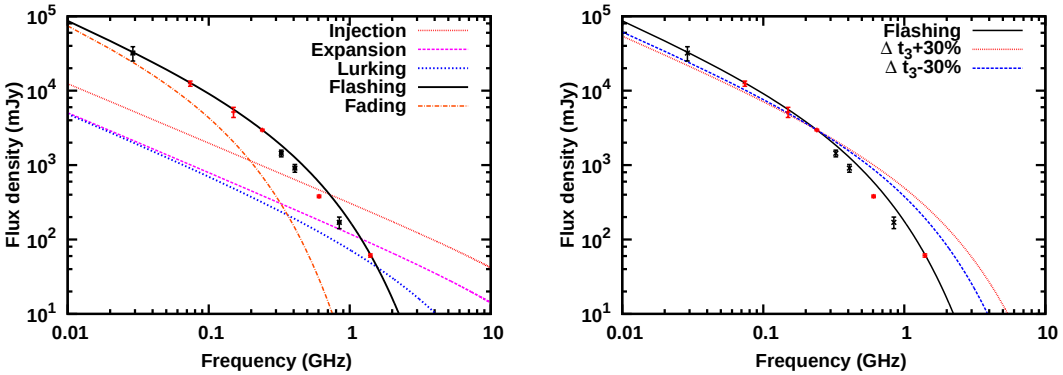

FIGURE 4.5: *Left* The best fit model spectrum in 'flashing' phase along with spectra in other phases. *Right* The observed integrated spectrum of the relic with the best fit and the model spectra with $\Delta t_3 \pm 30\%$. Parameters for this fit are in the first five entries of Table 4.4.

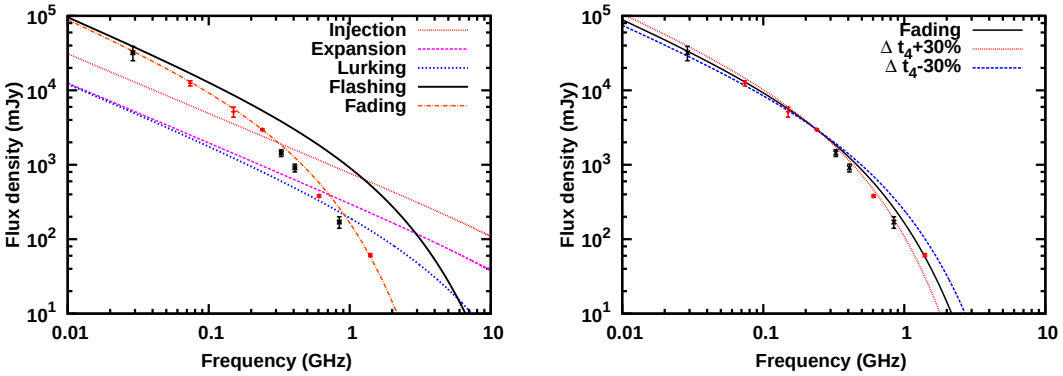

FIGURE 4.6: *Left* The best fit model spectrum in 'fading' phase along with spectra in other phases. *Right* The observed integrated spectrum of the relic with the best fit and the model spectra with $\Delta t_4 \pm 30\%$. Parameters for this fit are in the last five entries of Table 4.4.

4.4 Discussion- I: Abell 4038

Our sensitive low frequency observations with the GMRT have led to the discovery of extended morphology of the relic in A4038 than was known from earlier observations at 1400 MHz. The largest linear extent of the relic in A4038 as seen at 240 MHz is $\sim$ 210 kpc; whereas only 56 kpc was known using 1.4 GHz images. The morphology is elongated along N-S with an extension toward the NW. The bright low frequency extension of the relic, termed as North Relic here (marked in Fig. 4.2 b) has spectral index ~ -2.8 between 240 and 606 MHz and steeper at higher frequencies. A further low surface brightness extension to the relic toward the NW

has been discovered at 240 MHz. Due to limitations of the sensitivities of observations at 150 and 606, the NW-Ext was not detected at these frequencies. Deeper observations at these frequencies are required to detect and determine the spectral index of the NW-Ext and confirm the components C1 and C2 (Fig. 4.2b). We used the adiabatic compression model to fit the integrated spectrum of the relic.

The EG01 model accounts for the energy losses due to expansion and also the resulting change in the magnetic field. Further it also considers the case in which a shock in the ICM compresses lurking radio cocoons and leads to enhanced emission from them. The best fits were obtained in the 'flashing' and the 'fading' phases. The durations of the phases of injection, expansion and lurking are the same in both the cases. However the extent of the compression in the 'flashing' phases differs. In the case of 'flashing' phase being the best fit, the volume changes by a factor of ~ 6, whereas in the case of 'fading' being the best fit, the change is by a factor of ~ 3.3. This implies that the pressure jumps at the shock that caused the compression are factors of ~ 11 and ~ 5 in the 'flashing' and the 'fading' best fit cases, respectively. This was found by using the relation between the compression factor (C) and the pressure ratio (P_1/P_2) given by, $C = (P_1/P_2)^{3/4}$. The pressure jump is related to the Mach number (M) and the adiabatic index γ. Using the pressure ratios and the factor $\gamma = 5/3$ (for thermal gas), M was found to be ~ 3 and ~ 2 in the cases of 'flashing' and 'fading' best fit respectively. The change in the spectral luminosity by factors of 10 is achieved in the compression phase making the relic detectable over the observed frequency range. Considering the similarity in the implications of the best fits in the 'flashing' and 'fading' phases, it is difficult to prefer one more than the other fit. Using the EG01 model we find that to fit the integrated spectrum of the relic in A4038, compression of the cocoon is essential.

In X-rays, no shock has been reported in the cluster A4038. Dunn et al (2005) classify A4038 as a cluster having a weak cooling core. This implies that some dynamical activity in the recent past of A4038 is possible. One of the ways to identify shock is to see the orientation of magnetic fields using polarization maps.

No preferred orientation has been found in the polarization maps by SL01; 4% polarized intensity has been found at 1.4 GHz (SL01).

The remnants of radio galaxies in clusters have been found in the form of bubbles in the ICM (eg. McNamara 2002). The jets of radio galaxies inflate bubbles in the ICM which are detected in high resolution X-ray images as cavities in the ICM. These are often found to be filled with relativistic plasma detectable in radio wavelengths. These bubbles can get detached from the place where they formed and rise in the ICM due to buoyancy. The main relic in A4038 could be such a bubble and the NW-Ext could be an old bubble that has risen by buoyancy. However no cavities in the ICM of A4038 that correlate with the morphology and position of the relic have been reported. This could be due to the effects of projection.

The relic has been considered as a remnant of a radio galaxy in the EG01 model. Over time, the host galaxy would have moved and may not have an AGN any more, preventing identification. The radio images (Figs. 4.2) also indicate a diffuse bridge connecting the relic to the cD. The bridge cannot be an active jet considering that it has a steep spectral index and is not detectable at higher frequencies (young relativistic plasma in the jet has a flat spectrum). If the cD galaxy were the progenitor then it would have been a narrow angle tailed galaxy with the jets pointing toward west.

4.5 Results- II : Abell 1664

4.5.1 Radio Images

Images of A1664 at 150 and 330 MHz using the GMRT are presented in Fig. 4.7a and b respectively. The image at 1400 MHz from the NVSS is presented in Fig. 4.7c. The relic has a circular morphology and has an angular extent of $\sim 6'$ which means a linear extent of $\sim$ 0.927 Mpc at the redshift of A1664. The northern edge of the relic appears connected to an unresolved radio source associated with

the galaxy A1664_3 (Pimbblet et al 2006). No evidence for jets from this source is found. Comparison of the morphologies of the relic at 150, 325 and 1400 MHz reveals that there is variation in the positions of high surface brightness features. At 150 MHz the relic seems to be resolved into two components.

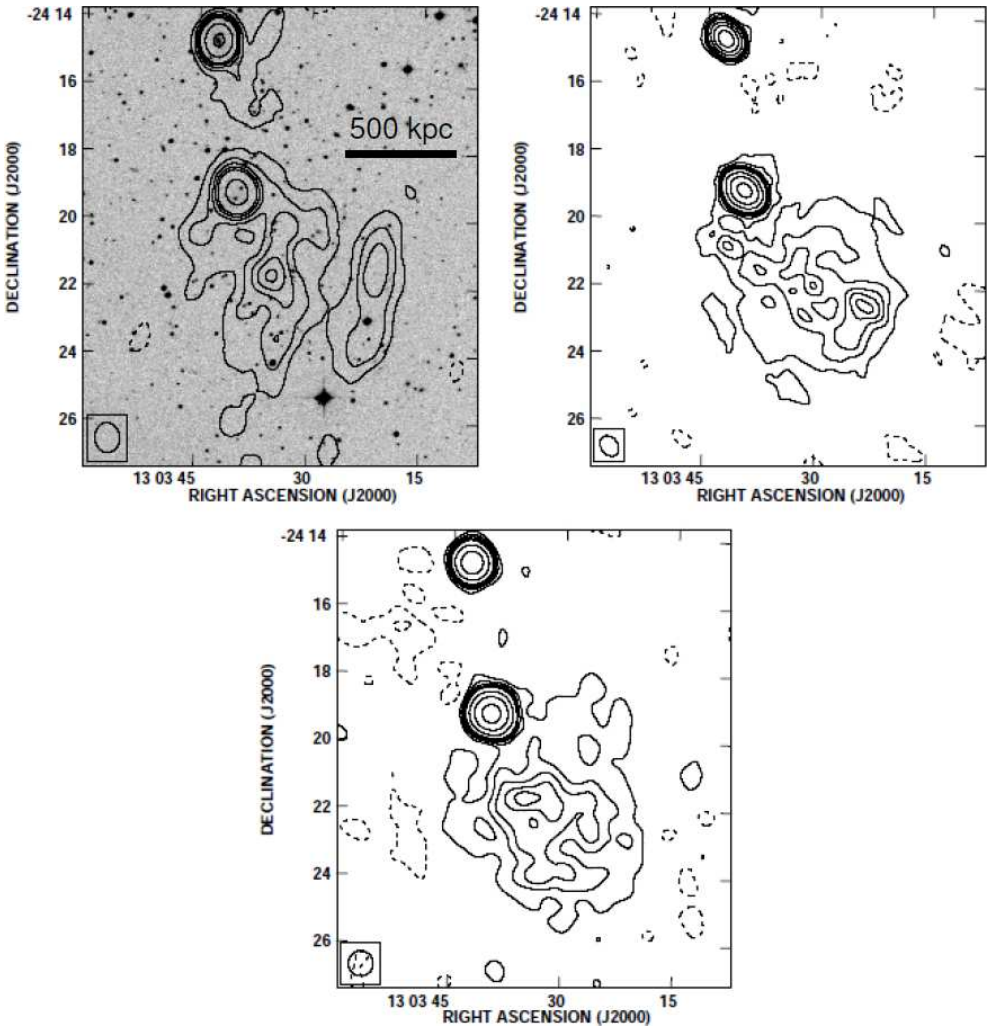

FIGURE 4.7: A1664:*Top Left* (a) GMRT 150 MHz contours overlaid on DSS R-band image in grey scale. Contour levels are at -21, 21, 42, 63, 84, 105, 210, 420, 840 mJy beam^{-1}(synthesized beam = $53'' \times 45''$, P. A.= $4°$). *Top Right*(b) GMRT 330 MHz contour levels at -3.0, 3.0, 6.0, 9.0, 12.0, 15.0, 30.0, 60.0, 120.0 mJy beam^{-1}(synthesized beam = $39'' \times 30''$, P. A.= $40°$). *Bottom*(c) NVSS 1400 MHz contour levels at -1.05, 1.05, 2.10, 3.15, 4.20, 5.25, 10.50, 21.00, 42.00 mJy beam^{-1}(synthesized beam = $45'' \times 45''$).

4.5.2 Integrated spectrum

The flux density in a box enclosing the relic and the radio source A1664_3 was estimated. From higher resolution images, the flux density of A1664_3 was estimated and subtracted. These flux densities are listed in Table 4.5. The integrated spectrum of the relic is plotted in Fig. 4.8 (points with error bars). The spectral indices of the relic, α_{150}^{325} and α_{325}^{1400} are -1.32 ± 0.03 and -0.98 ± 0.01.

TABLE 4.5: Integrated flux densities of the relics in A1664 and in A786.

Freq. (MHz)	A1664_3+relic (total) Jy	A1664_3 mJy	A1664 relic mJy	A786 relic mJy
150	1.811 ± 0.181	561.0 ± 56.0	1250.0 ± 125.0	933.5 ± 90.0
325	0.688 ± 0.030	238.0 ± 10.0	450.0 ± 30.0	-
345	-	-	-	440.2 ± 30.0
606	-	-	-	306.0 ± 8.0
1400	0.178 ± 0.004[a]	71.8 ± 1.0	106.2 ± 4.0	45.9 ± 3.0

[a] NVSS

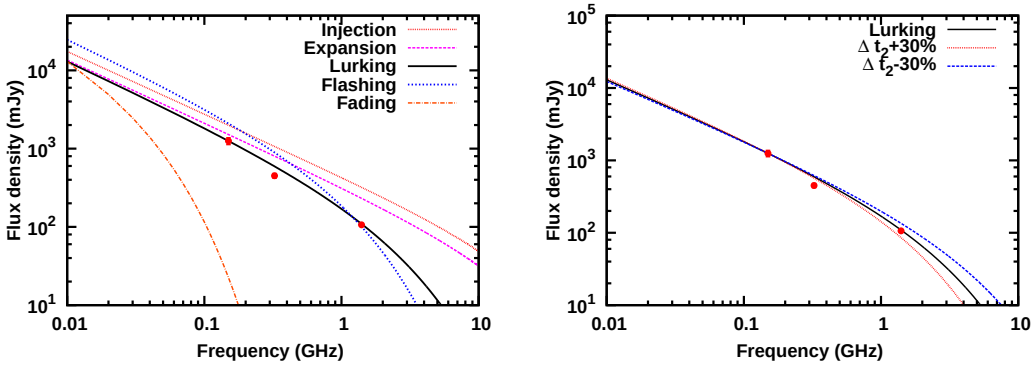

FIGURE 4.8: (*Left*) The integrated spectrum of the relic in A1664 is plotted (Table 4.5). The lines are the spectra obtained from the EG01 model. Solid black line is the best fit ('Lurking Phase') to the integrated spectrum of the relic in A664. Other lines are model spectra in the other phases of evolution. (*Right*) The best fit model spectrum (black line) with the model spectra obtained when the duration of the best fit phase (Δt_2) was varied by 30%. The integrated spectrum (points) is also plotted for reference.

TABLE 4.6: Model fit parameters for A1664 relic.

Phase		Δt (Gyr)	τ (Gyr)	b	V (Mpc^3)	B (μG)
0	Injection	0	0.015	1.8	0.104	0.96
1	Expansion	0.005	0.04	1.2	0.120	0.88
2	**Lurking**	0.04	∞	0	0.120	0.88
3	Flashing	0.03	-0.17	2.0	0.0814	1.14
4	Fading	0.3	∞	0	0.0814	1.14

4.5.3 Model Fits

The relic in A1664 is at a distance of ~ 1.13 Mpc from the centre of the cluster. Among the scenarios described in EG01, the scenario C where the relic is considered close to a cluster radio galaxy is used.

Best Fit in the 'Lurking' Phase: A best fit was found when the relic was assumed to be in the 'Lurking' phase. The best fit parameters are listed in Table 4.6. The duration of the 'Lurking' phase was found to be 4×10^7 yr.

4.6 Discussion- II: Abell 1664

The 150 and 325 MHz images presented above are the first low frequency images of the relic in A1664. These have yielded an estimate of the spectral index of the relic between 150 and 1400 MHz $\sim -1.13 \pm 0.05$. Although the flux density estimates of the relic were obtained only at three frequencies, we attempted a model fit using the EG01 model. The best fit found in the 'Lurking' phase implies that no shock compression is required to produce the relic. This is consistent with the cooling flow at the centre of A1664 (Allen et al 1995).

The NVSS image overlaid on ROSAT (0.1-2.4 keV) image of A1664 is shown in Fig. 4.9. The cluster centre is north of the relic. Recently a detailed study of the cluster has been carried out using *Chandra* by Kirkpatrick et al (2009). The X-ray surface brightness in the cluster centre is elongated and can be approximated to be an ellipse, the major axis of which is at a P. A. of 25° (Kirkpatrick et al 2009). The relic is situated along the same axis toward SW at a distance of 1.13 Mpc

from the cluster centre. The elongation in X-rays is consistent with the optical major axis of the galaxy at the cluster centre. Thus the elongation does not seem to be due to any dynamical activity in the cluster. Therefore the location of the relic along this axis may not be of any significance.

The relic appears connected to the galaxy A1664_3 in the images. However, no evidence for jets from the galaxy connecting to the relic has been found. The location of the relic at the outskirts of the cluster and close to a radio source is similar to the relic in Coma cluster. The Coma cluster relic is at a distance of 2.2 Mpc from the cluster centre and is possibly associated with a radio galaxy seen close to the relic (Ensslin et al 1998; EG01). The cosmological structure formation shocks are believed to be found at cluster peripheries. These could compress cocoons of radio galaxies leading to the formation of relics and/or could accelerate the particles in the thermal gas to form relics. The Coma relic is elongated and has been proposed to have been compressed by an accretion shock (Ensslin et al 1998).

The cluster A1664 is known to be a cooling flow cluster (Allen et al 1995). Most radio halo and relic sources are associated with clusters that have undergone or are undergoing mergers. The case of A1664 is similar to that of A85 which is also a cooling flow cluster with a peripheral relic. The main difference between A85 and A1664 relics is that the relic in A85 has an extent of ~ 100 kpc whereas A1664 relic has an extent ≥ 0.92 Mpc.

The relic in A1664 can be a bubble of radio plasma that has buoyantly risen in the ICM and reached the peripheries of the cluster. As the density of the surrounding ICM decreases the volume of the bubbles can expand. At the location of the relic, the sensitivity of X-ray images is not enough to detect if there is a cavity.

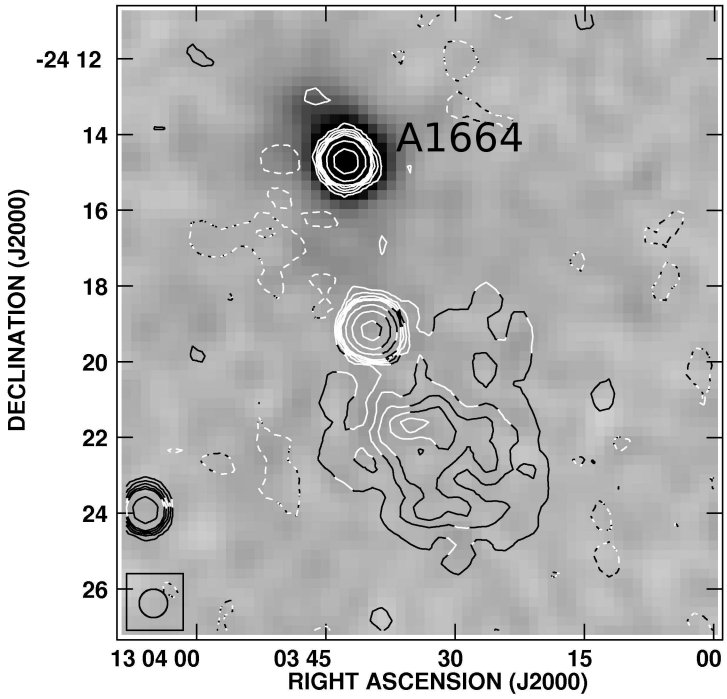

FIGURE 4.9: A1664: 1400 MHz image (contours) overlaid on ROSAT (0.1-2.4 keV) image in grey-scale. Contours are at the same levels as in Fig. 4.7c.

4.7 Results- III : Abell 786

4.7.1 Radio Images

The images of the relic associated with A786 at 150, 345, 606 and 1464 MHz are presented in Figs. 4.10 a, b, c and d. The largest extent of the relic is detected at 345 MHz ($\sim 10'$). A central region with higher surface brightness is seen at 345 and 1464 MHz with low surface brightness extensions along east and west. A large fraction ($\sim 40\%$) of short baseline data at 150 MHz was corrupted due to RFI and had to be discarded. The sensitivity in the 150 MHz image is $\sim$ 10mJy beam^{-1}. The bright central portion of the relic is detected but the weak extensions along the east and west are not detected at 150 MHz. An image at 606 MHz with a resolution of $64'' \times 64''$ is presented in Fig. 4.10c. The A high resolution image at 606 MHz of the same region is presented in Fig. D.2. To the southwest of the relic is a bright unresolved radio source (source R5, Harris et al (1993)). It is presumably a background source not related to the relic.

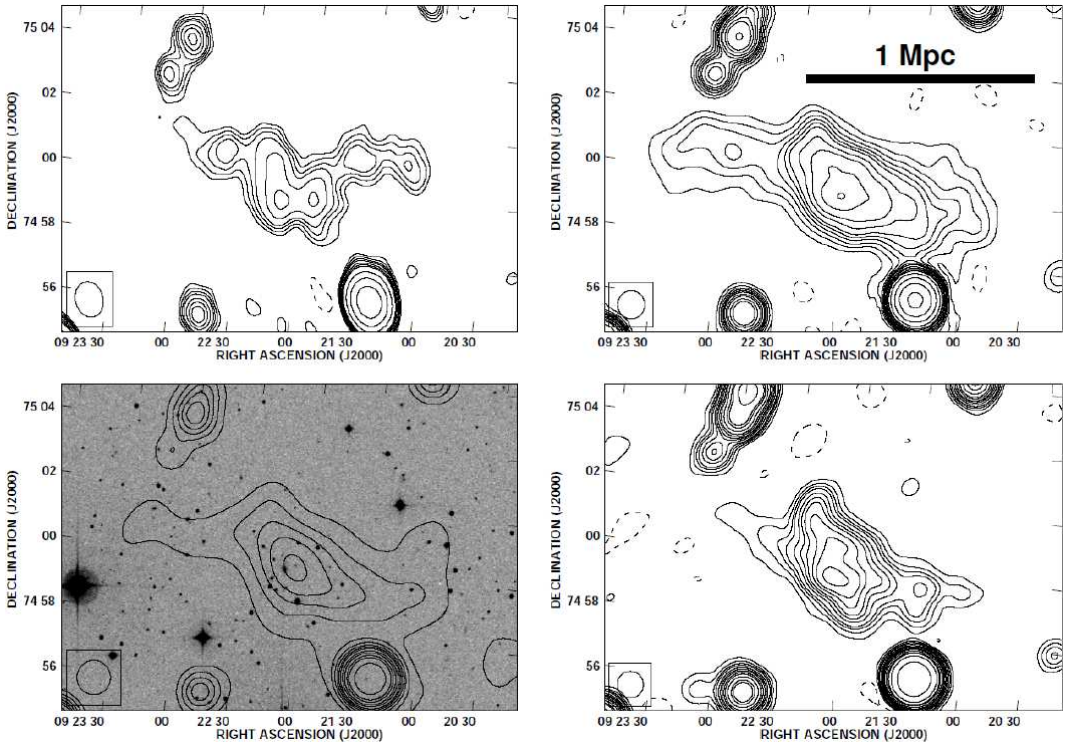

FIGURE 4.10: *Top Left*(a) GMRT 150 MHz. Contour levels are at -30, 30, 40, 50, 60 , 80, 100, 120, 240, 480, 960 mJy beam^{-1}(synthesized beam= $67'' \times 52''$, P.A.= 22°). *Top Right*(b) WSRT 345 MHz. Contour levels are at -2.4, 2.4, 4.8, 7.2, 9.6, 12.0, 14.4, 19.2, 24.0, 32.0, 40.0, 64.0, 128.0, 256.0, 512.0 mJy beam^{-1}(synthesized beam= $52'' \times 51''$, P.A.= 7°). *Bottom Left*(c) GMRT 606 MHz contours overlaid on DSS R band image in grey scale. Contour levels are at -7.0, 7.0, 15.0, 22.5, 30.0, 37.5, 45.0, 60.0, 75.0, 100.0, 125.0, 200.0 mJy beam^{-1}(synthesized beam= $64'' \times 64''$). *Bottom Right*(d) VLA 1464 MHz. Contour levels are at -0.3, 0.3, 0.6, 0.9, 1.2, 1.8, 2.4, 3.0, 4.0, 5.0, 7.0, 10.0, 12.0, 20.0, 50.0 mJy beam^{-1}(synthesized beam = $50'' \times 50''$).

4.7.2 Integrated Spectrum

The integrated flux densities of the relic obtained from the images at 150, 345, 606 and 1400 MHz are reported in Table 4.5. In the highest resolution image ($\sim 7'' \times 3''$ (P.A. -5), not presented since the relic was marginally detected in it) at 606 MHz, two unresolved sources were detected in the region of the relic. The positions (J2000) of these sources are RA 09h22m19.096s DEC +75d01′41.95″ and RA 09h22m24.77s DEC +75d01′43.92″ (separation $\sim 20''$). The location of these sources is marked as 'CS' in the image with a resolution $\sim 20'' \times 16''$ presented in the Appendix D. The total flux density of these two sources at 606 MHz is 7.6 mJy. Assuming a spectral index of -0.8 for these, the flux densities at 150, 350

TABLE 4.7: Model fit parameters for the relic near A786.

Phase		Δt (Gyr)	τ (Gyr)	b	V (Mpc^3)	B (μG)
0	Injection	0	0.015	1.8	0.046	1.5032
1	Expansion	0.012	0.01	1.2	0.119	0.8
2	**Lurking**	0.06	∞	0	0.119	0.8
3	Flashing	0.02	-0.04	2.0	0.0297	2.0
4	Fading	0.06	∞	0	0.0297	2.0

and 1400 MHz were estimated and subtracted from the flux densities of the relic. The integrated flux densities of the relic after this correction are reported in Table 4.5. The spectrum of the relic is plotted in Fig. 4.11.

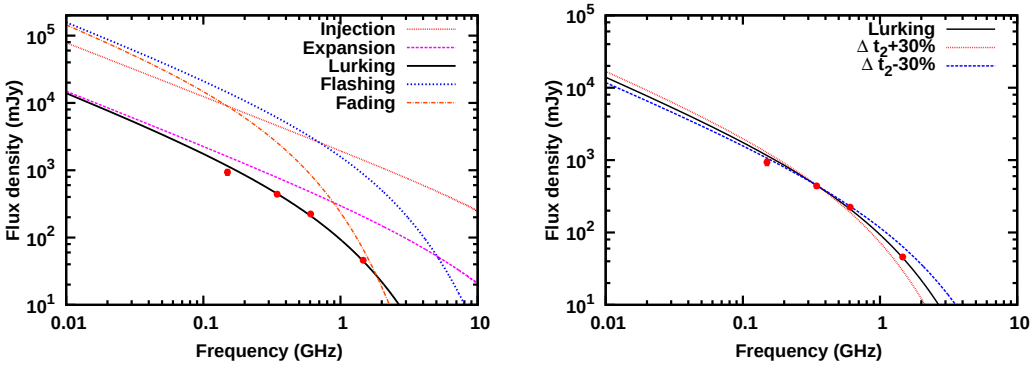

FIGURE 4.11: Integrated spectrum of the relic near A786 is shown by points with error bars. *Left* Each curve is a spectrum in a Phase (labelled in the legend) in the model. The solid black line is the best fit spectrum in the 'Lurking' phase. *Right* The curves representing spectra when the duration of the best fit phase was changed by 30%. The best fit curve and the integrated spectrum are plotted for reference.

4.7.3 Model fit to the integrated spectrum

The EG01 model was used to fit the integrated spectrum of the relic near A786. A best fit was obtained when the relic was assumed to be in the 'Lurking' phase. The best fit parameters are reported in Table 4.7. The duration of the Lurking phase phase was found to be 6×10^7 yr. Assumptions of the relic being in the any other phase did not yield good fits.

4.8 Discussion-III: Abell 786

The relic is about 5 Mpc from the centre of the cluster A786 in the plane of the sky. In Fig. 4.12 the 345 MHz contours are overlaid on the ROSAT HRI image (0.1-2.4 keV). There are two optical galaxies near the brightest central region of the relic, called D and E by Harris et al (1993), which have redshifts consistent with that of the cluster A786. For this reason the relic has been considered associated with the cluster A786.

The integrated spectrum of the relic near A786 is curved. The spectral index between 150 and 606 MHz is $\sim -0.8 \pm 0.1$ and it steepens to a value of $\sim -2.1 \pm 0.06$ between 606 and 1400 MHz. A best fit in 'Lurking' phase was obtained. According to the model fit the radio galaxy responsible for depositing the relativistic plasma in the ICM had been active for $\sim 1.5 \times 10^7$ yr. The total time elapsed since the jets of the radio galaxy ceased to be active is $\sim 7 \times 10^7$ yr. Within this timescale the progenitor galaxy would have travelled a distance of 700 kpc with a velocity of 1000 km s^{-1}(typical at cluster centre) and 70 kpc with a velocity of 100 km s^{-1} (typical velocities in galaxy groups). Due to this large uncertainty, no progenitor can be identified with confidence.

The relic near A786 is one of the largest diffuse emission (LLS$\sim$ 1.6 Mpc) regions known in the Universe which cannot be associated with any one galaxy. Such large scale filamentary radio emission is rare and has been associated with filaments of galaxies or cluster peripheries when detected (eg. ZwCl 2341.1+0000, Bagchi et al 2002 and A3376, Bagchi et al 2006). Structure formation shocks are believed to be responsible for such sources. Ensslin et al (1998) have discussed this relic as a candidate for accretion shock compressed relic. However due to lack of information regarding the temperature and velocity dispersion of the cluster A786, the expected shock radius and polarization could not be determined (Ensslin et al 1998). Our fit to the integrated spectrum requires no compression by accretion shock.

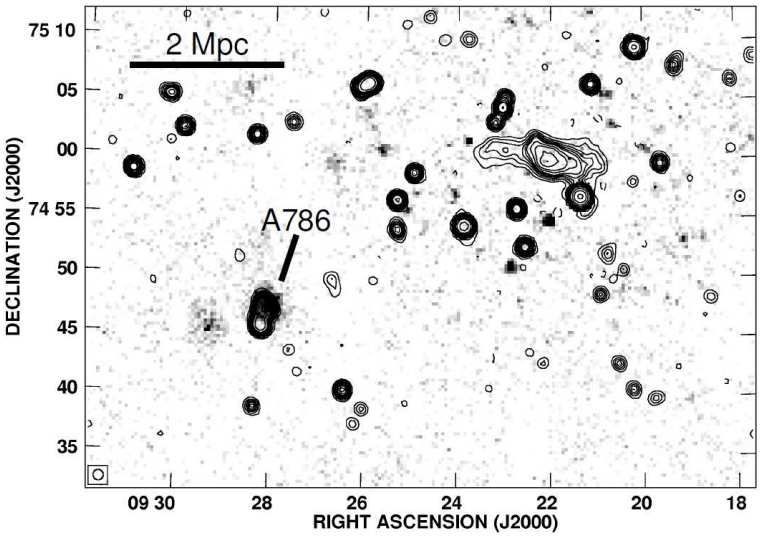

FIGURE 4.12: Contours at 345 MHz (WSRT) overlaid on the ROSAT HRI (0.1-2.4 keV) image. The cluster A786 lies to the southeast of the relic and is seen as a bright source in X-rays. A radio galaxy resides at the centre of A786.

4.9 Summary

A low frequency study of three radio relics is presented. The 150, 240 and 606 MHz images of A4038 have revolutionized the picture of the relic known earlier. New features of the relic are uncovered extending the largest linear size of the relic from 56 kpc to 210 kpc. The newly discovered emission have spectral indices $\alpha \leq -1.8$. A low surface brightness feature is discovered to the north west of the relic which could be a bubble blown out by a radio galaxy rising in the ICM of A4038 by buoyancy. Our fit using the EG01 framework to the integrated spectrum of the relic reveals that shock compression is required.

The relic in A1664 was imaged at 150 and 325 MHz with the GMRT. These images and the NVSS image at 1400 MHz were used to construct the integrated spectrum of the relic in A1664. The spectral index of the relic in A1664 is estimated to be $\alpha \sim -1.13 \pm 0.05$ over the range of frequencies 150 to 1400 MHz. A best fit to the integrated spectrum of the relic in A1664 was obtained in the 'lurking' phase. This is consistent with absence shocks inferred from the cooling flow at the cluster centre.

The images of the relic near A786 at 150, 345, 606 and 1464 MHz were used to construct the integrated spectrum. The integrated spectrum was best fit in the EG01 framework in the 'lurking' phase. This relic which is unique in its location – ~ 5 Mpc from the centre of the cluster A786 is thus consistent with a remnant of a radio galaxy.

Chapter 5

Relics of Radio Galaxies

Dwarakanath, K. S. & **Kale, R.** 2009, ApJ Letters, 698, 163

5.1 Introduction

So far multi-wavelength studies of radio halos and relics in clusters of galaxies which were selected from known sample of such sources have been presented. Those sources were discovered by examining the regions of known clusters of galaxies in the NVSS (Giovannini et al 1999). Here we present a sample of radio relics identified from all sky surveys based on the steepness of their spectra. Identification, deep imaging and spectral modelling of such sources forms the content of this chapter.

5.1.1 Steep Spectrum Sources

Sources with steep spectra (α < -1.5; S $\propto \nu^{\alpha}$) at low radio frequencies ($\nu <\sim$ 1 GHz) are interesting to study from many points of view. Such sources could be (a) pulsars (millisecond, or, otherwise), (b) halos in galaxy clusters, (c) relics of double radio sources, or, (d) high redshift radio galaxies. Although sources of this kind are known, more in some category than in the other, they are rather

rare. Multi-frequency studies of these objects are even rarer. In this background, it is interesting to follow up steep-spectrum sources identified from sensitive low-frequency surveys.

5.1.2 Earlier Studies

Several studies of steep spectrum sources extracted from various radio surveys have been carried out. Based on the radio surveys at 38 and 178 MHz, Baldwin and Scott discussed sources with spectra steeper than -1.2 and concluded that about half of these sources are associated with clusters of galaxies (Baldwin & Scott, 1973). Komissarov and Gubanov (1994) modeled the evolution of the synchrotron spectrum of a number of steep-spectrum sources ($\alpha <$ –2.0) found in the centers of rich clusters. The spectra of radio relics in galaxy clusters were modeled by Slee et al (2001) and Kaiser and Cotter (2002). Gopal-Krishna et al (2005) extracted a sample of 52 sources from the Ooty lunar occultation survey, Molonglo 408 MHz surveys MC1, MC2 and MIT-Greenbank survey. The spectral indices of sources in this sample in the frequency range 300 MHz - 5 GHz are steeper than -1.1 but flatter than -1.5. This study detected many radio sources in the redshift range 0.4 - 2.6, some of them in galaxy clusters. There appear to be some radio sources in this sample which are at redshifts even beyond 2.6. Klamer et al (2006) have studied a sample of 76 steep spectrum (α in the range -1 – -1.6) sources extracted from the SUMSS and the NVSS surveys to find high z radio galaxies and advance a plausible cause behind the z-α correlation. Cruz et al. (2006) studied a sample of 68 sources extracted from the 6C(151MHz) survey. The spectral indices (between 151 and 1400 MHz) of these sources are in the range -1 – -1.4 and these sources are confined to $\sim$ 0.4 sr of the sky. The redshifts of these sources are in the range 0.2 - 3.3. Parma et al (2007) studied a sample of steep-spectrum ($\alpha < -$ 1.3) sources selected by comparing the NVSS and the WENSS catalogs and found six dying sources and three restarted sources.

5.1.3 Prospects for New Studies

Recently, results from the VLA 74 MHz-survey have become available. This survey has a resolution of $\sim 80''$ with an average rms of ~ 0.1 Jybeam^{-1} (Cohen et al 2006). In the Data Release I the area covered is ~ 6 sr. This survey is the most sensitive survey to date in this frequency range. This survey data can be effectively used to identify the steep-spectrum sources. On similar lines of motivation, a limited area of the sky (~ 0.05 sr) was analyzed by Cohen at al (2004) and further followed by imaging in the near-infrared by Jarvis et al (2004). The radio sources in their list had spectral indices (between 74 and 1400 MHz) in the range -1.2 – -1.8. These studies have yielded potentially interesting candidates for high redshift radio galaxies, relics of double radio sources, and cluster halo sources.

5.2 Sample Selection

In order to select steep-spectrum sources, the Data Release I of the VLA 74-MHz survey (VLSS) and the 1.4 GHz NRAO VLA Sky Survey (NVSS) were used. The synthesized beams of the VLSS and the NVSS surveys are $\sim 80''$ and $45''$ respectively. The detection limits of the VLSS and the NVSS surveys are ~ 0.5 Jy/beam and 2 mJy/beam respectively. The source positions in the VLSS ($\sim$ 32000 sources) were compared with those of the NVSS sources ($\sim$ 1.8 million sources). More than $\sim 90\%$ of the sources in the VLSS had a counterpart in the NVSS within $\sim 15''$ – well within the expected value based on the positional uncertainties in the two surveys.

5.2.1 Sources with Extremely Steep Spectra

The spectral indices of all the sources were estimated between 1420 and 74 MHz. The distribution of spectral indices mimics a Gaussian distribution with a mean spectral index of -0.79 with a σ of -0.2. These values are consistent with those obtained in earlier high frequency surveys. Sources which have spectral indices

greater than, or, equal to -1.8 (mean+5σ) were selected. These are continuum sources with the steepest spectra that have been studied yet. There were 38 such sources in the VLSS. Further selection was based on their possibility of being extended radio sources. The NASA Extragalactic Database (NED) and the SIMBAD were searched for any other information about these sources. Of the 38, 12 of them have been identified as either a 'galaxy' or a galaxy cluster based on the APM/ROSAT/2MASX surveys and RBS/Zwicky/ROSAT catalogues. Some of these also have an optical magnitude measurement. In addition, there are 3 more sources which do not have an optical counterpart, but are considered 'extended' based on the NVSS data. A total of 15 sources were shortlisted for imaging at low frequencies with high resolution. For the purpose of this chapter, hereafter, 'steep-spectrum sources' are those which have spectral indices steeper than -1.8.

5.3 Radio Observations

Of the 15 sources, two sources 0741+7414 (ZwCl 0735.7+7421) and 0041-0923 (Abell 85) have already been imaged at 330 and 1400 MHz with the VLA (Cohen et al 2005; Slee et al 2001; Young 2004) with interesting results regarding their nature. The remaining 13 sources were observed at 330 MHz with the VLA in the A configuration ($\sim 10''$ resolution) during 2007 June-September. The observations were carried out in 4 IF mode with a bandwidth of 6.25 MHz and 16 channels. The centre frequencies of the two bands were 321.5 and 328.5 MHz, respectively. In each of the observing session 3-4 sources were cycled through for a total of 6-8 hr giving an integration time of $\sim$ 2 hr on each source, but with better visibility coverage.

Of the 13 sources, data on 4 sources had to be discarded due to poor quality resulting from the problems related to the VLA to EVLA transition. Nine sources were imaged with the VLA successfully. These 9 sources were also observed with the GMRT at 1287 MHz. The observations were carried out during 2008, May 5-15. A 16 MHz bandwidth over 128 channels around the centre frequency of

1287 MHz was used. Two sources were cycled through in an observing session of $\sim$ 10hr, giving an integration time of $\sim$ 5hr per source.

Both the VLA and the GMRT data were analysed using AIPS. About 10-30% of data were lost to RFI in the VLA and in the GMRT data.

5.4 Radio Images and Integrated Flux Densities

All the nine sources except one were detected at both the frequencies. The undetected source was a result of confusion from a brighter source in the lower resolution VLSS and NVSS surveys. Images of the relevant portions of the eight fields are given in Figures 5.1 - 5.4. Overlays of the radio contours on the optical and the 2μ All Sky Survey images in grey scale are shown. The integrated flux densities of the steep spectrum sources estimated from these images are given in Table 5.1. The possible identifications of the radio sources with optical and X-ray sources are mentioned in the note to Table 5.1.

5.4.1 Morphologies of the Steep Spectrum Sources

The images at 330 and 1287 MHz with resolutions $\sim 10''$ were used to study the morphologies of these sources. The most striking feature of the morphologies of the relic sources discussed here is that almost all have $\sim$double lobed morphology. However none of them show evidence for a core and jets like an active radio galaxy shows. Comparison of the radio sources with the optical, 2MASS and X-ray images showed only a few possible associations. These are of sources 0128B, 1152, 2216 and 2345 (See the note in Table 5.1). If these are at redshifts ~ 0.2, then the linear sizes are $\sim$ 300 kpc. Thus these do not seem to be the Mpc scale 'radio relics' associated with large scale structure formation shocks. These steep spectrum sources are thus likely to be fossil lobes of radio galaxies or relic radio galaxies.

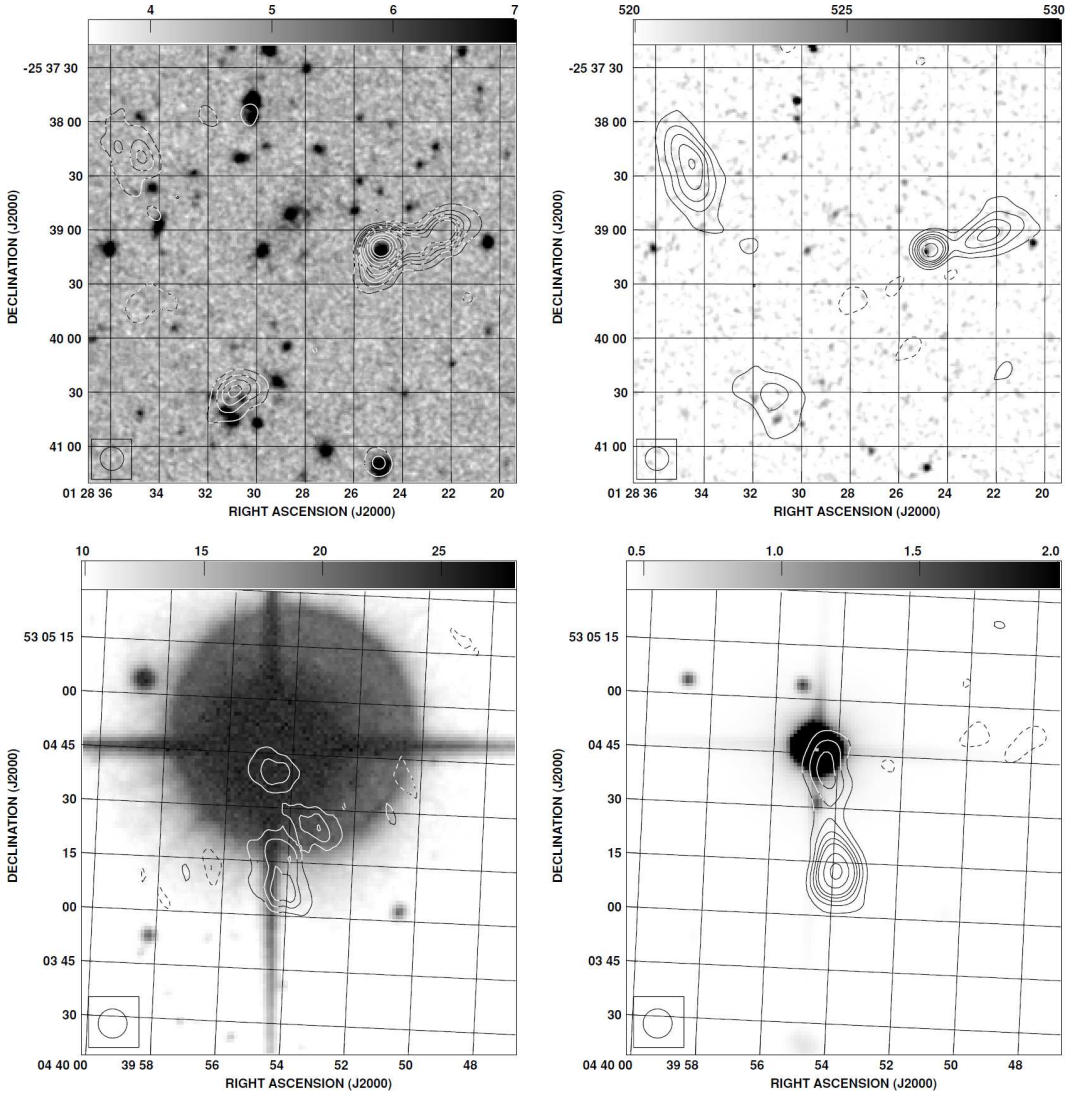

FIGURE 5.1: *top (0128)*: GMRT (left, 1287 MHz) and VLA (right, 328 MHz) radio images (contours) overlaid on optical and 2μ All Sky Survey images (in grey) respectively. The synthesized beam is $13'' \times 13''$ and the rms values are 0.14 (left) and 3.5 (right) mJy beam^{-1}. The contours are at -0.5, 0.5, 1, 1.5, 2, 2.5 and 3.75 (left) and at -8, 8, 16, 24, 32, 40, 60, 80, 120, 160 and 200 (right) mJy beam^{-1}. The source to the NE is 0128A, to the NW is 0128B and to the south is 0128C. *bottom (0439)* : The synthesized beam is $8'' \times 8''$. The rms values are 0.14 (left) and 1.6 (right) mJy beam^{-1}. The contours are at -0.5, 0.5, 1 and 1.5 (left) and at -4, 4, 8, 12, 16, 20, 30 and 40 (right) mJy beam^{-1}.

TABLE 5.1: Integrated flux densities and spectral indices of the relic sources.

Note: All flux densities are integrated values and in mJy. Values within parentheses are 1σ error estimates. The sources with optical identifications are 0128B (2dFGRS S149Z127, z=0.207), 1152 (SDSS J115236.45+373243.7, z=0.229), 2216 (RBS 1842, z=0.136), and 2345 (2MASX J23451645+2157578, z$\sim$ 0.15 (based on the k-z relation of van Breugel et al (1999))). The t_{RE}/t_{CI} is the ratio of the time elapsed since the AGN turned off to the time for which the AGN was on.

Source	R.A. (J2000)	Dec. (J2000)	S74	S328	S1287	α_{328}^{74}	α_{1287}^{328}	t_{RE}/t_{CI}
	hh mm ss	o ′ ″	(VLSS)	(VLA)	(GMRT)			
0128A	01 28 34.551	-25 38 22.90	1200(190)	129(9)	5.5(0.45)	-1.5(.15)	-2.3(.15)	1.9
0128B	01 28 24.697	-25 39 11.15	650(160)	152(7.5)	31.0(0.3)	-1.0(.2)	-1.2(.05)	0.5
0128C	01 28 31.112	-25 40 31.80	180(75)	35.8(2.1)	4.4(0.4)	-1.1(.34)	-1.5(.15)	1.6
0439	04 39 53.930	53 04 12.02	1600(180)	95.6(4.6)	7.8(0.75)	-1.9(.1)	-1.8(.14)	0.8
1133	11 33 45.045	23 25 14.05	1400(118)	150.8(12)	18.1(0.40)	-1.5(.1)	-1.6(.09)	1.6
1152	11 52 36.104	37 32 46.63	4300(102)	387(11)	25.5(2.4)	-1.6(.03)	-1.9(.08)	2.5
2216	22 16 58.007	-17 25 08.03	10800(380)	420(30)	15.9(0.7)	-2.2(.07)	-2.4(.09)	0.2
2345	23 45 15.392	21 57 39.82	2900(114)	257(20)	9.6(1.6)	-1.6(.08)	-2.4(.18)	1.8
2313	23 13 46.837	38 42 16.13	1800(100)	245(12)	28.7(8.5)	-1.3(.08)	-1.6(.25)	1.5
1114	11 14 13.194	15 19 44.12	600(101)	43.3(6)	2.1(0.46)	-1.8(.2)	-2.2(.27)	0.4

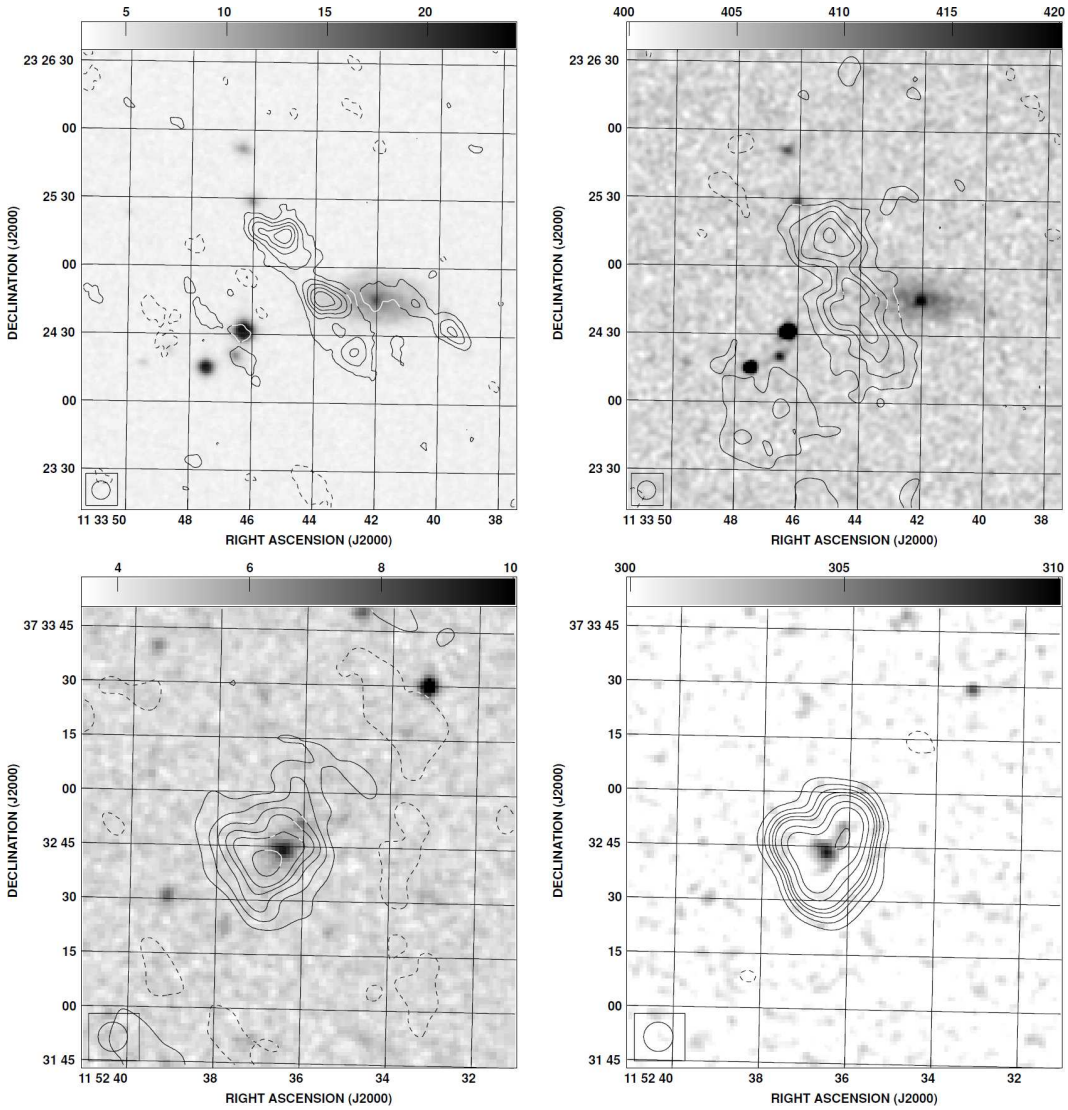

FIGURE 5.2: *top (1133)*: The synthesized beam is $8'' \times 8''$. The rms values are 0.1 (left) and 0.95 (right) mJy beam^{-1}. The contours are at -0.2, 0.2, 0.4, 0.6, 0.8 and 1 (left) and at -2, 2, 4, 6, 8 and 10 (right) mJy beam^{-1}. *bottom (1152)* : The synthesized beam is $8'' \times 8''$. The rms values are 0.3 (left) and 1.3 (right) mJy beam^{-1}. The contours are at -0.6, 0.6, 1.2, 1.8, 2.4, 3 and 4.5 (left) and at -4, 4, 8, 12, 16, 20, 30, 40 and 60 (right) mJy beam^{-1}.

5.5 Modelling the Spectral Ageing of a Radio Galaxy

We model the spectrum of a relic radio galaxy and fit it to that of the relic radio sources. The aim is to learn about the activity timescale of the AGN and the time the radio lobes have spent as relics. Several previous studies of spectral evolution and modeling exist to account for steep spectra (Komissarov & Gubanov 1994;

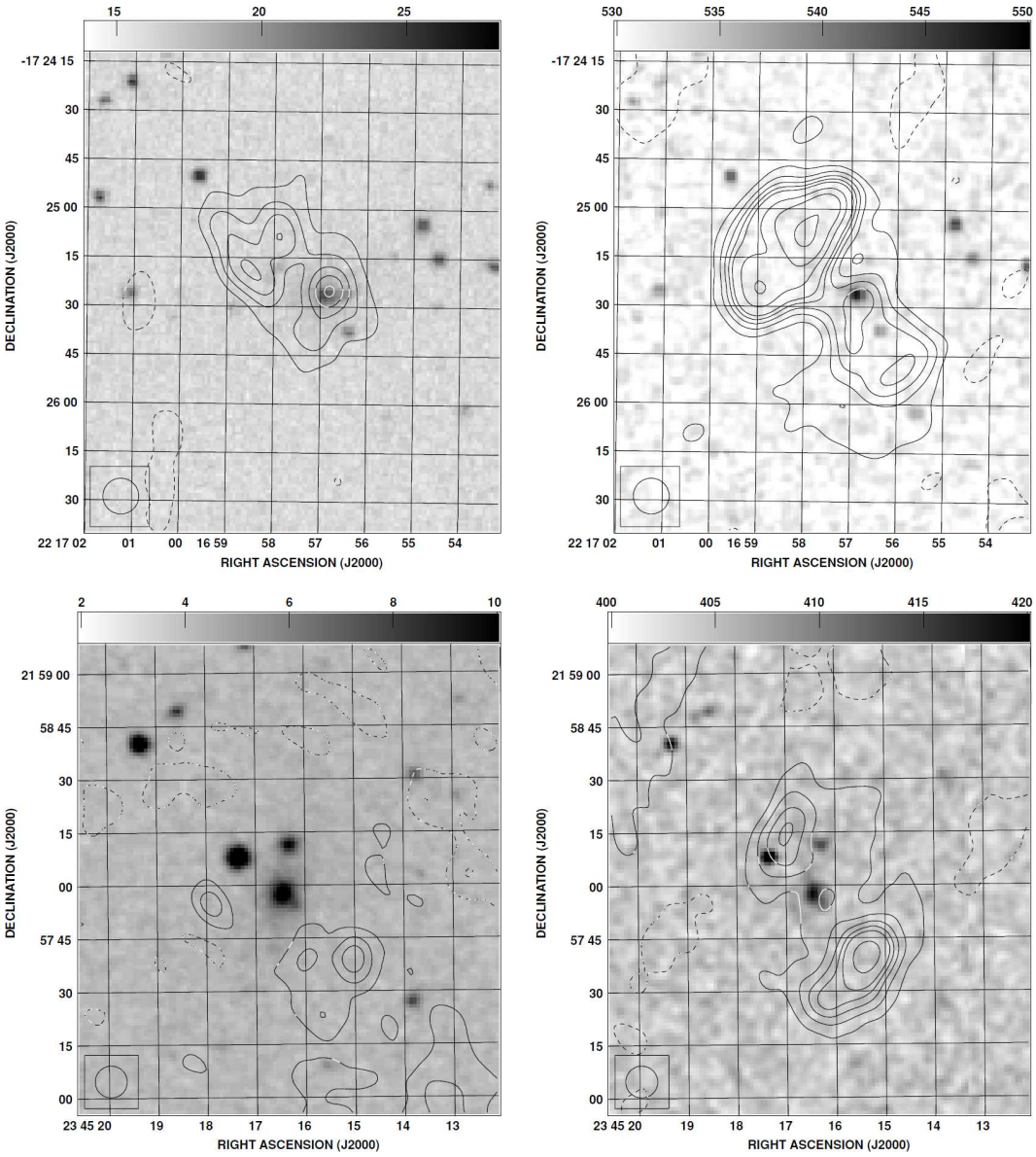

FIGURE 5.3: *top (2216)* : The synthesized beam is $11'' \times 11''$. The rms values are 0.18 (left) and 2.7 (right) mJy beam^{-1}. The contours are at -0.4, 0.4, 0.8, 1.2, 1.6 and 2.0 (left) and at -4, 4, 8, 12, 16, 20, 30, 40 and 60 (right) mJy beam^{-1}. *bottom (2345)* : The synthesized beam is $9'' \times 9''$. The rms values are 0.44 (left) and 3.0 (right) mJy beam^{-1}. The contours are at -0.7, 0.7, 1.4 and 2.1 (left) and at -5.6, 5.6, 11.2, 16.8, 22.4, 28 and 42 (right) mJy beam^{-1}.

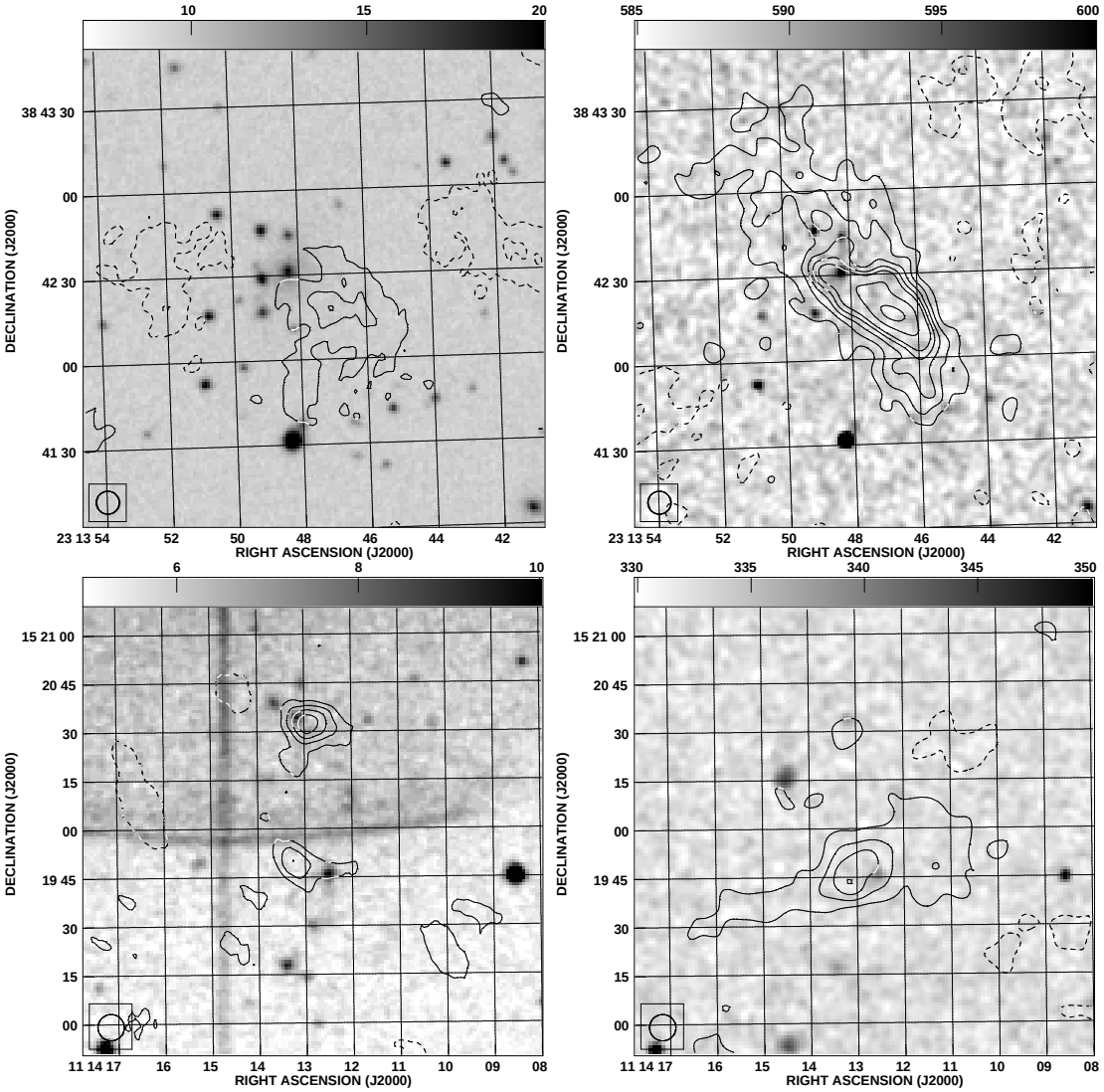

FIGURE 5.4: *top (2313)*: The synthesized beam is $8'' \times 8''$. The rms values are 0.85 (left) and 0.9 (right) mJy beam^{-1}. The contours are at -2, -1, 1, 2 and 3 (left) and -1.6, 1.6, 3.2, 4.8, 6.4, 8, 12 and 16 (right) mJy beam^{-1}. *bottom (1114)*: The synthesized beam is $8'' \times 8''$. The rms values are 0.17 (left) and 1.9 (right) mJy beam^{-1}. The contours are at -0.4, 0.4, 0.8, 1.2 and 1.6 (left) and -3, 3, 6, 9 and 12 (right) mJy beam^{-1}.

Goldschmidt & Rephaeli 1994; Slee et al 2001; EG01). The basic synchrotron theory is discussed in Kardashev (1962) and Pacholzyck (1970).

Spectral steepening of radio sources is due to differential energy losses by synchrotron and inverse Compton radiation. Another source of energy loss is the PdV work done by the lobes while expanding in the external medium. Expansion also results in reducing the magnetic flux density which affects the synchrotron energy losses. To find out the spectrum as a function of time, one needs to start

with an equation which relates the rate of change in the momentum of a relativistic electron to the rates of energy losses. This is same as Eq. 3.1. The solution of this equation and the framework to obtain the spectrum as given by EG01 was discussed in Sec. 3.6.1.

5.5.1 Use of EG01 Formalism

The relevant portions of the EG01 formalism are discussed here. The relic sources discussed here are not necessarily in cluster environments. Most of the sources show double lobed morphology. The 'scenario C' in the EG01 model in which a radio galaxy acts as a smoking gun for the lobes was chosen. The first two phases in the EG01 framework are 'injection' and 'expansion'. The relic sources here could be considered to be in the 'expansion' phase as no evidence for jets and cores is found. An ith phase in EG01 (Sec. 3.6.1.1) is characterized by τ_i and Δt_i which are the timescale for expansion and the duration of the ith phase, respectively. The subscript i is '0' in the injection phase and '1' in the expansion phase.

The timescales of interest here are the activity time of the AGN and the time spent by the lobes after the AGN turned off. These will be referred to as the continuous injection timescale, t_{CI} and the relic timescale, t_{RE} respectively. The time at which the spectrum is obtained is $t = \tau + \Delta t$. The duration of expansion phase is Δt_1 which is the same as t_{RE}. Thus t_{CI} can be given by $t - \Delta t_1$.

The input parameters to the model are (a) current volume of the relic, (b) the source magnetic field, and (c) the initial index α_e ($f_0(p_0) \propto p^{-\alpha_e}$, Eq. 3.5). The current volume of the source was estimated for a linear size of 250 kpc. This linear size corresponds to an angular size of $\sim 1'$ (see Fig. 5.1-5.4) at a redshift of 0.2 ($H_o = 75$ km s^{-1} Mpc^{-1}). A value of $\alpha_e = 2.5$ was assumed. For different sources, a range of t_{RE}, t_{CI} and B were considered. Using Eq. 3.14, the spectra were obtained.

5.6 Model Spectra

A comparison of the model spectra with the observed integrated spectra of the sources was carried out. The model spectrum with a single value of B has an exponential high-frequency cut-off and is unable to fit the observed data. This is a well known problem as was noted by Komissarov & Gubanov (1994) and Slee et al (2001). However if spectra for a range of field strengths are obtained and combined, the sharp cutoff (typical of the 'JP models' where the distribution of the pitch angles of the relativistic electrons is considered to be isotropic) is smoothed out and the integrated spectrum fits the data well. Such a model is considered more physical as different magnetic field strengths are believed to exist in any of such sources (Slee et al 2001).

As the simplest case, we have used superposition of spectra resulting from two values of magnetic field strengths in the source. The equipartition magnetic fields in these steep spectrum sources are in the range 2-10μG and thus the values of magnetic fields in the model were chosen to be in this range. The values of t_{RE} and t_{CI} were varied over a range of 0.01 Myr to 1.2 Gyr. The model spectra were found to be far from the observed spectra beyond this range. For each pair of t_{RE} and t_{CI}, two spectra corresponding to two magnetic field values were obtained and superposed. The values of spectral indices, α_{328}^{74} and α_{1287}^{328} for the resultant spectrum were then compared with those observed for the steep spectrum sources. A match within the error bars on the spectral indices was considered to be a good fit.

5.7 Spectral Fits

In Figure 5.6, the solid black lines denote the best fit spectra to the corresponding data points. The model spectra in these cases were anchored to the 74 MHz point to fix the y-normalization. Although only 3 data points were available, the spectrum could be constrained well as the points are well separated in frequency.

The sensitivity to the parameters t_{RE} and t_{CI} was checked by varying the values of these around the best fit value. The dotted and the dashed lines in the spectra denote the spectra when the t_{RE} was changed by $\pm 30\%$, respectively, keeping the t_{CI} equal to the best fit value. The red and the blue lines denote the spectra when the t_{CI} was changed by $\pm 50\%$, respectively, keeping the t_{RE} equal to the best fit value. A departure from the best fit values is clearly visible when the t_{RE} and the t_{CI} are changed. The ranges of values of the parameters that account for the spectra of the relic sources are : $10 < t_{CI} < 400$ Myr, $15 < t_{RE} < 90$ Myr and $2 < B < 10\mu$G.

5.8 Discussion

A striking feature of the morphologies of the steep-spectrum sources is their double-lobed nature in most cases. The morphologies of the steep-spectrum sources observed here are similar to those of radio galaxies rather than that of halos and relics observed in galaxy clusters. Furthermore, there are no clear indications of cores and jets in any of these sources (with the exception of 0128B) even in the highest resolution ($\sim 4''$) GMRT images at 1287 MHz. The morphologies, the absence of cores and jets and the steep spectra of these sources imply that they are most likely fossil radio sources.

The sources 2216 and 1152 are likely to be associated with clusters of galaxies. A ROSAT source (RASS 105, De Grandi et al 1999) is cospatial with the relic source 2216. It is classified as a galaxy cluster with a luminosity (0.5 - 2.0 keV band) of 2.85×10^{44} erg s^{-1} and a redshift of 0.13. The VLA image of 2216 in greyscale is overlaid with contours of the ROSAT source and shown in Fig. 5.6. The relic 2216 is much smaller in extent compared to the X-ray emission and is located at the centre. It can neither be a giant radio halo source nor a peripheral Mpc size radio relic source in the galaxy cluster. Another relic, 1152 is cospatial with the galaxy cluster 400d J1152+3732 listed by Burenin et al (2007). This cluster is at a redshift of 0.23 and has a luminosity (0.5-2.0 keV band) of 4.95×10^{43}erg s^{-1}.

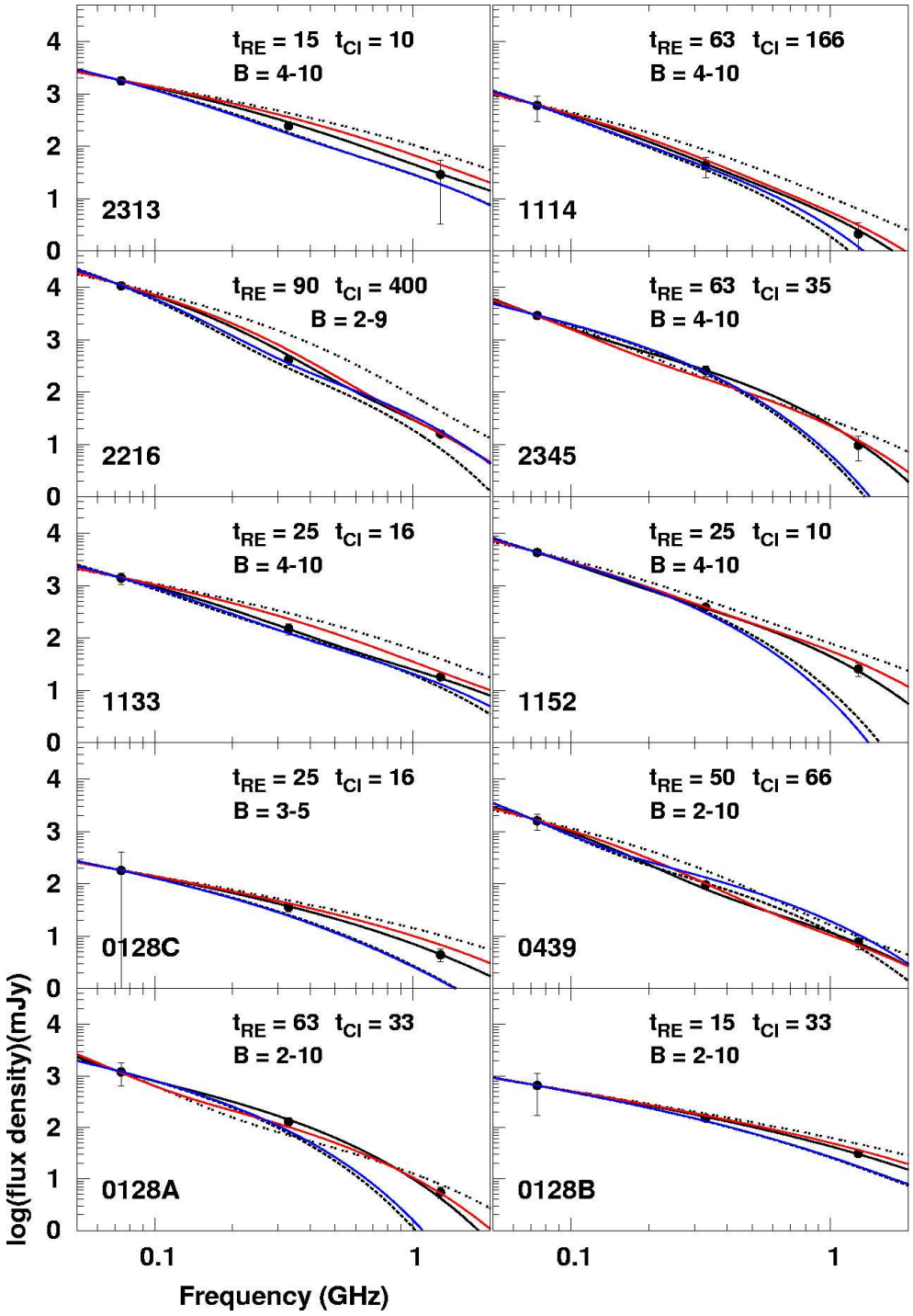

FIGURE 5.5: Spectra of all the sources in Table 5.1. The solid points are observed data along with 3σ error bars. The black solid line is the best fit model spectrum. The best fit parameters are indicated in each panel. The values of t_{CI} and t_{RE} are in million years and of B are in μG. The dotted and the dashed lines are model spectra when t_{RE} is changed by $\pm 30\%$, respectively, with respect to the best fit value. The red and the blue lines are model spectra when t_{CI} is changed by $\pm 50\%$, respectively, with respect to the best fit value. Note that the model spectra for each source are anchored to the respective data value at 74 MHz to fix the y-normalization.

A galaxy B2 1150+37 (SDSS J115236.45+373243.7) at a redshift of 0.229 is also cospatial with the position of 1152. The sources 2216 and 1152 are possibly cluster centre radio galaxies in which the AGNs have turned off (or are not detectable at the sensitivities of observations presented here). Other well known examples of similar relics are A4038 (Chap. 4 in this thesis) and A85 (Slee et al 2001; Young 2004). In recent years, high resolution images from the *Chandra* X-ray Observatory have revealed cavities in the ICM of several clusters (Birzan et al 2009). In some cases these cavities have been found to be filled with radio plasma (for example McNamara 2002). The current understanding is that the jets of radio galaxies deposit plasma in the ICM and this over pressured plasma can expand by doing PdV work, giving rise to cavities in the ICM. The sources 2216 and 1152 could be such relic lobes of radio galaxies which gave rise to cavities in the ICM. In the cases of 2216 and 1152, the ROSAT images do not resolve the X-ray emission to the extent required for the detection of cavities. Arcsec scale resolution X-ray images of the 2216 and the 1152 regions, which are possible using *Chandra*, are required to learn more about the role of these relics in the clusters.

Four of the ten sources are at a redshift of ~ 0.2 (see notes to Table 5.1). For the purposes of the spectral modelling we assumed the current sample of steep-spectrum sources to be at a redshift of 0.2. This is not a serious drawback since the conclusions we draw on the nature of these sources is not sensitive to this assumption. The implied range of radio luminosities (H_o = 75 km s^{-1} Mpc^{-1}) at 1400 MHz is 2-25 $\times$ 10^{23} W Hz^{-1}, close to the value where the distribution of local AGNs peak (Condon 1989, Sadler et al 2002). The linear extents of the steep-spectrum sources are in the range 100 - 400 kpc. The equipartition magnetic fields in these systems are in the range 2 - 10 μG.

Since the shape of the spectrum is a sensitive function of t_{CI}, t_{RE} and B it has been possible to estimate these parameters. It is evident from these plots (Fig. 5.5) that a $\pm$ 30% change from the best-fit value of t_{RE} produces model spectra which are in disagreement with the observed data points and predicts values beyond the 3σ errors of the measurements. So, the errors in the estimates of t_{RE}'s are not more than $\pm$ 30 %. Similar considerations indicate that the errors in the estimates

of t_{CI}'s are not more than $\pm$ 50 %. The mean value of the ratio t_{RE}/t_{CI} for the current sample of sources (Table 5.1) is 1.3. This mean value of t_{RE}/t_{CI} implies that most of the sources discussed here are at a stage when the central engine has been off for as long as it was on. This sample of relics is unique in this respect. This method of selecting sources which have extremely steep spectra has thus resulted in efficient selection of relic radio galaxies.

Examination of the spectral fits for these sources (Fig. 5.5) reveals that the departure from the best fit spectrum when t_{RE} and t_{CI} are varied is more at higher frequencies. This happens since synchrotron and inverse-Compton mechanisms result in higher losses for high energy electrons. This is evident as the steepening of the spectrum at high frequencies. Thus the change in the shape of the spectrum with time is rapid at high frequencies. For the current sample, the highest frequency at which the flux densitites were measures was 1400 MHz. Observations at higher frequencies such as 2 - 10 GHz are required to constrain the timescales t_{RE} and t_{CI} to a much better level.

During the computation of model spectra, it is also possible to keep track of the relative decrease in the radio luminosity as a function of time. This ratio varies in the range 10^2 to 10^4 depending on the value of t_{RE}/t_{CI} for sources in this sample. Since the current radio luminosities of these sources are $\sim 10^{24}$ W Hz^{-1} at 1.4 GHz, the peak radio luminosities of these sources when the AGN was active would have been $\sim 10^{27}$ W Hz^{-1}, brighter than the brightest of the currently known radio galaxies. While the current sample represents sources when the relic phase is comparable to the active phase, the Parma et al (2007) sample represents radio galaxies when the relic phase is an order of magnitude smaller than the active phase.

The detection limits of the surveys at 1400 and 74 MHz are 2 and 500 mJy/beam respectively. The sensitivities of these two surveys are comparable for sources with a spectral index of -1.8. Hence, such steep-spectrum sources detected at 1400 MHz would also be detected at 74 MHz. The peak luminosities of the sources discussed here is $L_{1.4} \sim 10^{27}$ W Hz^{-1}, when they were active. Most of these

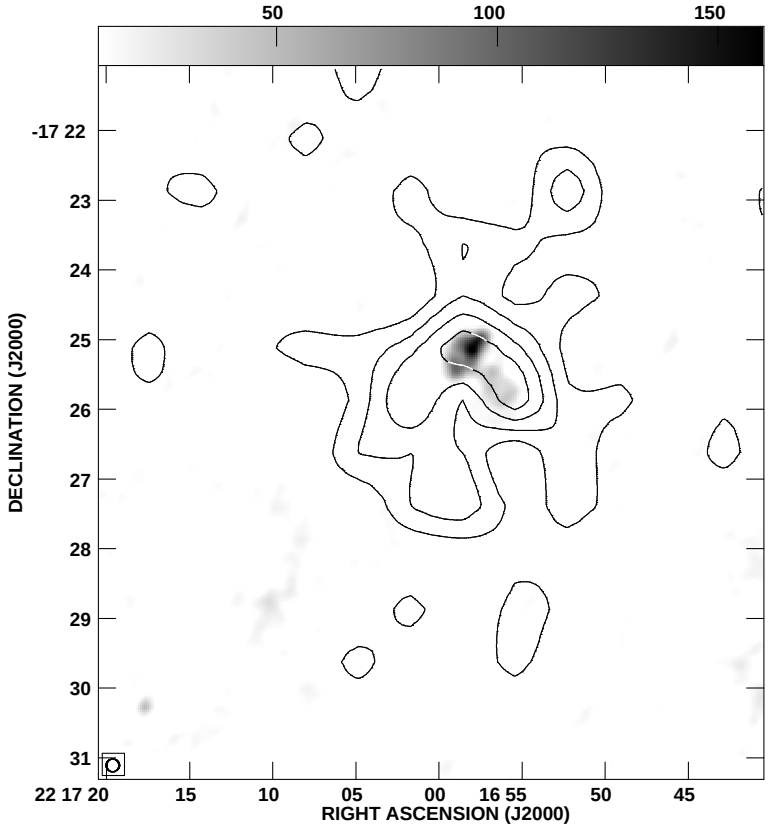

FIGURE 5.6: 2216: GMRT image at 1287 MHz (grey-scale 4 - 60 mJy) on ROSAT (contours).

sources are close to the detection limits of the two surveys used to identify them. However, the luminosity function of currently active AGNs indicates that their number density is about 100 times higher at $L_{1.4} \sim 10^{24}$ W Hz^{-1} (Sadler et al 2002) than at $L_{1.4} \sim 10^{27}$ W Hz^{-1}. At the corresponding ages of the sources reported here, majority of the currently active sources (with $L_{1.4} \sim 10^{24}$ W Hz^{-1}) will remain undetected at the current sensitivity limits of low-frequency surveys. Hence, the dead radio sources discussed here represent just the 'tip of the iceberg' with a large population of such sources to be unearthed from more sensitive low frequency surveys. Such surveys ought to detect a large number of AGNs at different stages of their activities (and hence different spectral indices) and lead to an understanding of their workings and evolution.

5.9 Summary

We have formed a new sample which consists of extended extragalactic radio sources without obvious active galactic nuclei (AGN) in them. These sources with steep spectra ($\alpha <$ -1.8; S $\propto \nu^{\alpha}$) were identified using the 74 (VLSS) and the 1400 MHz (NVSS) surveys and further imaged using the VLA and the GMRT. The radio morphologies of these sources are rather unusual in the sense that no obvious cores and jets are detected in these sources, but, two extended lobes are detected in most. Most of these sources appear to be dead double radio sources. Two of these sources are cospatial with galaxy clusters identified from the ROSAT observations. Neither of the two are giant radio halos or Mpc scale relics at cluster peripheries. Deeeper and higher resolution images in X-rays of these clusters can reveal whether these relics are associated with any cavities in the ICM.

Spectral fits to these relics imply that these sources have been in relic phase as long as these were in the active phase. This property makes this sample of relics the first of its kind. The current data allowed estimates of the relic and the continuous injection timescales to 3σ errors of 30% and 50% respectively. Further higher radio frequency (2-10 GHz) observations of these sources will be useful for constraining the relic and the continuous injection timescales to a better accuracy.

The mean redshift of 4 of the 10 sources reported here is $\sim$ 0.2. At a redshift of 0.2, the linear extents of the sources in the current sample are $\sim$ 250 kpc with their spectral luminosities at 1.4 GHz in the range 2-25 x 10^{23} W Hz^{-1}. The steep spectra of these sources is a result of the cessation of AGN activities in them about 15 – 100 million years ago. Before the cessation of AGN activity, the radio luminosities of these galaxies were $\sim$ 1000 times brighter than their current luminosities and would have been comparable to those of the brightest active radio galaxies detected in the local universe ($L_{1.4} \sim 10^{27}$ W Hz^{-1}). Quantifying the abundance of such a population has important implications to the life cycle of the AGN.

Chapter 6

Summary, Discussion and Future Perspectives

6.1 Summary

In this thesis a variety of diffuse radio halos and relics were considered for a comprehensive multifrequency study. The primary aim of this thesis was to understand the origins of radio halos and relics in clusters of galaxies. Apart from radio halos and relics, a sample of steep spectrum sources were also analysed which turned out to be relic radio galaxies. A summary of the results of the work carried out and conclusions drawn from it are presented below.

6.1.1 Results

- The multifrequency (150, 350, and 1369 MHz) analysis of the radio halo and the relic in A2256 indicates that turbulent reacceleration during mergers may be the mechanism that generated the radio halo and the relic. The flat spectrum NW region of the relic ($\sim$ 200 kpc region, showing polarization upto 45% at 1.4 GHz, CE06) could be the result of the current activity of a shock that passed through the cluster from SE to NW. The low frequency

steepening of the spectra of the diffuse radio emission in A2256 (spectral index maps, Figs. 2.2 and 2.4) is interpreted as the result of superposition of spectra of relativistic electrons accelerated at two epochs. These two epochs are interpreted to be the two mergers that are proposed to have occurred based on X-ray and optical observations (Sun et al 2002; Berrington et al 2003). (Chapter 2; Kale, R. & Dwarakanath, K. S. 2010, ApJ, 718, 939)

- The 150 MHz imaging of A754 resulted in the discovery of a steep spectrum blob of radio emission. Multi-frequency observations suggest that the diffuse radio emission in A754 is patchy and has spectral indices (α) steeper than -1.2 (Table 3.2) ($S \propto \nu^{\alpha}$). The diffuse 'relic' emission that is located along the proposed merger axis in A754 is inconsistent with the model of adiabatically compressed cocoon of radio galaxy. The blobby and steep spectrum diffuse emission and the absence of high temperature thermal gas at those locations (indicators of shocks) in A754 points to the importance of turbulence in the generation of diffuse radio emission. (Chapter 3; Kale, R. & Dwarakanath, K. S. 2009, ApJ, 699, 1883)

- The radio relic near the centre of the cluster A4038 has steep spectrum northern extension (detected at 150, 240 and 606 MHz, Fig. 4.1) and a further NW-Ext suspected at 240 MHz. The spectrum of the relic is consistent with that of a shock compressed cocoon of a radio galaxy. A faint bridge (detected at 150, 240 and 606 MHz) connects the relic to the cD galaxy in A4038 but it is unlikely to be a jet. The possibility of this relic being a non-thermal bubble excavating a cavity in the X-ray emission is explored. However, no cavities in the X-ray images at the location of the relic have been reported (Dunn et al 2005). It is thus possible that the relic is a shock compressed cocoon located at the cluster periphery, but appears close to the cluster centre due to the effects of projection. (Chapter 4; Kale, R. & Dwarakanath, K. S. in prep.)

- The multi-frequency images of the relics in A1664 (150, 330 and 1400 MHz) and A786 (150, 350, 606 and 1464 MHz) were analysed. The relic in A1664

has an integrated spectral index of -1.13 (α_{150}^{1400}) and is at a distance of ∼1.2 Mpc from the cluster centre. Its spectrum is consistent with that of a lurking radio cocoon (age $\sim 4\times10^7$yr). The relic associated with A786 has the largest linear extent of ∼1.6 Mpc and is ∼ 5 Mpc from the centre of the cluster. This could be an example of relativistic plasma generated by acceleration in structure formation shocks (Ensslin et al 1998). The spectrum of the relic is consistent with that of a radio cocoon lurking for $\sim 6 \times 10^7$ yr. (Chapter 4; Kale & Dwarakanath, in prep.)

- The identification of ultra-steep spectrum ($\alpha < -1.8$) sources from the NVSS and the VLSS and their imaging at 330 MHz (VLA) and at 1.4 GHz (GMRT) led to the discovery of double lobed sources with no obvious presence of cores and jets (AGN). These are interpreted to be dead radio galaxies. The model of lurking radio cocoons implies that most of these are sources which have been in the 'relic' phase (AGN off) for more time than the timescale for which the AGN was active. Assuming a mean redshift of 0.2 (4 of the 10 sources are at this redshift) for these sources, the present luminosities ($L_{1.4} \sim 10^{24}$W Hz^{-1}) imply that their luminosities in active phase would have been 10-100 times of those of the brightest AGNs in the local universe. With the detection limits of the VLSS and the NVSS only the brightest among such dead radio sources could be detected. The luminosity function of the currently active AGN indicates that the number density of sources with power $L_{1.4} \sim 10^{24}$ W Hz^{-1} is 100 times higher than with $L_{1.4} \sim 10^{27}$ W Hz^{-1} (Sadler et al 2002) and more sensitive surveys will be able to detect these. These studies will lead to the understanding of the various stages of AGN evolution. (Chapter 5; Dwarakanath, K. S. & Kale, R. 2009, ApJL, 698, 163)

6.1.2 Conclusions

- Sensitive low frequency studies are crucial to discover steep spectrum diffuse components in the ICM. For example, imaging of A754 at 150 MHz resulted in the discovery of a new diffuse component (Chapter 3). At 150, 240 and

606 MHz a steep spectrum northern extension to the relic in A4038 was discovered (Chapter 4). Also at 240 MHz an extention toward the NW is suspected (Chapter 4). This is consistent with more such discoveries in other clusters such as A2255 and A521 (Pizzo et al 2008; Brunetti et al 2008).

- Spectral index maps between more than one pair of frequencies is important to study radio spectra of diffuse emission. In the case of A2256, the property of low frequency steepening of the diffuse emission could not have been discovered otherwise (Chapter 2). It served as an important clue to support the two epochs of merger (and hence of acceleration) proposed from X-ray observations (Chapter 2).

- The radio spectra change rapidly at the higher frequencies due to the nature of synchrotron and inverse-Compton energy losses. To constrain the estimates of the continuous injection and the relic timescales better (errors less than $30\% - 50\%$), spectra of radio halos and relics need to be sampled adequately at frequencies higher than 1.4 GHz (Chapter 3, 4 and 5).

6.2 Discussion

The results of the various observations and their interpretation have been discussed in the respective chapters of this thesis. Some of the issues which draw attention when seeing the results in the larger perspective are discussed below.

In this thesis we studied two dynamically active clusters, A2256 (Chapter 2) and A754 (Chapter 3). Both the clusters are massive ($M \sim 3 \times 10^{14} M_{\odot}$, A754 (Okabe & Umetsu 2008); $M \sim 6 \times 10^{14} M_{\odot}$, A2256, Markevitch & Vikhlinin 1997) and show signatures of ongoing complex mergers (Markevitch et al 2003; Sun et al 2002). However, the nature of diffuse radio emission in these two clusters is very different. The cluster A2256 has a radio halo and a relic, whereas A754 has a blobby radio emission (no well defined radio halo). The spectral indices (α_{150}^{1400}) of the blobs of diffuse emission in A754 are steeper than -1.2 and those of the radio

halo and the relic in A2256 vary over a range -0.7 to -2.5. As compared to A2256, the cluster A754 is deficient in radio emission with flat spectrum. The origin of these differences may be in the difference in the mergers in the two clusters. The amount of turbulence injected in cluster mergers may be different due to different mass ratio of merging clusters and the impact parameter of the merger (Cassano & Brunetti 2005). The time since the mergers have taken place in the clusters A754 and A2256 may be different. Due to the short radiative lifetimes (<Gyr) of radio halos, the nature of the radio emission must be sensitive to the time since the merger occurred. According to the turbulent reacceleration model, the spectral indices of radio halos depend on the energetics of the merger events (eg. Fujita et al 2003; Cassano & Brunetti 2005). A detailed study of the energetics of the mergers in the clusters A754 and A2256 may be the key to the understanding of the difference in the nature of their diffuse radio emission.

There is increasing evidence for mergers playing a major role in the generation of radio halos and relics (Feretti 2006). However, of all the clusters $\sim 40\%$ show signatures of merger (Jones & Forman 1999) but only $\sim 5\%$ of all clusters show presence of radio halos (Giovannini & Feretti 2002). One of the unresolved issue is to establish whether mergers are responsible for the generation of radio halos and relics. From the proposed turbulent reaccelertion model for radio halos, energetics of mergers decide whether a radio halos is generated. It is necessary to carry out deep surveys and obtain stringent limits on presence of diffuse radio emission to resolve the issue about the rare occurrence of radio halos. Recently, a sensitive survey of a complete sample of galaxy clusters with the GMRT (Venturi et al 2008) has led to some progress. A sample of 34 X-ray luminous ($L_x > 5 \times 10^{44}$ergs^{-1}) clusters in the redshift range 0.2-0.4 was observed with the GMRT at 610 MHz by Venturi et al (2008) to search for radio halos and relics. Five clusters contained radio halos and the remaining 29 showed no evidence for diffuse radio emission (Brunetti et al 2007). The stringent limits obtained for the 29 clusters are much below the expected radio power if these clusters were to obey the correlation between radio power and X-ray luminosity (Sec. 1.3.3; Brunetti et al 2007). The clusters with and without radio halos form a bimodal distribution in the $L_x - P_{1.4}$

plane. According to the primary models such as the turbulent reacceleration model, merger injected turbulence which scales with the mass of the clusters plays a major role in the generation of radio halos (Brunetti et al 2007). The clusters undergoing mergers rapidly occupy a place in the $L_x - P_{1.4}$ correlation within $\sim 10^8$ yr and then fade over the same timescale. Thus bimodality in the $L_x - P_{1.4}$ plane is expected from the turbulent reacceleration model. The secondary models on the other hand predict that radio halos can be generated in clusters with magnetic fields and relativistic particles. Since magnetic fields at μG levels are common in clusters (Clarke et al 2001; Govoni & Feretti 2004) and accumulation of relativistic protons on cosmological timescales is expected in all clusters, a scatter in the $L_x - P_{1.4}$ may be expected (eg. Miniati et al 2001; Dolag 2006) but not a bimodal distribution. To reconcile with the observed bimodality, the secondary models would require a significant dissipation of magnetic fields in clusters that do not have radio halo – which is difficult to produce with the current understanding of magnetic fields (Brunetti et al 2007). It was found that all the 5 clusters in the sample that show the presence of diffuse radio emission are undergoing mergers but there is evidence for mergers even among those that do not have radio halos (Venturi et al 2008). This issue needs to be resolved by obtaining constraints on the energetics of cluster mergers in the merging cluster where no radio halo was detected.

The three radio relics in A4038, A1664 and A786 respectively, undertaken for multi-frequency study in this thesis, represent cluster relics in various environments. The relic in A4038 is close to the cluster centre (within 50 kpc), the relic in A1664 is at the periphery of the cluster ($\sim$ 1 Mpc) and the relic in A786 is $\sim$ 5 Mpc from the cluster centre. The size of the relic in A4038 is the smallest among these ($\sim$ 210 kpc) and the relic near A786 is the largest ($\sim$ 1.6 Mpc). The external pressure may be one of the reasons for this. The pressure ($P_{th} \propto nT$, n is the gas density, T is the gas temperature) of the ICM surrounding the relic at cluster cores is 10-100 times that at the peripheries. The morphology and extent of the relic is influenced by the pressure. However it must also be noted that what

one observes is only a projected position of the relic and thus there is ambiguity regarding the external pressure.

The A4038 relic is consistent with a shock compressed plasma and thus smaller in size. The relic in A786 is consistent with a lurking radio cocoon (Chapter 4), but, has also been considered to be due to direct acceleration in structure formation shock (Ensslin et al 1998). The polarization measurements by Harris et al (1993) detected $\sim 20\%$ polarized intensity with the vectors alligned along the longer side of the relic near A786. These indicate the role of shocks. In the scenario of shock accelerated plasma, the location of shock front is expected to have a flat spectral index ($\alpha \sim -0.8$) which progressively steepens in the downstream region of the shock (Sec. 1.5). The images of the relic in A786, with typical resolutions of $\sim 1' - 1.5'$ (FWHM) at 150, 345, 606 and 1464 MHz presented here (Chapter 4) were not useful to make spectral index maps of the relic structures with angular sizes $\sim 1' - 3'$ (the width of the elongated relic). Images with better resolution and sensitivity are required to sample the trends in spectral indices in the elongated relics.

The ultra-steep spectrum sources discussed in Chapter 5 were identified from the VLSS and the NVSS using a spectral index cutoff of -1.8. From the same surveys using a spectral index cutoff of -1.35 and -1.15, van Weeren et al (2010) report the discovery of 23 relic sources out of which one is a giant radio halo and three are suspected to be relics at cluster peripheries (one of it being the source 1133, Table 5.1; Dwarakanath & Kale 2009). The relics analysed in this thesis were found to be consistent with the model of lurking radio cocoons. However due to the uncertainties in the values of magnetic fields and the spectra at frequencies higher than 1.4 GHz, the continuous injection and relic timescales could not be estimated to accuracies better than $30\% - 50\%$. Polarization measurements and high frequency observations are crucial to make progress in understanding these sources.

Overall, a wide variety of radio halo and relic sources are available for study, although the total number of known such sources is $\sim$50. Mergers seem to be a

common aspect of clusters hosting radio halos and relics. It will be of interest to see if a unified model for explaining the radio halos and the peripheral cluster relics based on mergers is possible. Clusters of galaxies that contain radio halos and relics can be segregated in the following way: A. Clusters with only a radio halo and no evidence for peripheral relics (eg. A520, Markevitch et al 2005); B. Clusters with radio halo and a single peripheral relic (eg. Coma, Theirbach et al 2003 and references therein; A521, Brunetti et al 2008); C. Clusters with double peripheral relics and no radio halo (A3667, Rottgering et al 1997; A3376, Bagchi et al 2006); D. Clusters with single peripheral relics and no radio halo (eg. A133, Slee et al 2001) E. Clusters with radio halo and double peripheral relics (RXC J1314.4-2515, Feretti et al 2005). Simulations suggest that double relics at cluster peripheries could be plasma accelerated at outgoing cluster merger shocks (eg. Miniati et al 2001). In such a case the merger would have affected the cluster cores before the shocks developed and reached the cluster peripheries. Under the scenario where the same merger event is responsible for injecting turbulence and leading to radio halo and then leading to the formation of radio relics, the spectral indices of the radio halo and the relics must reveal the chronology of these events. The spectral index of the radio halo is expected to be steeper than that of the freshly accelerated plasma at the outgoing shock. The other possibility is that, if only single/double relics are present, the radio halo has probably faded away. Sensitive low frequency measurements can reveal the radio halo if it were present. A case of such kind is the cluster A521 where only a peripheral relic was discovered at 1.4 GHz and low frequencies revealed the presence of a steep spectrum radio halo (Brunetti et al 2008). Low frequency observations of A3667 and A3376 are required to test whether such steep spectrum radio halos are present at their cores too.

To test the hypothesis of the unified scenario presented above, it is crucial to obtain spectral indices of radio halos and relics and to carry out sensitive low frequency observations. Also for a unified explanation for radio halos and relics as suggested above, support from the simulations is required. Simulations of cluster mergers have predicted the presence of shocks and turbulence in cluster cores

(Sec. 1.3.3). However to understand the observed non-thermal components of the ICM, simulations need to consider acceleration, transport and interactions of non-thermal energetic particles and amplification process of magnetic fields (see review by Dolag et al 2008).

6.3 Future Perspectives

The main objective of further observations will be to test the current theories proposed for the origin of the radio halos and relics in galaxy clusters. Some open questions that need to be addressed are : Can secondary models be ruled out? Do all clusters have diffuse radio halo sources? Are radio halos and relics found only in merging clusters of galaxies? What are the physical processes that lead to the occurrence of radio halos and relics in some and not in all merging clusters? Are the sensitivities of current instruments the only reason for non-detection of such sources in merging clusters? What is the structure of magnetic fields in clusters of galaxies?

The radio telescopes that are planned for the future (such as the LOFAR, LWA and SKA) will be able to address many of these issues. The Low Frequency Array (LOFAR) is a radio telescope planned to make observations in the frequency ranges of 30-80 MHz and 110-240 MHz with baselines spanning the range of 100m -1500 km (Beck 2007). LOFAR will be sensitive to weak magnetic fields around galaxies and in galaxy clusters and possibly in the intergalactic medium (Beck 2007). In an integration time of 1 hr and an effective bandwidth of 3.57 MHz, LOFAR is expected to reach sensitivities $\sim 0.41 - 0.74$ mJy beam^{-1}(beam FWHM $\sim 5 - 40$ arcsec) at 120 MHz with 20-36 stations operational (LOFAR-ASTRON-MEM-251). The Long Wavelength Array (LWA) is planned to operate in the frequency range of 10-88 MHz and will have baselines over the range of 0.1-400 km. The LWA will be able to make images with sensitivities of 0.5 - 1 mJy beam^{-1}over the frequency range of 80- 20 MHz with resolutions $\sim 2'' - 15''$. The Square Kilometre Array (SKA) is an international project planned over the next decade. This will be

a telescope that will have a collecting area of one square kilometre and will operate over a frequency range of 0.3-20 GHz with a resolution of $\sim 1''$(at 1.4 GHz) (Beck 2007). Cosmic magnetism is one of the key science projects of LOFAR, LWA and SKA.

The typical surface brightness of the known radio halos and relics at 120 MHz is $\sim$ 10 mJy beam^{-1}(beam FWHM $\sim 60''$). The extensive surveys with resolutions $\sim 5'' - 60''$, at frequencies $\sim$ 120 MHz and <mJy level sensitivities planned using the LOFAR, LWA and SKA will enormously increase the rate of detection of radio halos and relics. According to models (eg. turbulent reacceleration model, Cassano et al (2006, 2008)), low frequency surveys with <mJy sensitivities at 120-150 MHz frequencies will be able to detect more than 10 times the number of radio halos detected at 1.4 GHz. In an all sky survey planned at 120 MHz, with the LOFAR, with a sensitivity of $\sim$ 0.1 mJy beam^{-1}, 350 radio halos ($z < 0.6$) are expected to be detected (Cassano et al 2010). In the Million Source Shallow Survey (expected to be carried out over 2010-2011 with the LOFAR) with a sensitivity $\sim$ 0.5 mJy beam^{-1}at 150 MHz, 100 radio halos are expected to be detected (Cassano et al 2010). Feretti et al (2004) estimate that with 1 hour integration time at 1.4 GHz, 50% of SKA collecting area will allow detection of radio halos and relics having total flux down to 1mJy at any redshift and down to 0.1 mJy at high redshifts. A statistical sample of radio halos and relics will be available to address the issues regarding the occurrence of radio halos and relics. It will be possible to test the $L_x - P_{1.4}$ correlation down to the lowest X-ray luminosities ($L_x \sim 10^{43}$ergs^{-1}), study the redshift evolution of radio halos and relics and the relation between the non-thermal and thermal components of the ICM.

The radio halos and relics in clusters of galaxies open the avenues to learn about the large scale magnetic fields in galaxy clusters. Sensitive measurements of polarized emission and rotation measures, possible with the LOFAR and SKA, will lead to a much better understanding of the magnetic fields in the galaxy clusters and intergalactic medium (Ferrari et al 2008).

Diffuse extended extra-galactic sources such as the radio halos and relics and relic radio galaxies contribute as foregrounds to the signal from the Epoch of Reionization (EoR). Better knowledge of the statistics of such sources and well-constrained modelling will be required for the detection of the EoR signal (Jelic et al 2008).

Apart from low frequencies, observations at higher frequencies are also going to be crucial for radio halos and relics. The radio spectra of radio halos and relics are more sensitive to changes in model parameters at higher frequencies. With the currently available facilities, the extents and the steep spectra of radio halos and relics have been the major hurdles in obtaining images at higher frequencies (> 1.4 GHz). With the EVLA becoming operational, some progress in understanding the high frequency spectra of the radio halos and relics can be made. Eventually with SKA, it will be possible to study radio halos and relics over the frequency range of 0.3 - 20 GHz.

Appendix A

Radio Telescopes

A brief introduction to each of the radio telescopes that were used for the study in this thesis is given below.

The Giant Metrewave Radio Telescope (GMRT): The GMRT consists of 30 dish antennas, each of diameter 45 m (Fig. A.1, left) arranged approximately in a shape of 'Y'. It provides baseline lengths in the range 100 m to 25 km. Fourteen of the 30 dishes are in a compact configuration over an area of 1 km^2 and the rest form the 3 'arms' of the 'Y' shape (Fig. A.1, right). This, often called the 'hybrid configuration', allows a good $u, v-$coverage (crucial for imaging extended emission) at short as well as long baselines. The GMRT provides observing bands of 8-32 MHz of bandwidth around each of 150, 235, 610 and 1400 MHz. A facility of simultaneous observation at 235 and 610 MHz is also available. The band around 1400 MHz spans from 1280-1700 MHz. Observations using all the bands of the GMRT have been carried out for this thesis.

The Westerbork Synthesis Radio Telescope (WSRT): The WSRT consists of 14 dish antennas each of 25 m diameter arranged along the east-west direction (Fig. A.2, left). It provides baseline lengths ranging from 36 m to 14 km. Observations at 350 MHz were carried out with the WSRT for this thesis.

The Very Large Array (VLA): The VLA consists of 27 dish antennas, each of 25 m diameter arranged in a perfect 'Y' shape (Fig. A.2, right). The VLA antennas are placed on rails and are moved to change the configuration of the

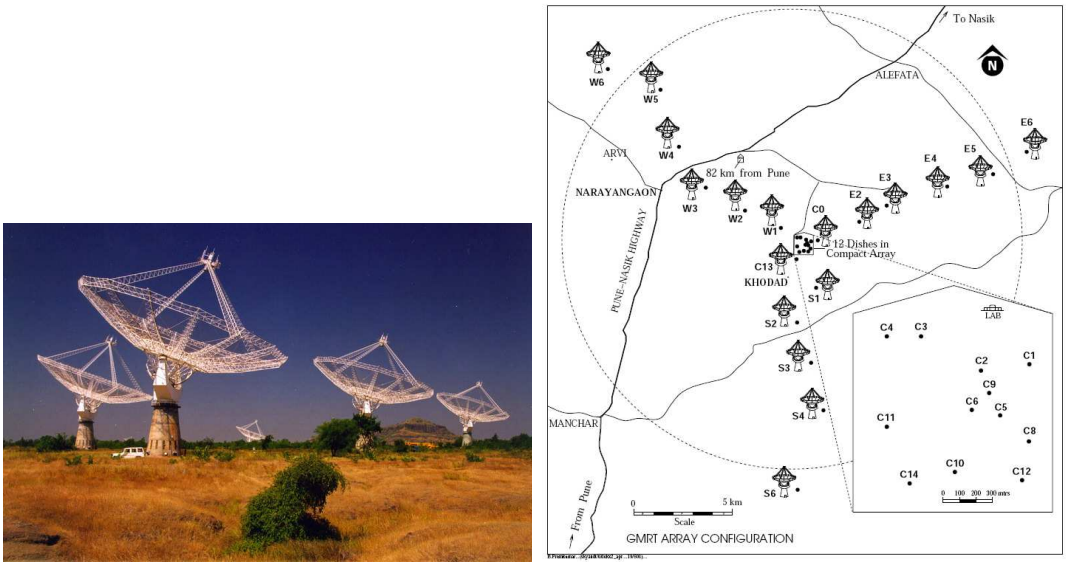

FIGURE A.1: GMRT antennas (left). All together 30 such dish antennas form the complete GMRT array, schematically shown in the right panel. (Image credit: TIFR)

telescope. The configurations are named as A, B, C, and D in which the longest baselines are 36, 13, 3 and 1 km, respectively. Observations at 330 MHz in the A configuration and at 1400 MHz in the D configuration form part of this thesis.

FIGURE A.2: View of the WSRT (left) and of the VLA in D configuration (right). (Image credits: ASTRON (left) and NRAO (right))

Appendix B

GMRT 150 and 610 MHz Images of the A2256 field

A2256 at 150 MHz

The image of A2256 field at 150 MHz using the GMRT covering an area of $\sim 4 \times 4$ deg^2 of the sky is presented in Fig. B.1. Uniform weights were used for the visibilities to produce an image with a resolution of $21'' \times 21''$. The rms is 2.6 mJybeam^{-1} near the centre of the field. The grey scale is displayed over a range of 0.003 - 0.05 Jy. The peak flux density in this field is 4.8 Jybeam^{-1}. Primary beam correction has not been applied to the image. The radio halo and the relic region was not detected in this image.

A2256 at 610 MHz

Central portion (same as in Fig. 2.1) of the 610 MHz image is presented in Fig. B.2 to show the compact radio sources in the A2256 field. Portions of the diffuse relic, G and H were detected at 610 MHz and are marked in the image.

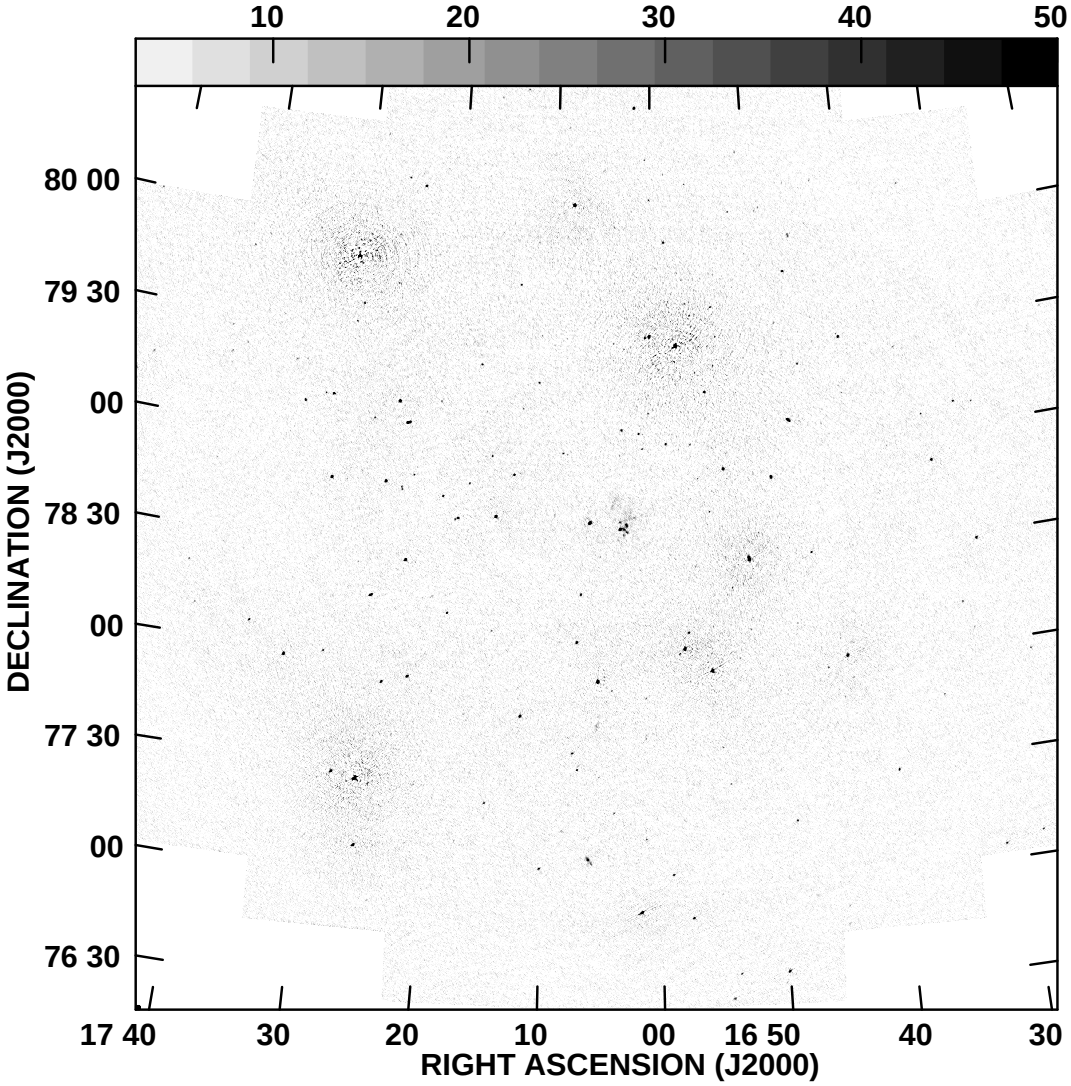

FIGURE B.1: The A2256 field at 150 MHz. Synthesized beam is $21'' \times 21''$ and the rms is 2.6 mJybeam^{-1} (central region). Grey-scale is displayed over a range 0.003 - 0.05 Jy.

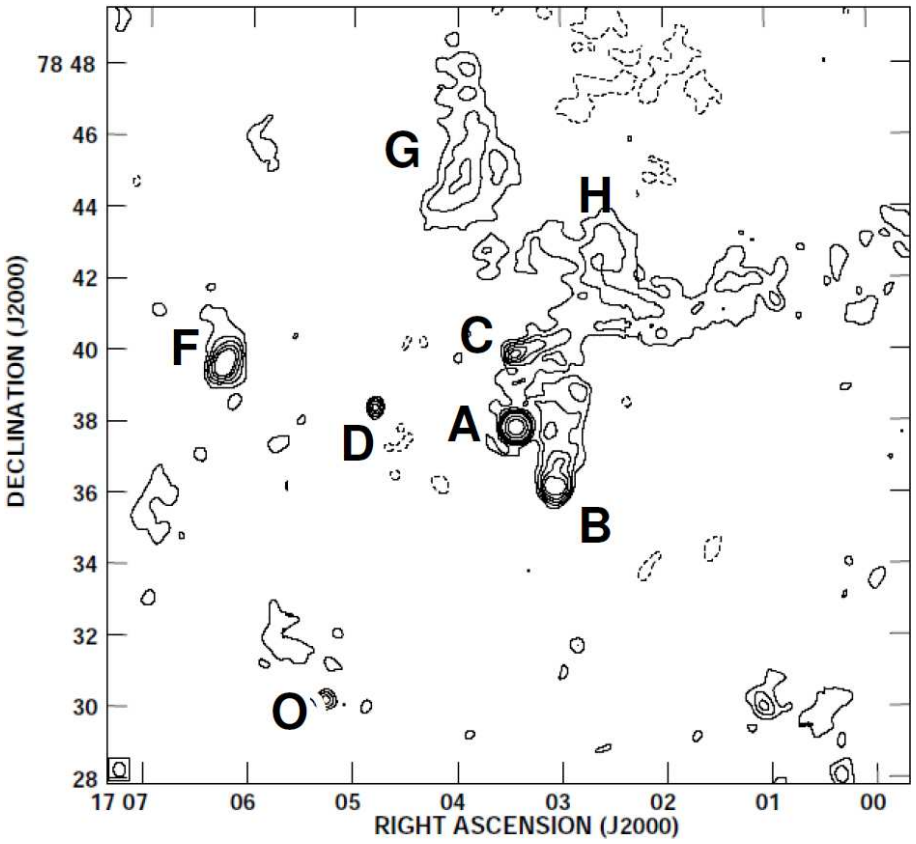

FIGURE B.2: A2256: Central region of the GMRT 610 MHz image with a synthesized beam of $23'' \times 22''$ (PA 0.9°) and an rms of 0.8 mJy beam^{-1} . Contours are at -2.4, 2.4, 4.8, 8, 12, 16, 40, 80 mJy beam^{-1}. The labels A, B, C, D, F, O, G and H for the radio sources are according to the convention in Bridle et al (1979) and R94. Compare this image with the Fig. 2.1 to locate the radio sources relative to the diffuse radio halo and the relic. The source B is a bent double radio galaxy and C is the head-tail radio galaxy in A2256 (Miller et al 2003). Portions of diffuse relic, G + H that were detected at 610 MHz are also marked. The central diffuse radio halo emission was not detected due to insufficient uv-coverage at short baselines.

Appendix C

AIPS 'PBCOR' values for the WSRT

The task 'PBCOR' in AIPS is used to apply primary beam gain correction to the images. The procedure followed to obtain the values to be used in the task 'PBCOR' of AIPS for primary beam correction for the WSRT is described here. The primary beam of a radio telescope antenna can be approximated by a polynomial. In AIPS the polynomial is given by

$$\begin{aligned} F(X) &= 1.0 + X\frac{PBPARM(3)}{(10^3)} + X^2\frac{PBPARM(4)}{(10^7)} + \\ & X^3\frac{PBPARM(5)}{(10^{10})} + X^4\frac{PBPARM(6)}{(10^{13})} + \\ & X^5\frac{PBPARM(7)}{(10^{16})} \end{aligned} \tag{C.1}$$

where $X = (r_{am}\nu_{GHz})^2$ where r_{am} is the distance from the pointing center in arcminutes and ν_{GHz} is the frequency in units of GHz. The set of parameters $PBPARM(3-7)$ determine the primary beam specific to an antenna. Our aim is to determine these parameters for the WSRT.

The primary beam of the WSRT can be represented by

$$f(x) = cos^6(c\nu_{GHz}r_{rad}) = cos^6(x) \tag{C.2}$$

where r_{rad} is the distance from the pointing center in radians, ν_{GHz} is the observing frequency in GHz and the constant c= 68 is, to first order, wavelength independent at GHz frequencies (declining to $c = 66$ at 325 MHz and $c = 63$ at 4995 MHz) (Sec. 5.7 of the WSRT Observing Guide provided by ASTRON[1]). Let $x = c\nu_{GHz}r_{rad}$. To find the parameters $PBPARM(3-7)$ in A.1, f(x) must be expressed as a polynomial in terms of X.

We have,

$$\begin{aligned} x &= c\nu_{GHz}r_{rad} \\ &= 2.9 \times 10^{-4} c\nu_{GHz}r_{am} \end{aligned} \tag{C.3}$$

where r_{am} is the distance from the pointing centre in arcminutes. At 325 MHz, $c = 66$ and therefore,

$$x = 0.019\nu_{GHz}r_{am}$$

and using the definition of X, we have,

$$x^2 = 3.61 \times 10^{-4} X \tag{C.4}$$

The function $cos^6(x)$ can be approximated by a polynomial and depending on the required accuracy, the terms upto a certain order can be retained. In the case of the task 'PBPARM', the polynomial has terms upto X^5 which means terms upto x^{10} (see C.4) need to be retained. It will be checked whether this is a good representation of the primary beam over the region of interest in the image. Using *MATHEMATICA*, $cos^6(x)$ was approximated upto an order x^{10},

$$cos^6(x) = 1 - 3x^2 + 4x^4 - \frac{47}{15}x^6 + \frac{169}{105}x^8 - \frac{2717}{4725}x^{10} + \mathcal{O}(x^{11}). \tag{C.5}$$

Comparing C.5 with C.1 and using the relation in C.4, the parameters for the task 'PBPARM' were obtained. Those are:

$$\begin{aligned} PBPARM(3) &= -1.083 \\ PBPARM(4) &= 5.212 \\ PBPARM(5) &= -1.474 \\ PBPARM(6) &= 0.273 \\ PBPARM(7) &= -0.035 \end{aligned}$$

Using these parameters, it was found that the error on the estimate of the gain of the primary beam of the WSRT is less than a few percent upto a distance of $30'$ from the pointing centre. This was checked by comparing the function $cos^6(x)$ and the polynomial approximation of it.

The values for these parameters for other frequency bands of the WSRT can be obtained by substitution of ν_{GHz} and the corresponding c in Eq. C.3 and then following the same procedure of comparing C.5 to C.1.

[1]

[1] ASTRON url: http://www.astron.nl

Appendix D

GMRT 240 MHz image of A4038 and 606 MHz image of A786

A larger field of view around the relic in A4038 is presented in Fig. D.1 at 240 MHz. High resolution image at 606 MHz of the relic near A786 is presented in Fig. D.2.

A4038 at 240 MHz

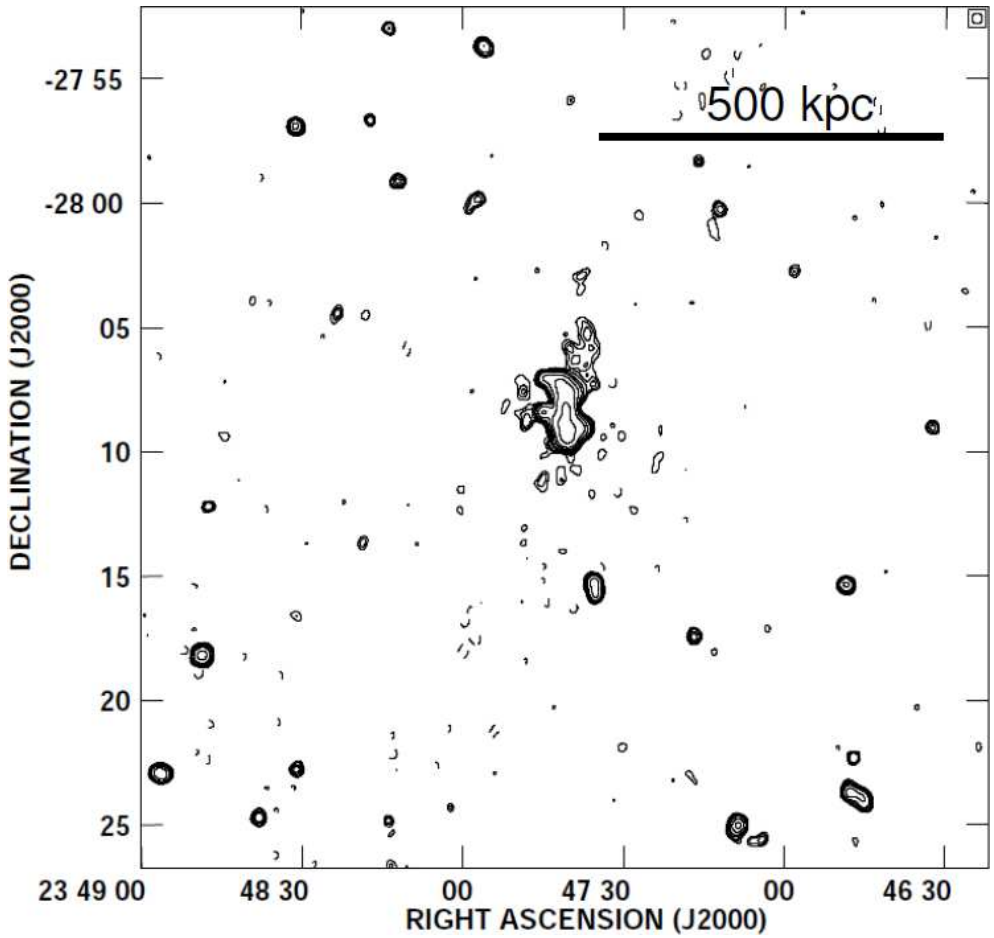

FIGURE D.1: The A4038 field at 240 MHz. Synthesized beam is $25'' \times 25''$ and the contours are at -4.5, 4.5, 6.0, 7.5, 12.0, 18.0, 36.0, 72.0, 144.0, 231.0 mJybeam^{-1}.

A786 at 606 MHz

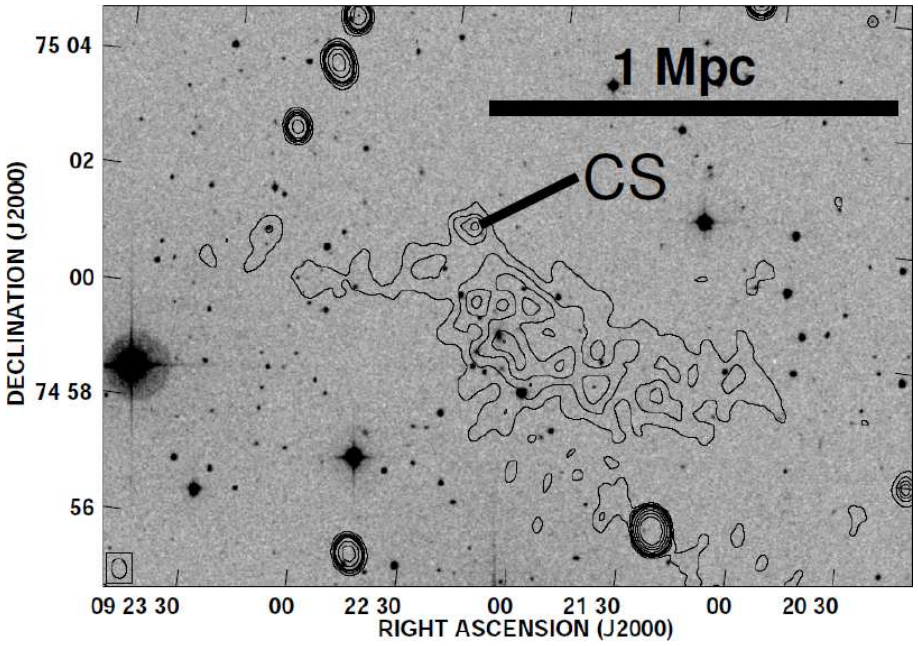

FIGURE D.2: A high resolution image of the relic near A786 at 606 MHz. The location of unresolved sources is marked as 'CS'. Contour levels are at -1.05, 1.05, 2.10, 3.15, 4.20, 5.25, 10.50, 21.0, 42.0, 84.0 mJy beam^{-1}(synthesized beam= $20'' \times 16''$, P.A. = 14.66°).

Bibliography

Abell, G. O. 1958, ApJS, 3, 211

Alexander, P. & Leahy, J. P. 1987, MNRAS, 225, 1

Allen, S. W., Fabian, A. C., Edge, A. C., Bohringer, H., & White, D. A. 1995, MNRAS, 275, 741

Bacchi, M., Feretti, L., Giovannini, G., & Govoni, F. 2003, A&A, 400, 465

Bagchi, J., Ensslin, T. A., Miniati, F., Stalin, C. S., Singh, M., Raychaudhury & S., Humeshkar, N. B. 2002, New Astr., 7, 249

Bagchi, J., Durret, F., Neto, G. B. L. & Paul, S. 2006, Science, 314, 791

Baldwin, J. E., Scott, P. F. 1973, MNRAS, 165, 259.

Beck , R. 2005, Adv. in Rad. Sci., 5, 399

Berrington, R. C., Lugger, P. M., & Cohn, H. N. 2002, AJ, 123, 2261

Birzan, L., Rafferty, D. A., McNamara, B. R., Nulsen, P. E. J. & Wise, M. W. 2009, Proceedings of "The Monsters Fiery Breath", Eds. Heinz, S. & Wilcots, E.

Blandford, R., & Eichler, D. 1987, Phy. Rep., 154, 1

Blasi, P., & Colafrancesco, S. 1999, Astropart. Phys., 12, 169

Blundell, K. M., Rawlings, S., Willot, C. J., Kassim, N. E. & Perley, R. 2002, New Astr. Rev., 46, 75

Bonafede, A., Feretti, L., Giovannini, G., Govoni, F., Murgia, M., Taylor, G. B., Ebeling, H., Allen, S., Gentile, G., & Pihlstrm, Y. 2009a, A&A, 503, 707

Bonafede, A., Giovannini, G., Feretti, L., Govoni, F., & Murgia, M. 2009b, A&A, 494, 429

Bourdin, H. & Mazzotta, P. 2008, A&A, 479, 307

Branson, N. J. B. A. 1967, MNRAS, 135, 149

Brentjens, M. A. 2008, A&A, 489, 69

Bridle, A. H. & Fomalont, E. B. 1976, A&A, 52, 107

Bridle, A. H., Fomalont, E. B., Miley, G. K., & Valentijn, E. A. 1979, A&A, 80, 201

Briel, U. G. & Henry, J. P. 1994, Nature, 372, 439

Briel, U. G., Henry, J. P., Schwarz, R. A., Bohringer, H., Ebeling, H., Edge, A. C., Hartner, G. D., Schindler, S., Trumper, J., & Voges, W. 1991, A&A, 246, 10

Brown, S. & Rudnick, L. 2009, AJ, 137, 3158

Brunetti, G., Venturi, T., Dallacasa, D., Cassano, R., Dolag, K., Giacintucci, S. & Setti, G. 2007, ApJL, 670, 5

Brunetti, G., Setti, G., Feretti, L., & Giovannini, G. 2001, MNRAS, 320, 365

Brunetti, G. 2003, Matter and Energy in Clusters of Galaxies, ASP Conference Proceedings, 301, ed. Stuart B. & Chorng-Yuan H., Astronomical Society of the Pacific San Francisco, 349

Brunetti, G., Blasi, P., Cassano, R., & Gabici, S. 2004, MNRAS, 350, 1174

Brunetti, G., Giacintucci, S., Cassano, R., Lane, W., Dallacasa, D., Venturi, T., Kassim, N. E., Setti, G., Cotton, W. D. & Markevitch, M. 2008, Nature, 455, 944

Brunetti, G., & Lazarian, A. 2007, MNRAS, 378, 245

Buote , D. 2002, Merging Processes in Galaxy Clusters, ed. Feretti, L., Gioia, I. M., & Giovannini, G. (Kluwer), 79

Burenin, R. A., Vikhlinin, A., Hornstrup, A., Ebeling, H., Quintana, H. & Meshcheryakov, A. 2007, ApJS, 172, 561

Burns, J. O., Sulkanen, M. E., Gisler, Galen R., & Perley, Rick A. 1992, ApJL, 388, 49

Carilli,, C. L., & Taylor, G. B. 2002 ARA&A, 40, 319

Cassano, R., Brunetti, G. & Setti, G. 2006, MNRAS, 369, 1577

Cassano, R., Brunetti, G., Venturi, T., Setti, G., Dallacasa, D., Giacintucci, S., & Bardelli, S. 2008, A&A, 480, 687

Cassano, R., & Brunetti, G. 2005, MNRAS, 357, 1313

Cassano, R., Brunetti, G., Rttgering, H. J. A. & Brggen, M. 2010, A&A, 509, 68

Churazov, E., Forman, W., Jones, C., Sunyaev, R. A. & Bohringer, H. 2004, MNRAS, 347, 29

Clarke, T. E. & Ensslin, T. 2006, AJ, 131, 2900

Cohen, A. S., Clarke, T. E., Feretti, L., Kassim, N. E. 2005, ApJL, 620, 5.

Cohen, A. S., Lane, W. M., Cotton, W. D., Kassim, N. E., Lazio, T. J. W., Perley, R. A., Condon, J. J., & Erickson, W. C. 2007, AJ, 134, 3, 1245

Cohen, A. S., Lane, W. M., Kassim, N. E., Lazio, T. J. W., Cotton, W. D., Perley, R. A., Condon, J. J., Erickson, W. C. 2006, AN, 327, 262.

Cohen, A. S., Rottgering, H. J. A., Jarvis, M. J., Kassim, N. E., Lazio, T. J. W. 2004, ApJSS, 150, 417.

Colafrancesco, S. & Blasi, P. 1998, Astropart. Phy., 9, 227

Condon, J. J. 1989, ApJ, 338, 13.

Condon, J. J., Cotton, W. D., Greisen, E. W., Yin, Q. F., Perley, R. A., Taylor, G. B., & Broderick, J. J. 1998, AJ, 115, 1693

Cruz, M. J., Jarvis, M. J., Blundell, K. M., Rawlings, S., Croft, S., Klockner, H., McLure, R. J., Simpson, C., Targett, T. A., Willott, C. J. 2006, MNRAS, 373, 1531.

de Grandi, S., Bhringer, H., Guzzo, L., Molendi, S., Chincarini, G., Collins, C., Cruddace, R., Neumann, D., Schindler, S., Schuecker, P., & Voges, W. 1999, ApJ, 514, 148

Deiss, B. M., Reich, W., Lesch, H., & Wielebinski, R. 1997, A&A, 321, 55

Delain, K. M.; Rudnick, L. 2006, AN, 327, 561

Dennison, B. 1980, ApJ, 239, 93

Dewdney, P. E., Costain, C. H., McHardy, I., Willis, A. G., Harris, D. E. & Stern, C. P. 1991, ApJS, 76, 1055

Dolag, K. 2006, AN, 327, 575

Dolag, K., & Ensslin, T. A. 2000, A&A, 362, 151

Dolag, K., Vazza, F., Brunetti, G., & Tormen, G. 2005, MNRAS, 364, 753

Dolag, K., Bykov, A. M. & Diaferio, A. 2008, SSRv, 134, 311

Dunn, R. J. H., Fabian, A. C., & Taylor, G. B. 2005, MNRAS, 364, 1343

Dwarakanath, K. S. & Kale, R. 2009, ApJ Letters, 698, 163

Ebeling, H., Voges, W., Bohringer, H., Edge, A. C., Huchra, J. P., & Briel, U. G. 1996, MNRAS, 281, 799

Ensslin, T. A., Biermann, P. L., Klein, U., & Kohle, S. 1998, A&A, 332, 395

Ensslin, T. A. & Bruggen, M. 2002, MNRAS, 331, 1011

Ensslin, T. A., & Gopal-Krishna 2001, A&A, 366, 26

Ensslin, T. A., Biermann, P. L., Kronberg, P. P., & Wu, X.-P. 1997, ApJ, 477, 560

Ensslin, T. A., Lieu, R., Biermann, P. L. 1999, A&A, 344, 409

Fabricant, D., Beers, T. C., Geller, M. J., Gorenstein, P., Huchra, J. P., & Kurtz,

M. J. 1986, ApJ, 308, 530

Fabricant, D. G., Kent, S. M., & Kurtz, M. J. 1989, ApJ, 336, 77

Feretti, L. 2006, Proceedings of the XLIst Rencontres de Moriond, XXVIth Astrophysics Moriond Meeting: "From dark halos to light", ed. Tresse, L., Maurogordato, S., & J. Tran Thanh Van

Feretti, L., Boehringer, H., Giovannini, G., & Neumann, D. 1997, A&A, 317, 432

Feretti, L. & Giovannini, G. 1996, IAU Symp. 175, Extragalactic radio sources, ed. R. D. Ekers, C. Fanti, & L. Padrielli (Dordrecht: Kluwer), 333

Feretti, L., Schuecker, P., Bohringer, H., Govoni, F. & Giovannini, G. 2005, A&A, 444, 157

Feretti , L. & Giovannini, G. 2007, astro-ph/0703494

Feretti, L., Fusco-Femiano, R., Giovannini, G. & Govoni, F. 2001, A&A, 373, 106

Feretti, L., Orru, E., Brunetti, G., Giovannini, G., Kassim, N., & Setti, G. 2004, A&A, 423, 111

Ferrari, C., Govoni, F., Schindler, S., Bykov, A. M. & Rephaeli, Y. 2008, SSRv, 134, 93

Finoguenov, A., Bohringer, H., & Zhang, Y.-Y. 2005, A&A, 442, 827

Fujita, Y., Takizawa, M. & Sarazin, C. L. 2003, AJ, 584, 190

Fusco-Femiano, R., Orlandini, M., Brunetti, G., Feretti, L., Giovannini, G., Grandi, P., & Setti, G. 2004, ApJL, 602, 73

Fusco-Femiano, R., Orlandini, M., De Grandi, S., Molendi, S., Feretti, L., Giovannini, G., Bacchi, M., Govoni, F. 2003, A&A, 398, 441

Fusco-Femiano, R., Landi, R., & Orlandini, M. 2005, ApJL, 624, 69

Fusco-Femiano, R., Landi, R., & Orlandini, M. 2007, ApJL, 654, 9

Gabici, S., & Blasi, P. 2003, ApJ, 583, 695

Gastaldello, F. & Molendi, S. 2004, ApJ, 600, 670

Giacintucci, S., Venturi, T., Brunetti, G., Bardelli, S., Dallacasa, D., Ettori, S., Finoguenov, A., Rao, A. P., & Zucca, E 2005, A&A, 440, 867

Giacintucci, S., Venturi, T., Macario, G., Dallacasa, D., Brunetti, G., Markevitch, M., Cassano, R., Bardelli, S., & Athreya, R. 2008, A&A, 486, 347

Girardi, M., & Biviano, A. 2002, ASSL, 272, 39

Giovannini, G., & Feretti, L. 2000, NewAstr, 5, 335

Giovannini, G. & Feretti, L. 2002, Merging Processes in Galaxy Clusters, ed. L. Feretti, I.M. Gioia, G. Giovannini, ASSL (Dordrecht: Kluwer), 272, 197

Giovannini, G., Feretti, L., Venturi, T., Kim, K. -T., & Kronberg, P. P. 1993, ApJ, 406, 399

Giovannini, G., Tordi, M., & Feretti, L. 1999, New Astr. Rev., 4, 141

Giovannini, G., Bonafede, A., Feretti, L., Govoni, F., Murgia, M., Ferrari, F., & Monti, G. 2009, A&A, 507, 1257

Giovannini, G., Feretti, L., Venturi, T., Kim, K.-T. & Kronberg, P. P. 1991, Clusters and Superclusters of Galaxies, eds. Colless, M. M., Babul, A., Edge, A. C., Johnstone, R. M., & Raychaudhury, S., 71 (Cambridge)

Goldshmidt, O., Rephaeli, Y. 1994, ApJ, 431, 586.

Gopal-Krishna, Ledoux, C., Melnick, J., Giraud, E., Kulkarni, V., Altieri, B. 2005, A&A, 436, 457.

Govoni, F. & Feretti, L. 2004, IJMPD, 13, 1549

Govoni, F., Feretti, L., Giovannini, G., Bohhringer, H., Reiprich, T. H., & Murgia, M. 2001, A&A, 376, 803

Govoni, F., Markevitch, M., Vikhlinin, A., VanSpeybroeck, L., Feretti, L., & Giovannini, G. 2004, ApJ, 605, 695

Govoni, F., Murgia, M., Feretti, L., Giovannini, G., Dallacasa, D., & Taylor, G. B. 2005, A&A, 430, 5

Harris, D. E.; Kapahi, V. K.; Ekers, R. D. 1980, A&AS, 39, 215

Harris, D. E., Pineda, F. J., Delvaille, J. P., Schnopper, H. W., Costain, C. H., & Strom, R. G. 1980, A&A, 90, 283

Harris, D. E., Stern, C. P., Willis, A. G. & Dewdney, P. E. 1993, AJ, 105, 769

Henriksen, M. J. & Markevitch, M. L. 1996, ApJ, 466, 79

Henry, J. P. & Briel, U. G., 1995, ApJ, 443, 9

Henry, J. P., Finoguenov, A., & Briel, U. G. 2004, ApJ, 615, 181

Hoeft, M & Bruggen, M. 2007, MNRAS, 375, 77

Jaffe, W. J., & Perola, G. C. 1973, A&A, 26, 423

Jaffe, W. J. 1977, ApJ, 212, 1

Jarvis, M. J., Cruz, M. J., Cohen, A. S., Rottgering, H. J. A., Kassim, N. E. 2004, MNRAS, 355, 20.

Jelic, V., Zaroubi, S., Labropoulos, P., Thomas, R. M., Bernardi, G., Brentjens, M. A., de Bruyn, A. G., Ciardi, B., Harker, G., Koopmans, L. V. E. Pandey, V. N., Schaye, J., & Yatawatta, S. 2008, MNRAS 389, 1319

Jeltema, Tesla E., & Profumo, S. 2010, arXiv1006.1648

Jones, C. & Forman, W. 1999, ApJ, 511, 65

Kaiser, C. R. & Alexander, P. 1997, MNRAS, 286, 215

Kaiser, C. R. & Cotter, G. 2002, MNRAS, 336, 649.

Kale. R. & Dwarakanath, K. S. 2010, ApJ, 718, 939

Kale, R. & Dwarakanath, K. S. 2009, ApJ, 699, 1883

Kapferer, W., Ferrari, C., Domainko, W., Mair, M., Kronberger, T., Schindler, S., Kimeswenger, S., van Kampen, E., Breitschwerdt, D., & Ruffert, M. 2006, A&A, 447, 827

Kardashev, N. S. 1962, SvA, 6, 317.

Kassim, N. E., Clarke, T. E., Ensslin, T. A., Cohen, A. S., & Neumann, D. M. 2001, ApJ, 559, 785

Kim, K. -T. 1999, JKAS, 32,75

Kim, K.-T., Kronberg, P. P. & Tribble, P. C. 1991, ApJ, 379, 80

Kim, K.-T. 1990, Nuovo Cimento B, 105, 845

Kirkpatrick, C. C., McNamara, B. R., Rafferty, D. A., Nulsen, P. E. J., Brzan, L., Kazemzadeh, F., Wise, M. W., Gitti, M., & Cavagnolo, K. W. 2009, ApJ, 697, 867

Klamer, I. J., Ekers, R. D., Bryant, J. J., Hunstead, R. W., Sadler, E. M., & De Breuck, C. 2006, MNRAS, 371, 852.

Komissarov, S. S. & Gubanov, A. G. 1994, A&A, 285, 27.

Kuo, P. -H., Hwang, C. -Y., & Ip, W. -H. 2003, AJ, 594, 732

Liang, H., Hunstead, R. W., Birkinshaw, M., & Andreani, P. 2000, ApJ, 544, 686

Loewenstein, M. 2003, Origin and Evolution of the Elements, Carnegie Observatories Astrophysics Series, eds. McWilliam, A., & Rauch, M., 4, 1 (Cambridge: Cambridge Univ. Press)

Longair, M. S. 1981, High Energy Astrophysics (Cambridge University)

Markevitch, M., Govoni, F., Brunetti, G., & Jerius, D. 2005, ApJ, 627, 733

Markevitch, M., Mazzotta, P., Vikhlinin, A., Burke, D., Butt, Y., David, L., Donnelly, H., Forman, W. R., Harris, D., Kim, D.-W., Virani, S., Vrtilek, J. 2003, ApJ, 586, 19

Markevitch, M. 1998, ApJ,504, 27

Markevitch, M., & Vikhlinin, A. 2001, ApJ, 563, 95

Markevitch, M. & Vikhlinin, A. 1997, ApJ, 491, 467

Markevitch, M., Gonzalez, A. H., David, L., Vikhlinin, A., Murray, S., Forman, W., Jones, C. & Tucker, W. 2002, ApJ, 567, 27

Markevitch, M., Ponman, T. J., Nulsen, P. E. J., Bautz, M. W., Burke, D. J., David, L. P., Davis, D., Donnelly, R. H., Forman, W. R., Jones, C., Kaastra, J., Kellogg, E., Kim, D.-W., Kolodziejczak, J., Mazzotta, P., Pagliaro, A., Patel, S., Van Speybroeck, L., Vikhlinin, A., Vrtilek, J., Wise, M., & Zhao, P. 2000, ApJ, 541, 542

Masson, C. R., & Mayer, C. J. 1978, MNRAS, 185, 607

McNamara, B. R. 2002, The High Energy Universe at Sharp Focus: Chandra Science, ASP Conf. Proc., 262, Ed. Schlegel, E. M. & Vrtilek, S. D. San Francisco: Astronomical Society of the Pacific, 351

Melrose, D. B. 1980, Plasma Astrophysics (Gordon & Breach)

Miller, N. A., Owen, F. N., & Hill, J. M. 2003, AJ, 125, 2393

Mills, B. Y., Hunstead, R. W., & Skellern, D. J. 1978, MNRAS, 185, 51

Miniati, F., Ryu, D., Kang, H., Jones, T. W., Cen, R.,& Ostriker, J. 2000, ApJ, 542, 608

Miniati, F., Ryu, D., Kang, H., & Jones, T. W. 2001, ApJ, 559, 59

Moffet, A. T. 1975, Galaxies and the Universe, eds. Sandage A., Sandage, M. & Kristian, J., Stars and Stellar Systems, 9, 211 (University of Chicago Press: Chicago, IL USA)

Okabe, N. & Umetsu, K. 2008, Publ. Astron. Soc. Japan, 60, 345

Orru, E., Murgia, M., Feretti, L., Govoni, F., Brunetti, G., Giovannini, G., Girardi, M. & Setti, G. 2007, A&A, 467, 943

Pacholczyk, A. G. 1970, Radio astrophysics (Freeman: San Francisco)

Parma, P., Murgia, M., de Ruiter, H. R., Fanti, R., Mack, K.-H., Govoni, F. 2007, A&A, 470, 875.

Peres, C. B., Fabian, A. C., Edge, A. C., Allen, S. W., Johnstone, R. M., & White, D. A. 1998, MNRAS, 298, 416

Peacock, J. A., Cole, S., Norberg, P., Baugh, C. M., Bland-Hawthorn, J., Bridges, T., Cannon, R. D., Colless, M., Collins, C., Couch, W., Dalton, G., Deeley, K., De Propris, R., Driver, S. P., Efstathiou, G., Ellis, R. S., Frenk, C. S., Glazebrook, K., Jackson, C., Lahav, O., Lewis, I., Lumsden, S., Maddox, S., Percival, W. J., Peterson, B. A., Price, I., Sutherland, W., & Taylor, K. 2001, Nature, 410, 169

Petrosian, V., & Bykov, A. M. 2008, SSRv, 134, 207

Pimbblet, K. A., Smail, I., Edge, A. C., O'Hely, E., Couch, W. J., & Zabludoff, A. 2006, MNRAS, 366, 645

Pizzo, R. F., & de Bruyn, A. G. 2009, A&A, 507, 639

Pizzo, R. F., de Bruyn, A. G., Feretti, L., & Govoni, F. 2008, A&A, 481, 91

Rao A. P. 2003, Low Frequency Radio Astronomy, eds. Chengalur, J. N., Gupta, Y., & Dwarakanath, K. S.(http://www.gmrt.ncra.tifr.res.in)

Reimer, O., Pohl, M., Sreekumar, P., & Mattox, J. R. 2003, ApJ, 588, 155

Rephaeli, Y., & Gruber, D. 2002, ApJ, 579, 587

Rephaeli, Y., & Gruber, D. 2003, ApJ, 595, 137

Rephaeli, Y., Nevalainen, J., Ohashi, T., & Bykov, A. M. 2008, SSRv, 134, 71

Roettiger, K., Burns, J. O., & Pinkney, J. 1995, ApJ, 453, 634

Roettiger, K., Stone, J. M., & Mushotzky, R. F. 1998, ApJ, 493, 62

Rossetti, M., & Molendi, S. 2004, A&A, 414, 41

Rottgering, H. J. A., Wieringa, M. H., Hunstead, R. W., & Ekers, R. D. 1997, MNRAS, 290, 577

Rottgering, H., Snellen, I., Miley, G., de Jong, J. P., Hanisch, R. J. & Perley, R. 1994, ApJ, 436, 654

Ryu, D., & Kang, H. 2003, JKAS, 36, 105

Sadler, E. M., Jackson, C. A., Cannon, R. D., McIntyre, V. J., Murphy, T., Bland-Hawthorn, J., Bridges, T., Cole, S., Colless, M., Collins, C., Couch, W., Dalton,

G., De Propris, R., Driver, S. P., Efstathiou, G., Ellis, R. S., Frenk, C. S., Glazebrook, K., Lahav, O., Lewis, I., Lumsden, S., Maddox, S., Madgwick, D., Norberg, P., Peacock, J. A., Peterson, B. A., Sutherland, W., & Taylor, K. 2002, MNRAS, 329, 227.

Sarazin, C. L. 1999, astro.ph.11439

Schlickeiser, R., Sievers, A., & Thiemann, H. 1987, A&A, 182, 21

Schuecker, P., Finoguenov, A., Miniati, F., Bohringer, H. & Briel, U. G. 2004, A&A, 426, 387

Schuecker, P., Bohringer, H., Reiprich, T. H., & Feretti, L. 2001, A&A, 378, 408

Slee, O. B., Roy, A. L., & Savage, A. 1994, AuJPh, 47, 145

Slee, O. B. & Reynolds, J. E. 1984, PASAu, 5, 516

Slee, O. B., & Roy, A. L. 1998, MNRAS, 297L, 86

Slee, O. B., Roy, A. L., Murgia, M., Andernach, H., & Ehle, M. 2001, AJ, 122, 1172.

Springel, V., White, S. D. M., Jenkins, A., Frenk, C. S., Yoshida, N., Gao, L., Navarro, J., Thacker, R., Croton, D., Helly, J., Peacock, J. A., Cole, S., Thomas, P., Couchman, H., Evrard, A., Colberg, J., & Pearce, F. 2005, Nature, 435, 629

Struble, M. F., & Rood, H. J. 1999, ApJS, 125, 35

Sun, M., Murray, S. S., Markevitch, M., & Vikhlinin, A. 2002, ApJ, 565, 867

Sunyaev, R. A., Norman, M. L., & Bryan, G. L. 2003, Astron, Lett., 29, 783

Thierbach, M., Klein, U., & Wielebinski, R. 2003, A&A, 397, 53

Tribble, P. 1993, MNRAS, 263, 31

van Breugel, W., De Breuck, C., Stanford, S. A., Stern, D., Rottgering, H., Miley, G. 1999, ApJL, 518, 61.

van Weeren, R. J., Rttgering, H. J. A., Bruggen, M., & Cohen, A. 2009, A&A, 508, 75

van Weeren, R. J., Intema, H. T., Oonk, J. B. R., Rottgering, H. J. A. & Clarke, T. E. 2009, A&A, in press (arXiv0910.4967)

Vazza, F., Tormen, G., Cassano, R., Brunetti, G. & Dolag, K. 2006, MNRAS, 369, L14

Venturi, T., Bardelli, S., Dallacasa, D., Brunetti, G., Giacintucci, S., Hunstead,

R. W., & Morganti, R. 2003, A&A, 402, 913

Venturi, T., Giacintucci, S., Dallacasa, D., Cassano, R., Brunetti, G., Bardelli, S., & Setti, G. 2008, A&A, 484, 327

Willson, M. A. G. 1970, MNRAS, 151, 1

White, D. A., Jones, C., & Forman, W. 1997, MNRAS, 292, 419

Wielebinski, R., Waldthausen, H., Kronberg, P. P., & Haslam, C. G. T. 1977, Nature, 266, 239

Wu, X.-P., Fang, L.-Z., & Xu, W., 1998, A&A, 338, 813

Young, A. 2004, PhD Thesis, University of Minnesota.

Zabludoff, A. I., & Zaritsky, D. 1995, ApJ, 447, 21

Zwicky, F. 1938, PASP, 50, 218